UNIVERSITÀ POLITECNICA DELLE MARCHE
FACOLTÀ DI INGEGNERIA

Corso di Laurea magistrale in Biomedical Engineering

Quantitative Biomarkers of Contrast-Free High-Definition Ultrasound Microvessel Imaging for Differentiation of Thyroid Nodule

Relatore:
Lorenzo Scalise

Tesi di Laurea di:
Melisa Kurti

Correlatori:
Mostafa Fatemi, PhD
Azra Alizad, MD

A.A. 2021/2022

ai miei genitori, a mio fratello per esserci Sempre.
(to my parents, to my brother for being there Always.)

ABSTRACT

There are significant differences in microvascular morphological features in diseased tissues, such as cancerous lesions, compared to noncancerous tissue. Quantification of microvessel morphological features play an important role in disease diagnosis and tumor classification.

In this study, has been used multiple image enhancement techniques and appropriate morphological feature extraction methods that enable quantitative analysis of microvasculature structures, named high-definition microvasculature imaging (HDMI).

Morphological features of tumor microvessels such as vessel segment diameter and length, number of branch points, vessel density, tortuosity, microvessel fractal dimension (mvFD), Murray's deviation (MD), bifurcation angle (BA), and spatial vascularity pattern (SVP) were extracted and analyzed, and the results correlated with pathology.

These methods have been tested on in vivo images of 92 thyroid nodule microvasculature. Initial results show that using vessel morphological features allows for differentiation between malignant and benign thyroid nodules. All malignant thyroid nodules had higher values of *(NV)*, *(NB)*, *(VD)*, *(mvFD)*, *(BA_{mean})* and *(MD)* when compared to benign nodules, demonstrating a p-value of (**4.9E-05, 9.8E-06, 6.1E-04, 5.5E-05, 2.9E-03**, **5.5E-03**) respectively. The multivariable analysis using a support vector machine (SVM) classification method trained in the space of HDMI only and HDMI biomarkers combined with clinical factors (age, size and TI-RADS) has been used to develop two different models, HDMI model and HDMI-C. From the first model the AUC was 0.83 (95% CI: 0.75-0.91), with a sensitivity of 78% and a specificity of 80%. The AUC was further improved when clinical factors, including age, dimension, and TI-RADS was added to the HDMI model. The corresponding AUC estimate was 0.88 (95% CI: 0.81-0.94), with a sensitivity of 88 % and a specificity of 73%.

In conclusion this analysis suggests that TI-RADS combined with HDMI biomarkers may have a good performance in distinguishing benign and malignant thyroid nodules, but to increase the diagnostic accuracy further detailed studies are required to confirm the present findings.

INDEX

INTRODUCTION

The incidence of thyroid cancer, the most prevalent endocrine cancer worldwide, has increased in last few decade (1) and (2). Furthermore, thyroid nodules are commonly found in routine physical examination or as incidental findings on diagnostic imaging performed for other nonthyroidal indications (3). Clinical examination via palpation is subjective for detection of thyroid nodules and depends on the experience of the examining clinician, as well as the size and location of nodule (4). Although ultrasonography is the first line imaging tool in evaluating thyroid nodules, the high sensitivity for detecting nodules but unsatisfactory specificity for cancer results in overwhelming benign fine needle aspiration (FNA), about 60%–80% (5). While FNA is a widely used and safe procedure, complications such as discomfort or local pain and self-limited small hematomas may occur (6). The low specificity of ultrasound features for classifying thyroid nodules leads to unnecessary FNAs, therefore, new imaging modalities with special attention to anarchical angiogenesis observed in malignancy are of paramount importance in characterization of nodules. Addition of strain elastography (7) (8) (9)and shear wave elastography (10) (11) (12)relatively increased the sensitivity and specificity of ultrasound.

Thyroid nodules exhibit different patterns of blood flow and vascular morphology that are useful in separating malignant nodules from benign(13). Furthermore, angiogenic activity and sprouting angiogenesis is crucial to thyroid cancer progression (14). Because of neovascularization, the hallmark of cancer the microvessel structures in malignant nodules look quite different from that of in benign (15). Imaging modalities that could image and quantify the morphology of tumor microvessel can facilitate cancer diagnosis. Patterns of vascularity, intra-nodular with absent or insignificant perinodular blood flow shown in Color Doppler ultrasound (CDUS) and Power Doppler ultrasound (PDUS) suggest malignancy (16)and (17). With recent advances in slow blood flow imaging, attempts have begun to non-invasively image tumor's microvessel structures. With the help of contrast agents, acoustic angiography, enables high-resolution imaging of microvasculature(18).Recently, Superb microvascular imaging (SMI) has reported the added value of its microvessel imaging with (19)and without (20) TI-RADDS for distinguishing benign and malignant thyroid nodules, however, this method is based on visual inspection and quantification is limited to pixel counting.

A newly developed contrast-free ultrasound-based modality has been introduced to visualize microvessels at a sub-millimeter level, about 300 μm in diameter(21), labeling it as high-definition

microvessel imaging (HDMI)(22). A series of morphological filtering and vessel enhancement has complemented HDMI approach to quantify tumor vessel morphological parameters as quantitative vessel biomarkers (23) (21) and (22). Quantitative HDMI has been tested for distinguishing malignant breast masses from benign remarkable results (24), and(25).
The objective of the present study is to evaluate the performance of our proposed quantitative microvessel imaging in classifying malignant and benign thyroid nodules. In this study, microvessel vessel morphological features of thyroid nodules (vessel diameter, tortuosity, vascular density, branch points, number of segments, bifurcation angle, and Murray deviation) have been used as HDMI biomarkers. Additionally, all the vessel biomarkers alone and HDMI features with clinical information (age, nodules dimension, and TI-RADS) used to create a model capable of classifying the thyroid nodules as benign or malignant.

1. Thyroid Gland Structure and Function

The thyroid gland is a part of human endocrine system. Thyroid gland works together with the nervous system and the immune system to regulate the body metabolism by secreting hormones and releasing it into the blood stream. This section is referred to Thyroid Gland from Physiopedia website (26) and (27).

1.1 Thyroid anatomy

Thyroid gland is a butterfly shaped organ and is situated at the front of the neck in the lower part of the throat and consists of two connected lobes on either side of the trachea . The lower end of the lobes is connected by thyroid isthmus which is a thin band of connective tissue.
Each of the thyroid lobes are embedded with parathyroid glands, primarily on their posterior surfaces. The tissue of the thyroid gland is composed mostly of thyroid follicles. The follicles are made up of a central cavity filled with a sticky fluid called colloid. Surrounded by a wall of epithelial follicle cells, the colloid is the center of thyroid hormone production, and that production is dependent on the hormones' essential and unique component: iodine.
In Figure 1.1 are representet respectively, (a) Anterior view of the thyroid gland. (b) Posterior view of the thyroid gland. (c) The glandular tissue is composed primarily of thyroid follicles.

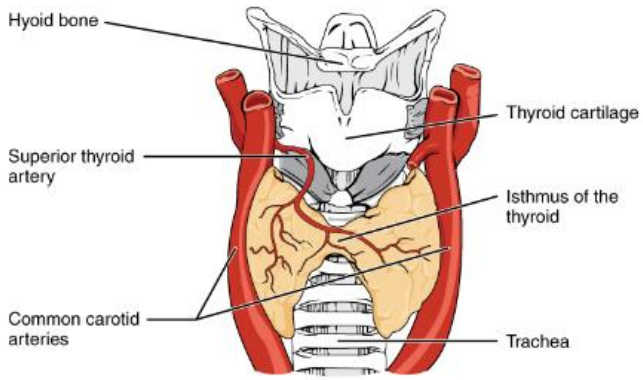

a) Anterior view

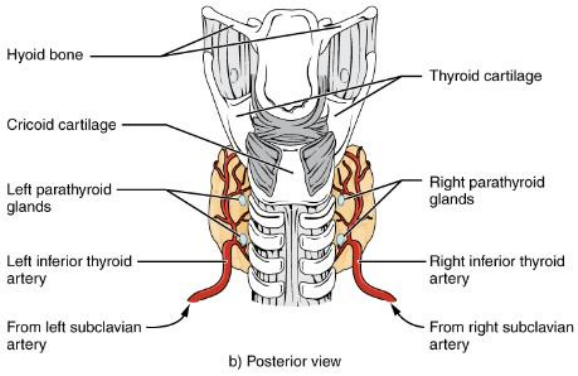

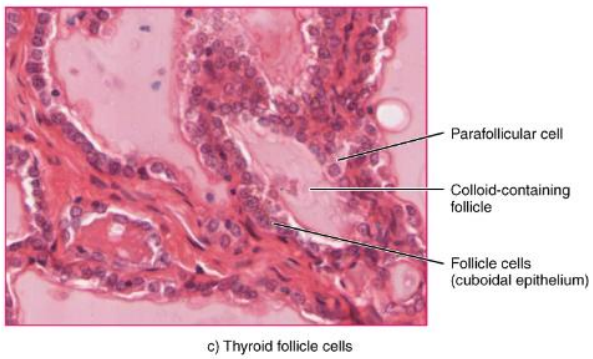

Figure 1.1: a) anterior view of the thyroid gland, b) posterior view of the thyroid, c) thyroid fullicle cell

1.2 Thyroid physiology

The thyroid hormone controls metabolism, growth, and many other bodily functions. The thyroid gland, anterior pituitary gland, and hypothalamus comprise a self-regulatory circuit called the hypothalamic-pituitary-thyroid axis. The main hormones produced by the thyroid gland are thyroxine or tetraiodothyronine (T4) and triiodothyronine (T3). Thyrotropin-releasing hormone (TRH) from the hypothalamus, thyroid-stimulating hormone (TSH) from the anterior pituitary gland, and T4 work in synchronous harmony to maintain proper feedback mechanism and homeostasis. Iodine is an essential trace element absorbed in the small intestine. It is an integral part of T3 and T4. Decreased iodine intake can cause iodine deficiency and decreased thyroid hormone synthesis. Iodine deficiency can cause cretinism, goiter, myxedema coma, and hypothyroidism.

The primary secretory product is inactive thyroxine, or T4, a prohormone of triiodothyronine, or T3. T4 is converted to T3 peripherally by type 1 deiodinase in tissues with high blood flow, such as the liver and kidneys. In the brain, T4 is converted to active T3 by type 2 deiodinase produced by glial cells. The third iodothyronine is called reverse T3, or rT3. rT3 is inactive and forms by type 3 deiodinase activity on T4.

These iodothyronines are composed of thyroglobulin and iodine. Thyroglobulin is formed from amino acids in a basal to apical fashion within the thyroid cells themselves. Thyroglobulin is then secreted into the follicular lumen, where it is enzymatically combined with iodine to form iodinated thyroglobulin. Endosomes containing this iodinated thyroglobulin then fuse with lysosomes, which enzymatically release the thyroglobulin from the resultant thyroid hormone. The thyroid hormones are next released from the cell while the remaining thyroglobulin is deiodinated and recycled for further use.

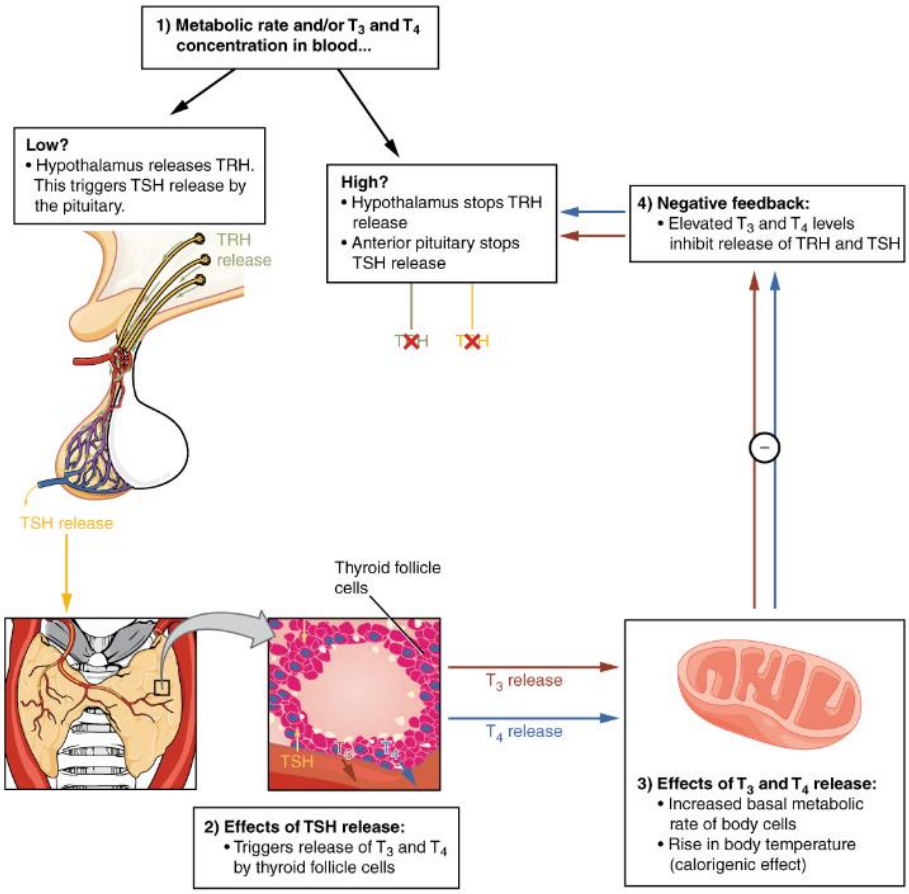

Figure 1.2: Negative feedback loop controls the regulation of thyroid hormone levels.

Functions of thyroid hormons

The thyroid hormones, T_3 and T_4, are often referred to as metabolic hormones because their levels influence the body's basal metabolic rate, the amount of energy used by the body at rest. When T_3 and T_4 bind to intracellular receptors located on the mitochondria, they cause an increase in nutrient breakdown and the use of oxygen to produce ATP. In addition, T_3 and T_4 initiate the transcription of genes involved in glucose oxidation. Although these mechanisms prompt cells to produce more ATP, the process is inefficient, and an abnormally increased level of heat is released as a byproduct of these reactions. This so-called calorigenic effect (calor- = "heat") raises body temperature.

Adequate levels of thyroid hormones are also required for protein synthesis and for fetal and childhood tissue development and growth. They are especially critical for normal development of the nervous system both in utero and in early childhood, and they continue to support neurological function in adults. Finally, thyroid hormones increase the body's sensitivity to catecholamines (epinephrine and norepinephrine) from the adrenal medulla by upregulation of receptors in the blood vessels. When levels of T_3 and T_4 hormones are excessive, this effect accelerates the heart rate, strengthens the heartbeat, and increases blood pressure. Because thyroid hormones regulate metabolism, heat production, protein synthesis, and many other body functions, thyroid disorders can have severe and widespread consequences.

1.3 Thyroid Pathophysiology

Hypothyroidism is an endocrine disorder with resultant under-production of thyroid hormone. This disorder of the thyroid gland results in excess T3 and T4 production along with the compensatory decrease of TSH. Common symptoms of hypothyroidism include cold intolerance and weight gain due to decreased basal metabolic rate and thermogenesis, depression, fatigue, decreased peripheral reflexes, and constipation, due to decreased stimulation of the central and peripheral nervous system. Many other consequences of hypothyroidism can manifest secondary to the lack of activated thyroid hormone on various tissues and organs of the body.

Hyperthyroidism is an endocrine disorder with excess thyroid hormone production. In primary hypothyroidism, decreased production of thyroid hormones by the thyroid gland causes a compensatory increase of TSH. Secondary hypothyroidism is caused by pituitary disorders causing decreased TSH release and decreased T3/T4 levels. Tertiary hypothyroidism is caused by hypothalamic disorders, resulting in decreased TRH levels, decreased TSH, and T3/T4 levels. In contrast to hypothyroidism, hyperthyroidism often causes heat intolerance, weight loss, anxiety, hyperreflexia, and palpitations. Increased stimulation of basal metabolic rate, thermogenesis, resting heart rate, and cardiac output, and central and peripheral nervous systems result in the most common symptoms.

Two of the most common causes of hyperthyroidism and hypothyroidism are:

I. Graves' Disease: Graves' disease is the most common cause of hyperthyroidism. It is an autoimmune disease caused by the production of TSH receptor antibodies that stimulate thyroid gland growth and thyroid hormone release. Patients will have abnormally increased T4 and T3 levels and a decrease in TSH. A positive TSH-receptor IgG immunoglobulin test confirms the diagnosis. Patients will often present with symptoms of hyperthyroidism and diffuse goiter. TSH-receptor antibodies can also activate orbital fibroblasts leading to fibroblast proliferation and differentiation to adipocytes. As a result, there is increased production of hyaluronic acid and glycosaminoglycan (GAG), leading to an increased volume of intraorbital fat and muscle tissue. It causes exophthalmos, lid retraction, and diplopia due to ocular motility problems. Pretibial myxedema is another finding in Graves' disease. It is due to the stimulation of dermal fibroblasts that leads to depositions of GAGs in the connective tissue. 70% of patients with Graves' disease has elevated anti-TPO antibodies.

II. Hashimoto Thyroiditis: The most common cause of hypothyroidism in iodine-sufficient areas is Hashimoto Thyroiditis. It is caused by autoimmune-mediated destruction of the thyroid gland. CD8+ T-cells cause thyroid follicular cell death. The release of IFN-gamma by TH1 cells causes recruitment and activation of macrophages. During the early stage of the disease, the patient develops a non-tender, symmetrical, and painless goiter. As inflammation continues, thyroid follicles are damaged and can rupture. When thyroid follicles rupture, the patient may be asymptomatic or can experience Hashitoxicosis (thyroid hormone from ruptured follicles, causing symptoms of hyperthyroidism). As the disease progresses, the thyroid gland may become normal-size or small, depending on the extent of fibrosis. As a result, the patient can develop the symptoms of hypothyroidism.

Other thyroid gland conditions

Goitre: It is defined as significantly enlarged and swollen thyroid gland. It is commonly seen in patients with iodine deficiency. As the pituitary gland tries to over-compensate by over stimulating the thyroid gland to produce more hormone, the thyroid gland grow larger and larger as it tries to produce more thyroid hormones. Goitre can also be associated with Hashimoto's thyroiditis, a condition related to thyroid gland inflammation.

Thyroid nodules: It is a small abnormal mass or lump in the thyroid gland. Thyroid nodules are extremely common, a few of which are known to be cancerous. They are known to secrete excess hormones, causing hyperthyroidism, or cause no problems at all. There are four major subtypes of thyroid cancer: papillary (PTC), follicular (FTC), anaplastic (ATC), and medullary thyroid cancer (MTC). Less common subtypes include: Hurthle cell carcinoma (HTC) and poorly differentiated thyroid cancer (PDTC).

Congenital thyroid disease: It is an extremely rare condition where; some babies are born with a defective thyroid gland or no thyroid gland at all. In most cases, the thyroid gland won't develop normally for unknown reasons, it may be an inherited disorder. Often, infants with congenital hypothyroidism appear normal at birth. That's one reason why most states now require newborn thyroid screening.

Iodine deficiency disorder: The trace mineral iodine is essential for the production of thyroid hormones. Too little iodine can cause hypothyroidism, and too much iodine can worsen hypothyroidism in people who are already suffering from the condition.

Thyroid storm: It is a rare form of hyperthyroidism in which extremely high thyroid hormone levels cause severe illness.

Pituitary disorder: It is a very rare form of hypothyroidism in which failure of the pituitary gland to produce enough thyroid-stimulating hormone (TSH) causes hypothyroidism. Mostly it happens because of pituitary gland tumor (which is mostly benign).

Pregnancy and postpartum: women develop hypothyroidism as their body produces antibodies to their own thyroid gland. If left untreated it can cause miscarriage, premature delivery, and preeclampsia. It can also cause defects in the developing fetus.

2.Thyroid cancer Diagnosis: Imaging modalities

This session refers to Kimberley-Jane Bonjoc: Thyroid cancer diagnosis in the era of precision imaging (28)

2.1 Ultrasound

Ultrasound is the initial modality of choice to evaluate thyroid nodules and distinguish benign from nodules. Ultrasound is cost-effective, readily available, and does not expose patients to radiation. Ultrasound is not only useful in detecting primary neoplasm, but it can evaluate locoregional lymph nodes for nodal metastasis. In diagnostic ultrasounds, thyroid nodules are characterized based on: size, margins, eccentric location of solid portion, hypoechogenicity, microcalcification, irregular shape, and if the tumor is taller than it is wide. Features extracted from this criterion help distinguish benign from malignant thyroid nodules. For example, irregular margins and microcalcifications are associated with malignant nodules while small subcentimeter spongiform avascular nodules are considered benign.

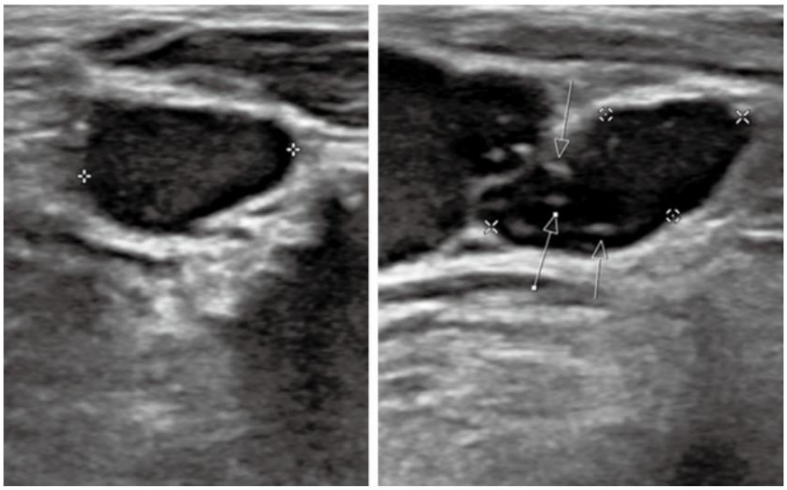

Figure 2.1: A 82-year-old female diagnosed with metastatic and classical tyroid carcinoma. Transverse (left) and longitudinal (right) ultrasound displays thyroid lesion with microcalsification indicated by the white arrows.

The American College of Radiologists (ACR) uses a thyroid cancer diagnostic management system called the Thyroid Imaging Reporting and Data System (TI-RADS). TI-RADS is increasingly used by radiologists and other healthcare practitioners to plan management of thyroid tumors, which may include FNA cytology, surgery, and administration of radiotherapy. TI-RADS criteria is based on composition, echogenicity, shape/morphology margins. Each criterion is scored based on risk levels range from benign to highly suspicious designated by TR1 and TR5, respectively. The criteria, scoring system, classification and recommendations based on classifications that are shown in. These risk levels help to determine management of thyroid tumors.

Table 2.1: Presents the five categories (TR1-TR5), the scoring for each category, the classification, and recommendations for each category defined by the Thyroid Imaging, Reporting, and Data Sysem (TIRADS) developed by the American College of Radiologists (ACR).

Category	**TR1**	**TR2**	**TR3**	**TR4**	**TR5**
Scoring	0	2	3	4–6	≥7
Classification	Benign	Not suspicious	Mildly suspicious	Moderately suspicious	Highly suspicious
Recommendations	No FNA required	No FNA required	≥1.5 cm follow up, ≥2.5 cm FNA; follow up: 1, 3, 5 years	≥1.0 cm follow up, ≥1.5 cm FNA; follow up: 1, 3, 5 years	≥0.5 cm follow up, ≥1.0 cm FNA; annual follow up for up to 5 years

2.2 Single Photon Emission Computed Tomography

123Iodine SPECT scans is an important diagnostic tool used in clinical practice for work-up of indeterminate or suspicious thyroid nodules as well as staging of thyroid cancer. Sodium-iodide symporters (NIS) located on the basolateral plasma membrane of thyrocytes leads to increased affinity for iodine and this physiologic mechanism is leveraged in radioiodine imaging and therapy. Whole-body scintigraphy (WBS) is commonly performed with 123Iodine to evaluate whether a suspicious or indeterminate thyroid nodule is "hot" (increased iodine uptake) or "cold" (diminished thyroid uptake). Radioiodine scans are particularly useful in differentiated subtypes of thyroid cancer due to preserved NIS allowing for preferential increased accumulation of radioactive iodine in the neoplasm compared to normal thyroid tissue figure 2.2. As thyroid neoplasms de-differentiate, they lose the NIS rendering abilities these lesions occult on radioiodine SPECT; an important false-negative to be aware of. In patients post thyroidectomy and/or lymph node dissection, radioiodine scan can help identify residual thyroid tissue and/or identify additional sites of metastasis. ^{131}Iodine (^{131}I) emits both beta and gamma particles, making it the perfect theranostics agent. ^{131}I is commonly administered post-thyroidectomy with or without nodal dissection for treatment of residual thyroid tissue and for treatment of local/distal metastasis. Additionally, due to 131I gamma activity, SPECT can be performed to evaluate response to 131Iodine radioablation. Post-ablation SPECT is usually performed within five-to-nine days due to improved signal-to-noise ration that increases overall sensitivity for detection of distant metastases.

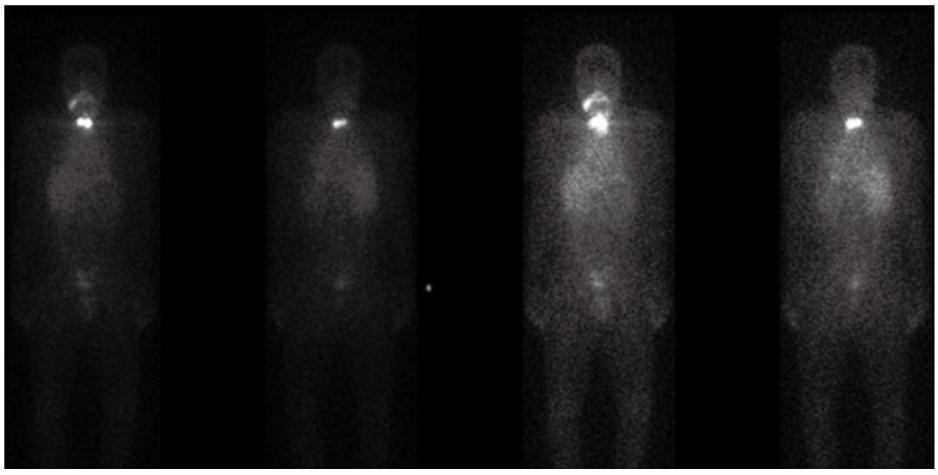

Figure 2.2: A 39-year-old male patient diagnosed with metastatic papillary thyroid carcinoma. Patient presents 131-Iodine uptake in I-SPECT scan.

2.3 Computed Tomography

With continual increase in use of CT, unsuspected thyroid nodules are often detected on CT. Incidental thyroid nodule detection rate on CT chest ranges from 2–65% . Although majority of these incidental thyroid nodules are benign, 5% of these nodules are malignant. Due to continued increase in utilization of CT with increased detection of thyroid nodules, coupled with a decade long trend of increased incidence of thyroid neoplasm, the ACR put forth recommendations for management of incidental thyroid nodules as referred in Figure 2.3. Thyroid nodules with suspicious features on CT are followed-up with ultrasound and may require ultrasound-guided FNA biopsies to determine whether the thyroid lesion is benign or malignant. Although CT is not the initial modality of choice for evaluation of primary thyroid cancer, it is useful for staging thyroid cancer in detection of metastasis. In cases where primary thyroid lesion has substernal extension or there is concern for airway compromise, CT is the preferred diagnostic modality Figure 2.4.

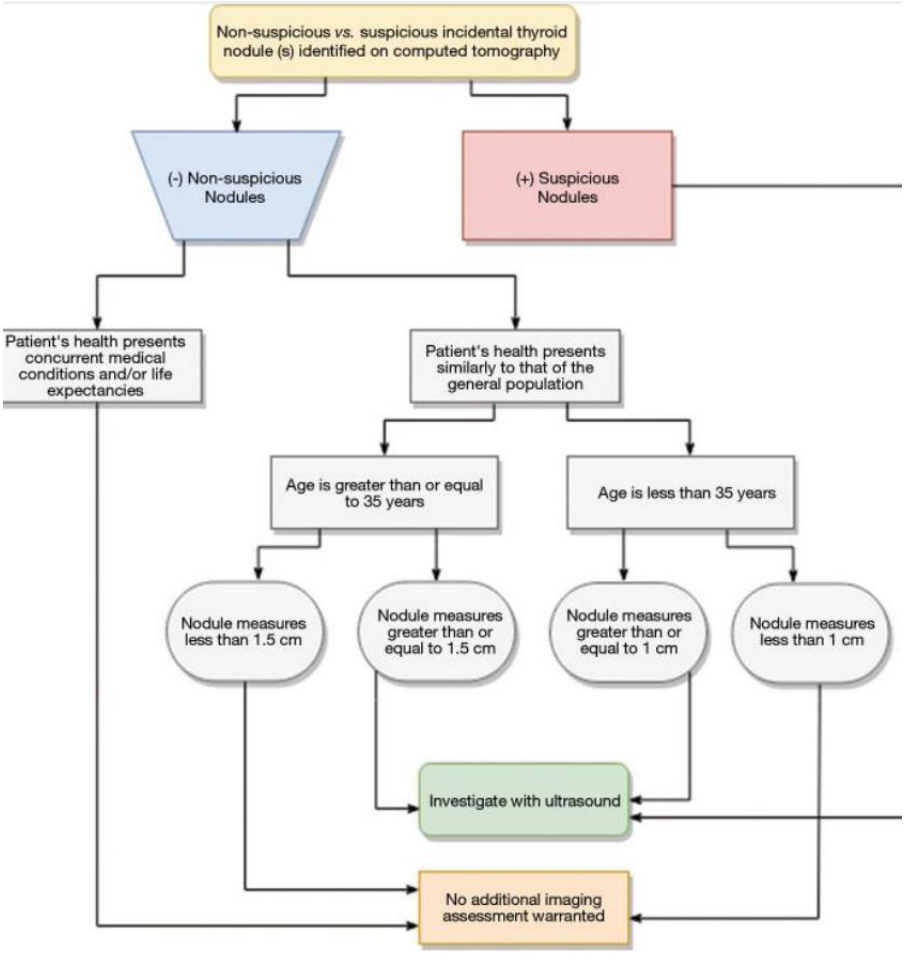

Figure 2.3: Clinical work-up for incidental thyroids identified on computed tomography

Figure 2.4: Coronal (left) and sagittal (right) CT of a 39-year-old male patient diagnosed with metastatic papillary thyroid carcinoma. Patient presents a heterogeneously enhancing thyroid nodule that is eroding through the thyroid capsule (white arrows).

2.4 Magnetic Resonance Imaging

Due to cost and limited availability compared to other modalities, MRI is used most frequently in a second line setting for characterization of tumor in suspicious regions. Ultrasound is the modality of choice for initial diagnosis and follow-up assessment in thyroid cancer. In cases where recurrence/relapse is suspected, MRI is utilized due to its superior soft tissue resolution relative to ultrasound, CT, PET/CT, and SPECT, Figure 2.5. In high-risk patients (e.g., incidence of familiar neoplasm, aggressive initial cancer with positive margins, etc.), MRI is the modality of choice to survey for recurrence. Improved contrast and soft tissue resolution on newer MRI techniques provides more precise evaluation of tumor extent and infiltration of surrounding tissues (vessels, nerves, bones, etc.). MRI techniques such as diffusion weighted imaging (DWI), coupled with changes in other sequences (T1- and T2-weighted) can help discriminate between benign and malignant thyroid lesions. Perfusion MRI, which evaluates degree to tumor vascularity and tumoral blood flow relative to the normal tissue, has also shown to be a helpful technique in discriminating benign and malignant lesions. One key challenge, which is an active area of research in MRI , is overcoming image quality

degradation from susceptibility artifact that generates from metals and air. These artifacts are commonly present in the surgical site, limiting evaluation of local disease. Newer surgical techniques and newer MRI sequences are being developed to overcome these limitations.

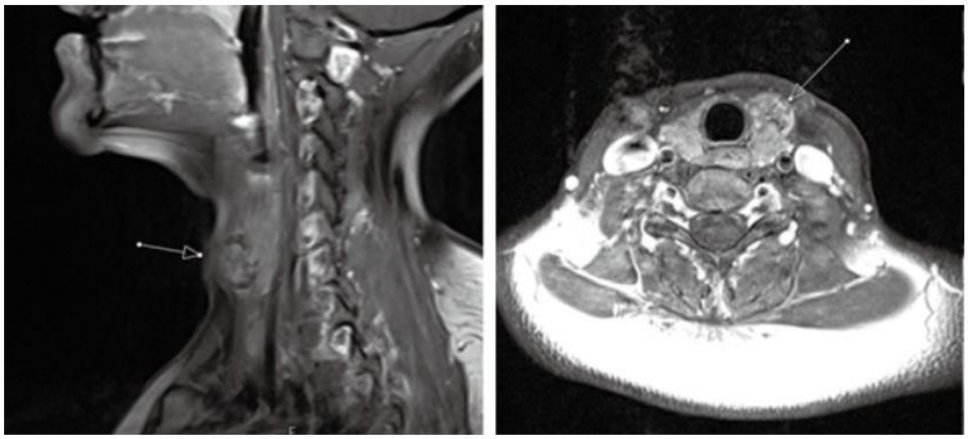

Figure 2.5: Sagittal (left) and axial (right) T1-post contrast MRI of a 37-year-old female diagnosed with papillary thyroid carcinoma. T1-post-contrast MRI demonstrates heterogeneously enhancing nodule in the anterior aspect of left thyroid lobe (arrows) with well-circumscribed borders without evidence of ipsilateral adenopthy or tracheal invasion.

3. Ultrasound Imaging

The sections of this chapter refer to “Diagnostic Ultrasound Imaging” of Thomas L. SZABO (29) , Bjrum et al.(30) and Bercoff J.et al (31) .

Ultrasound (US) imaging is one of the most widely used medical imaging modalities, thanks to being non-ionizing and having a greater cost-effectiveness and portability compared with X-ray, computed tomography (CT) or magnetic resonance imaging (MRI). While US imaging might be limited in its ability to image deep tissue compared with X-ray, CT or MRI, it can produce high-resolution images of soft tissue in real time. Recently, US imaging has been revolutionized by the development of ultrafast US imaging, an acquisition technique enabling frame rates of multiple kilohertz. To date, most commercial US scanners rely on an acquisition process called line-by-line scanning to reconstruct full-view images. This process consists of performing sequential pulse-echo acquisitions using focused transmit beams, suitably steered for the different image scan lines. To obtain high-quality images, several tens or few hundreds of scan lines are conventionally used in 2-D imaging, enabling frames rate of about 10 Hz to 30 Hz that are compatible for real-time visualization. Later Doppler imaging has been introduced. Doppler-based techniques are established tools in ultrasound imaging systems for flow analysis and quantification and have become indispensable in the context cancer assessment.

The use of Doppler imaging enables visualizing and quantifying blood flow by analyzing interactions of acoustic pulses with flowing blood within the vessel lumen.

Flow quantification is then typically available only at a single location (sample volume) or multiple locations along the same line (multigating). Color flow imaging overcomes the limited spatial sampling of the spectral analysis by partly sacrificing the quantitative analysis, by reducing the observation time at any given location and spreading the ultrasound firings over a 2-D region of interest. The big challenge of Doppler modes arises from the fact that was required simultaneous real time display of B-mode (gray scale) and PW-mode (duplex mode), or even B-, color- and PW-modes (triplex mode). Duplex and triplex simultaneous modes have become standard on ultrasound systems but suffer from frame rate limitations in deep organs such as the liver or heart. Duplex and triplex modes represent major technical challenges because they require complex sequencing, high-energy ultrasound transmission, and high processing power. Consequently, there is the need to reduce the number of ultrasound firings required to perform Doppler analysis while keeping constant or increasing performance. The simplest solution consists of reducing the number of transmit beams per

color flow image by widening them. Plane-wave transmission represents the most efficient solution in terms of number of firings.

UltraFast imaging represents an opportunity to overcome the presented limitations and create a new paradigm in ultrasound-based flow analysis by merging color Doppler and PW Doppler in one feature: UltraFast Doppler.

Ultrafast US imaging relies on the insonification of the entire field of view at once by transmitting an unfocused wavefront, such as a plane wave (PW) or a diverging wave (DW), thus breaking with the trade-off between field of view and frame rate inherent to conventional transmit-focused line-by-line scanning. This strategy, enables imaging large tissue regions at very high frame rates of multiple kilohertz. The main disadvantage of ultrafast US imaging compared with conventional line by line scanning is a decrease in image quality. Indeed, compared with a focused transmit beam which concentrates most of its energy in a limited region of interest, the energy of an unfocused wavefront is spread over the entire field of view, resulting in backscattered echoes of lower amplitude and measurements with lower signal-to-noise ratio (SNR). The absence of transmit focusing also results in a broader main lobe of the point spread function (PSF), consequently degrading the lateral image resolution. Furthermore, diffraction artifacts, such as the ones caused by grating lobes (GLs), side lobes (SLs), and edge waves (EWs), are more pronounced in ultrafast US imaging, consequently degrading the image contrast. The strategy to increase the image quality in ultrafast US imaging consists of coherently compounding low-quality images obtained from multiple, differently steered, unfocused transmit wavefronts. This method successfully improves the image quality by increasing the number of steered acquisitions, potentially even surpassing the quality of conventional focused imaging.

3.1 Conventional Ultrasound Imaging

Ultrasound imaging is usually performed by sequential insonification of the medium using focused beams. Each beam allows the reconstruction of one image line. A 2D image is usually made of a few tens of lines.

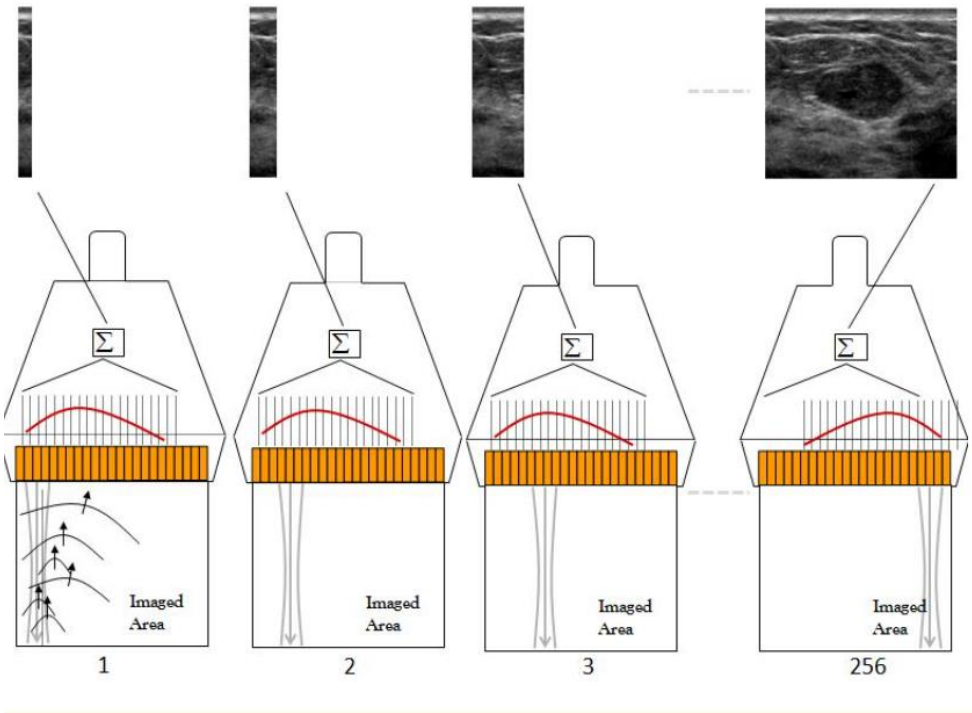

Figure 3.1: Conventional imaging acquisition process

The frame rate of the imaging mode is set by the time required to transmit a beam, receive and process the backscattered echoes from the medium and repeat that for all the lines of the image.
For a conventional 2D image, the time to build an image is:

$$Timage = \mathbf{2} * \boldsymbol{Z} * \boldsymbol{Nlinesc} \quad (3.1)$$

where Z is the image depth, c the speed of ultrasound waves assumed constant (1540 m/s) and $Nlines$ the number of lines in the image. The maximum frame rate that can be reached with this technique is:

$$FRmax = \mathbf{1}\boldsymbol{Timage} \quad (3.2)$$

Limitations of the conventional approach appear as soon as higher frame rates are required. Most current systems have multiline capabilities: for each transmit beam, several lines (2 to 16) are computed. Multiline processing can be used either to increase the frame rate o increase the number of lines computed per image.

4.1.1 Basic Principle of ultrasonic imaging

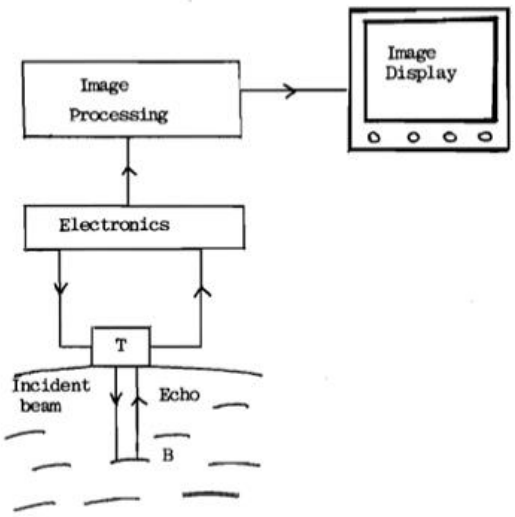

Figure 3.2: Basic of ultrasonic imaging

An ultrasonic transducer (T) sends a beam of ultrasound into the subject over a selected area of interest. At an acoustic boundary such as B within tissue, some of the ultrasound energy is reflected, either specularly or by scattering. Some of the reflected ultrasound will go back towards T. At the transducer, the returning echoes interacts with the piezoelectric crystal and generate an electric signal. This signal will be electronically processed and measured. The location of its origin at B will be determined. Ultrasonic imaging involves the mapping of the pattern of echoes reflected from acoustic boundaries within tissues. Characteristic echo patterns are obtained for different tissues. The basic diagnostic parameters to be determined in ultrasonic imaging are:

I. The size of an echo
II. The distance of echo origin from the transducer.

The ultrasound beam is built by scanning with the beam on the subject. For each position of the ultrasound beam, a set of signals will be recorded along the beam path, corresponding to reflecting boundaries lying at different distances from the transducer. The set of signals produced along one beam path may be referred to as a "scan line". It represents single-dimensional information along the beam path. By sweeping the ultrasound beam across the subject ("scanning") in a selected direction, many other scan lines are generated to build a two-dimensional (2-D) image of a plane in the subject. This plane will be defined by the chosen direction of beam sweep.

3.1.2 Electronic processing of the signal

The signals generated by the returning echoes at the transducer are electronically processed and organized in computer memory before being displayed on a cathode ray oscilloscope. First, the signals are amplified to increase their sizes. The intensity of an echo may be a tiny fraction of the original output intensity of the transducer, hence the piezoelectric voltage it generates at the transducer may be very small. Secondly, echoes returning from different tissue depths must be subjected to compensation for attenuation differences.
Time gain compensation (TGC) is a process of applying differential amplification to signals received from different tissue depths, with echoes originating from longer distances being amplified to a greater extent than those from shorter distances in such a way that similar tissue boundaries give equal sized signals regardless of their depth in tissue. Because the dynamic range of signal sizes may be very wide, the range of signal sizes is compressed by using logarithmic. Finally, signal sizes which are extremely small can be electronically rejected. Very small signal sizes have an increased

probability of being associated with artefacts. Rejection eliminates all signals whose magnitudes are below a certain threshold level. The accepted signals are organized in computer memory before being presented to a cathode ray oscilloscope (CRO) for display. Each echo signal is associated with its own intensity level and anatomical position in tissue. Intensity and geometrical coordinates must therefore be assigned to each accepted signal. This information is then read out of memory and displayed as an image on a CRO. Hard copies of the image may then be captured using a suitable recording medium, such as thermal printing paper.

3.2 Doppler Ultrasound

The Doppler effect is the phenomenon that causes a stationary observer to hear a change in the pitch of a police siren or racing car as it speeds past them. The effect is used in medical ultrasound to detect and evaluate blood flow. When a pulse of sound is reflected from a target that is moving either towards or away from the transducer, the reflected echo will have a different frequency to that of the transmitted pulse. If the reflecting target is moving towards the transducer, the echo frequency will be higher than the transmit frequency; if the target is moving away the echo frequency will be lower.

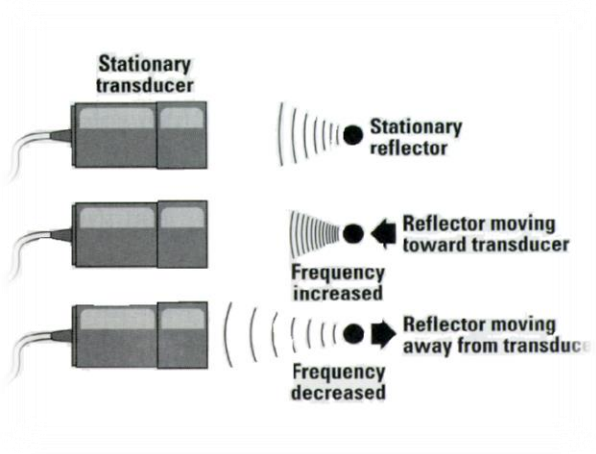

Figure 3.3: Doppler effect

The Doppler signal can be displayed as either a colour-coded overlay on the B-mode image – *colour flow mapping*, or as a graphical representation of the velocity profile over time at a specific operator selected anatomical location – *spectral Doppler.*

3.2.1 Doppler Equation

Doppler equipment is usually used to detect and evaluate blood flow in arteries and veins. A typical set-up is displayed in Figure 3.4. The ultrasonic transducer is placed in contact with the skin surface and the ultrasound beam is directed toward the vessel. The beam is at an angle θ with respect to the axis of the vessel. Red blood cells flowing in the vessel scatter ultrasound waves, giving rise to echo signals.

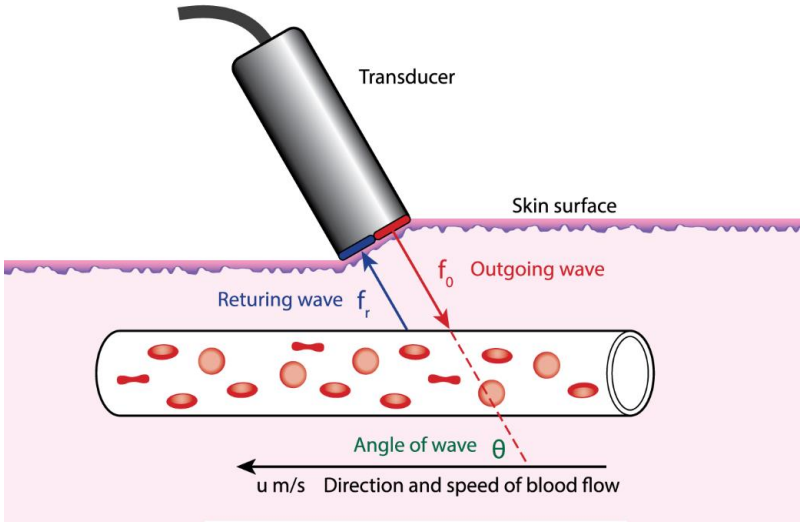

Figure 3.4: Set-up for detecting Doppler signals within the vessel.

Because the scatters are moving, the frequency of the return echo signals is Doppler shifted. The Doppler frequency, *fD*, and is given by:

$$fd = f_t - fr = \frac{2ftv_{cos\,\theta}}{C} \tag{3.3}$$

where *ft* and *fr* are the transmitted and received ultrasound frequencies, respectively, *v* the reflector velocity, *c* the speed of sound, and θ the angle between the ultrasound beam and the reflector path. The velocity *c* and the transmitted frequency *ft* are *a priori* known and therefore the reflector velocity can be estimated as follow:

$$v = \frac{kfd}{\cos\theta} \tag{3.4}$$

where k is a known constant given by:

$$k = \frac{c}{2f_t} \tag{3.5}$$

If the velocity is at a normal angle (90-degree) to the beam, the radial component of the velocity is zero and no Doppler shift is observed. Moreover, 0-degree Doppler angle corresponds to reflectors moving directly towards the transducer and, a 180-degree Doppler angle corresponds to reflectors moving directly away from the transducer.

There are two different kinds of Doppler modes available: spectral analysis (continuous or pulsed) and color-coded flow velocity and/or power imaging.

3.2.2 Continuous-Wave Velocity

An ultrasound beam is continuously transmitted into the tissue with one transducer while the back scattered signal is continuously received by another transducer Figure 3.5.

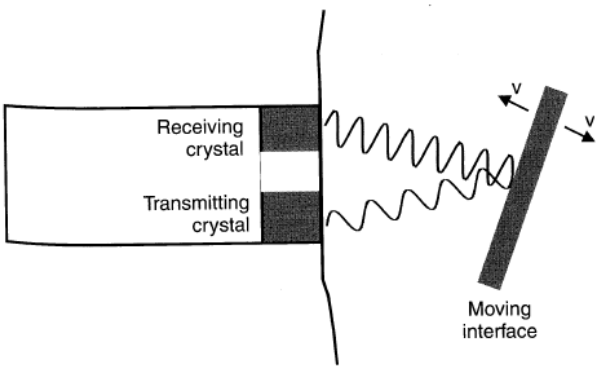

Figure 3.5: CW principle of work

Thus, all the moving targets within the overlap of the beams - sample volume - of the dual-transducer assembly are detected. This gives practically no range resolution, but since there is the continuous recording of the return signal, there is also no sampling and frequency aliasing, and no limit on the maximum velocity that can be measured.

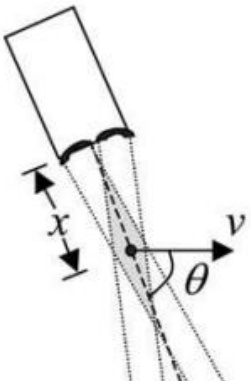

Figure 3.6: CW instrument detects Doppler shifted echoes in the region of overlap between the beams of the transmitting and receiving elements.

3.2.3 Pulsed-Wave Velocity

A drawback of the continuous-wave approach is the lack of range, or depth, information since transmit and receive elements are in proximity. An inherent limitation of the technique is that there is no uniqueness between a Doppler spectrum and a flow profile, rendering the method questionable for the reliable differentiation between normal and pathological cases. To overcome these limitations, pulsed wave systems were developed that allow for the investigation of flow patterns in individual vessels or individual parts of a vessel, Figure 3.7.

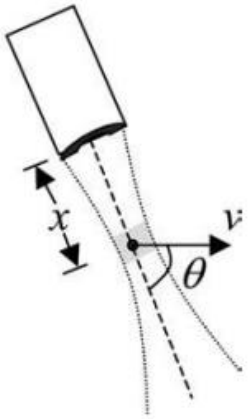

Figure 3.7: Pulsed wave Doppler uses the whole aperture for both send and transmit.

The pulsed-wave systems combine characteristics from pulse echo imaging and CW Doppler methods. A pressure wave of a certain frequency is emitted, like the CW system, but at short pulses and certain PRF. RF echoes are then received by the same transducer following each pulse and then gated with an adjustable duration.

3.3 Color flow imaging

Standard ultrasonic pulse-echo (PE) imaging generates anatomical cross-sectional images of the body, Figure 3.8. In the case of ultrasound colour flow imaging (CFI), a colour map depicting movement is superimposed on the PE image, Figure 3.9. This technique is mainly used to image blood flow. CFI techniques are like PE techniques in which information regarding the location of each target in the body, corresponding to each pixel in the image, is derived in the same way, but the returning echoes are analysed in terms of Doppler shift rather than amplitude. This technique estimates of velocity from the phase shifts or time delays between echoes from the same sample volume during subsequent pulses. A rate of change of phase is interpreted as a frequency shift and the velocity of the target is calculated from this frequency shift using the same equation that is used to interpret the true Doppler shift found in continuous wave ultrasound instruments, equation 3.3. In CFI, flow velocity estimation relies on the use of N narrowband pulses transmitted at a constant PRF to estimate the Doppler frequency and/or power. N is referred as the color ensemble length and usually varies between 6 and 16 pulses. In a typical case, each ultrasound line is insonified N times.

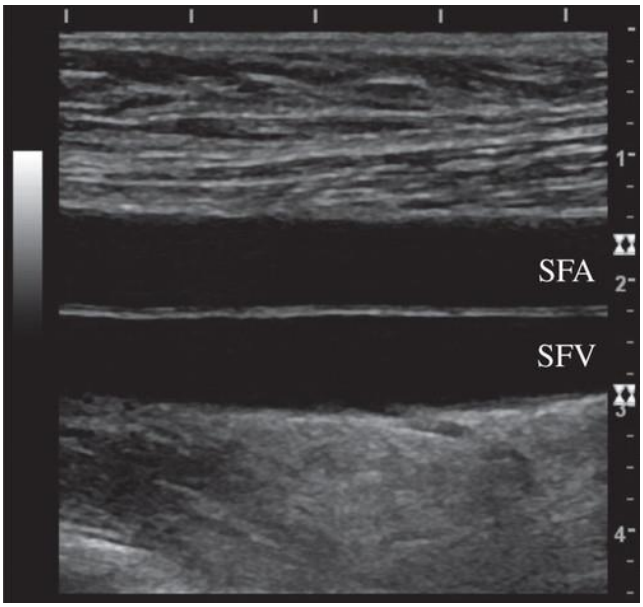

Figure 3.8: Pulse-echo image of the superficial femoral artery (SFA) and the superficial femoral vein (SFV) in the thigh of a healthy subject. The scale is calibrated in centimetres.

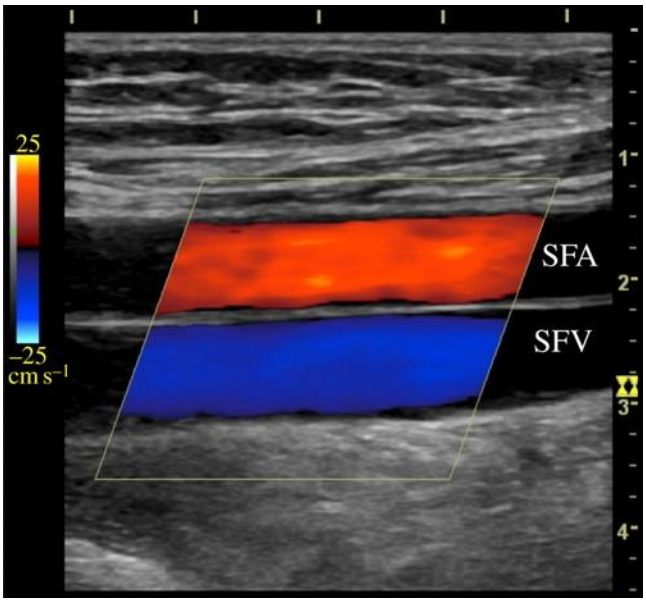

Figure 3.9: Colour flow image obtained by superimposing Doppler information on the pulse-echo image. The subject's head is to the left of the scan, and so the arterial flow is from left to right and the venous flow from right to left. The colour scale is calibrated in cm s^{-1} and shows that flow towards the probe is coloured as red-orange-yellow, while flow away from the probe is coloured in shades of blue. The angle of the colour box is inclined at an angle to the vertical to ensure that the Doppler angle is different from 90° .

Based on the Nyquist theorem, to avoid aliasing, the PRF must be at least two times the highest flow-related Doppler frequency of interest:

$$PRF_{flow} \geq 2F_s$$

The main steps of the processing are wall filtering to discriminate tissue echoes from the flow signal and velocity estimation, most based on autocorrelation methods. The sequencing strategy is

determined by the ratio between the maximum PRF achievable by the system at the considered depth (PRFmax) and the necessary PRF to detect the desired maximum flow velocity (PRFflow). This ratio gives the number of lines that can be sequentially insonified before going back to the first insonified line:

$$N_{lines} = PRF_{max} / PRF_{flo}$$

To generate a color flow image that contains more lines than Nlines, the image is subdivided into several segments of Nlines, and the color sequence and processing are done sequentially for all segments as illustrated in Figure 3.10. The number of firings necessary to compute a full color flow image is given by the following formula:

$$N_{FiringsC} = N_{lines} \cdot N_{Segments} \cdot N \quad (3.6)$$

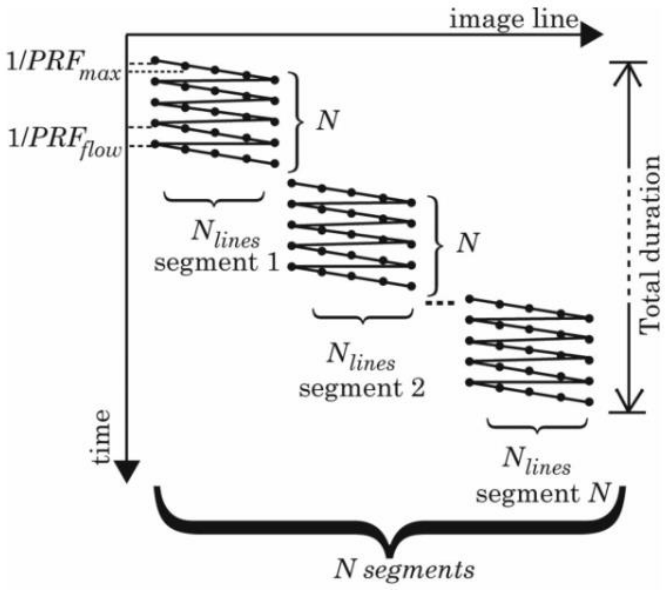

Figure 3.10: Process to generate a color flow image.

Acquisition and processing are done sequentially line by line as shown in Figure 3.11. The main processing steps are clutter filtering to extract Doppler blood flow signals from tissue echoes, and estimation of the mean flow velocity, using correlation-based methods.

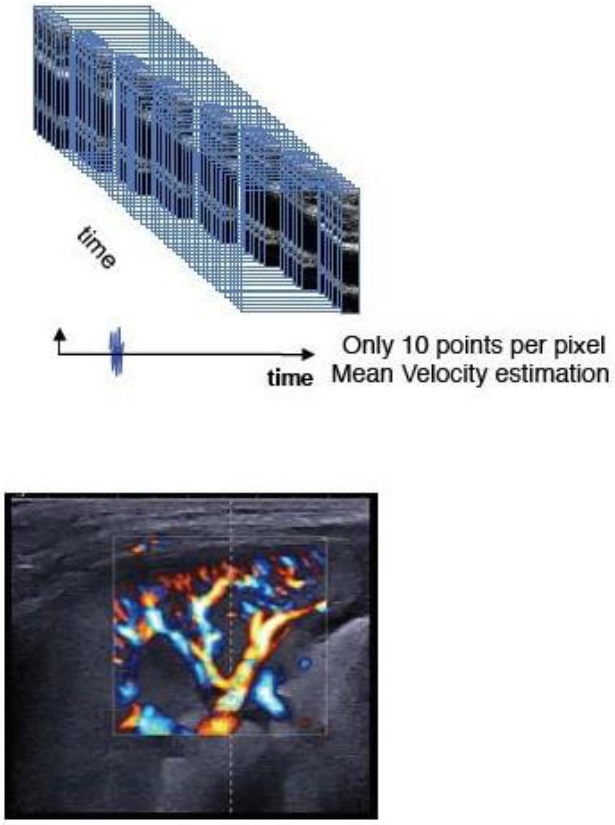

Figure 3.11: Data acquisition and processing in CFI

3.3.1 Clutter Filter for Ultrasound Color Flow Imaging

In ultrasound Doppler blood flow measurements, the signal scattered from blood is corrupted by signals scattered from muscular tissue. This clutter signal is typically 40-100dB stronger than the signal from blood. The signal scattered by the rapidly moving blood cells has a larger Doppler frequency shift than the signal reflected from slowly moving tissue. A high-pass filter is used to separate the signals from blood and tissue. To get adequate frame rates in 2D color flow imaging, only $8 - 16$ samples are generally available for high-pass filtering. All these algorithms consider only the steady state frequency response. For the short signals available in color flow imaging, the transient response is significant, and the steady state response cannot be used to compare the filters.

3.3.1.1 Finite Impulse Response Filter

The simplest type of clutter rejection filter is the single-echo canceller where, the output is derived by subtracting each successive echo from its predecessor. Signals from targets that are stationary should be unchanged and therefore will be cancelled, whereas those from targets that have moved will change and therefore not be subject to the same degree of cancellation. In practice, the single-echo canceller is inadequate for most CFI applications because of its poor roll-off (6 dB/octave) and wide transition band. The roll-off of the simple echo canceller could be increased by cascading two such filters, but this only impairs the transition band problem. More complex finite impulse response (FIR) filters are designed with much narrower transition bands, but this requires the use of much higher-order filters involving large numbers of data samples, which are not available in CFI applications.

3.3.1.2 Infinite Impulse Response Filter

The frequency characteristics of output values must be discarded before the data becomes valid. That is not possible in CFI applications of digital filters can be dramatically improved using infinite impulse (IIR) filters. IIR filters tend to have long transient responses, meaning that, unless appropriate steps are taken to initialize them, when a new signal is applied to the filter, a large number *Bjaerum, 1997)*.

4.3.1.3 Regression filter

A regression filter calculates the best least squares fit of the signal to a set of curve forms modeling the clutter signal and subtracts this clutter approximation from the original signal. Hoeks et al. introduced regression filters based on the assumption that the slowly varying clutter components of the Doppler signal can be approximated by a low-order polynomial, which can be found using least-squares regression analysis *(Hoeks, 1991)*. Later, Bjærum and Torp *(Bjaerum, 1997)* described an adaptive regression filter performing significantly better than a standard regression filter under some circumstances *(Bjaerum, 1997)*.

4.3.2 Velocity estimation

Once the clutter signals have been rejected, the I and *Q* components of the Doppler signal are further processed to generate estimates of power, frequency, and bandwidth. CFI systems do not use the Doppler shift frequency of individual pulses of ultrasound; this is because other mechanisms such as frequency-dependent attenuation and frequency-dependent scattering significantly change the spectrum of the pulse and make it impossible to estimate the change due simply to the Doppler effect. Instead, CFI systems rely on estimating the rate of change of phase of the signal returning from a given sample volume, or, alternatively, the change in the round-trip time from the transducer to a defined group of scatterers. Both methods have been implemented on commercial machines in the past, but now rely on techniques for estimating rates of change of phase. A simple model for the change in phase can be derived from using the time shift of the scatterers between pulse emissions. The axial motion Δz along the ultrasound beam between two pulse emissions is equal to:

$$\Delta z = |v|\cos(\theta)|Tprf = Vz\,Tprf \tag{3.7}$$

where T_{prf} is the time between two pulse emissions. This translates into a time shift t_s between the two received signals as:

$$t_s = \frac{2v_z}{2} Tprf \ , \tag{3.8}$$

and this delay will increase as a function of emission number *i*. Emitting a sinusoidal signal will then result in a received signal r (t, i) from a single moving scatterer given by:

$$r(t,i) = asin\left(2\pi ft\left(t - \frac{2D}{C} - its\right)\right) = \text{a sin}\,(2\pi ft\left(t - \frac{2D}{C} - \frac{2vz}{c} iTprf\right)) \tag{3.9}$$

where *D* is the initial depth of the scatterer and *the* amplitude of the scattered signal. Setting the measurement time to a fixed value t_m corresponding to a fixed measurement depth gives:

$$r(t,i) = asin\left(2\pi ft\left(tm - \frac{2D}{C} - its\right)\right) = -\text{a sin}\,(2\pi\left(t - \frac{2vz}{C} ft\ i\ Tprf - \phi\text{m}\right)) \tag{3.10}$$

where iT_{prf} now corresponds to sampling time and $\phi_m = 2\pi f_t(t_m - (2D/c))$ is a fixed-phase factor. The frequency f_p of the received signal is, thus, directly proportional to axial blood velocity and is given by:

$$f_P = \frac{2v_z}{c} f_t \tag{3.11}$$

The signal from a single scatterer passing the sampling point is illustrated on Figure 3.12. On the left is seen the individual received radiofrequency (RF) signals, and on the right the sampled signal from extracting one sample from each RF line at the depth of interest. The shape of the pulse is preserved

on the right, and its frequency is determined by how fast the scatterer passes the sampling point. A large velocity will compress the pulse and give a high frequency, and a low velocity will elongate the pulse and result in a low frequency.

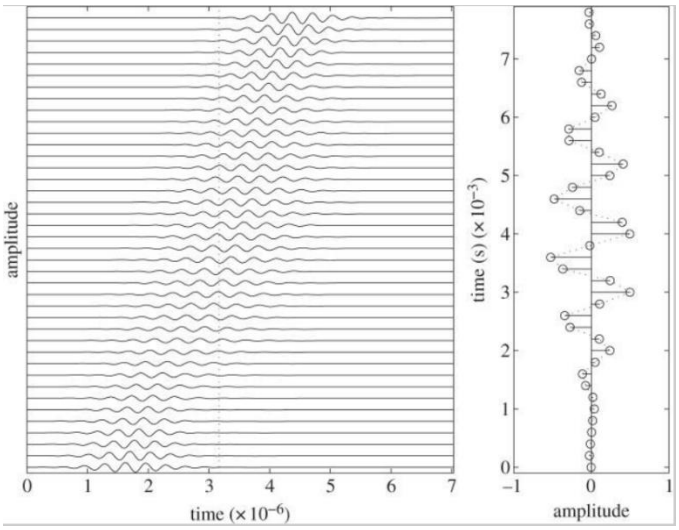

Figure 3.12: Signal from a single scatterer passing the sampling point. Left, RF signal, Right the sampled signal from each RF line.

After complex demodulation and sampling, the received signal r_c can be written as:

$$rc(i) = a \exp\left(-j2\pi \frac{2vz}{c}\ ftiTprf - \phi m\right) = a\ exp\ (\text{-j}\phi(\text{i}))=\text{I(i)+JQ(i)} \tag{3.12}$$

As for clutter rejection, the small number of samples available for each frequency estimate presents a number of technical challenges, and although a number of algorithms have been suggested as being useful for estimating the derivative of phase, by far the most widely is the autocorrelation technique introduced by Namekawa *et al*. and Kasai *et al*. Fig.3.13 illustrates the position of a rotating signal vector during two adjacent samples $i-1$ and i, with in-phase components $I(i-1)$ and $I(i)$, and quadrature components $Q(i-1)$ and $Q(i)$. The angular frequency ω of the rotating vector is defined as its rate of change of phase:

$$\omega = \frac{d\phi}{dt} \approx \frac{(\phi(\mathrm{i})-\phi(\mathrm{i}-1))}{Tprf} \tag{3.13}$$

The tangent of the phase difference $\phi(i) - \phi\,(i-1)$ may be written in terms of the ratio of the sine and cosine of the phase difference according to

$$tan(\phi(\mathrm{i}) - \phi(\mathrm{i}-1)) = \frac{sin(\phi(\mathrm{i})-\phi(\mathrm{i}-1))}{cos(\phi(\mathrm{i})-\phi(\mathrm{i}-1))} = \frac{sin(\phi(\mathrm{i})\cos\phi(\mathrm{i}-1))-cos\phi(\mathrm{i})sin\phi(\mathrm{i}-1)}{cos(\phi(\mathrm{i})\cos\phi(\mathrm{i}-1))-sin\phi(\mathrm{i})sin\phi(\mathrm{i}-1)} \tag{3.14}$$

If the sin and cos terms are now expressed as the in-phase and quadrature magnitudes of the vectors, and an average frequency calculated by summing over a number of adjacent pulse pairs, then the mean angular frequency can be written as:

$$w = \frac{1}{\mathrm{Tprf}} \arctan\left[\frac{\sum_{I=1}^{N} Q(i)I(i-1)-I(i)Q(i-1)}{\sum_{I=1}^{N} I(i)I(i-1)+Q(i)Q(i-1)}\right] \tag{3.15}$$

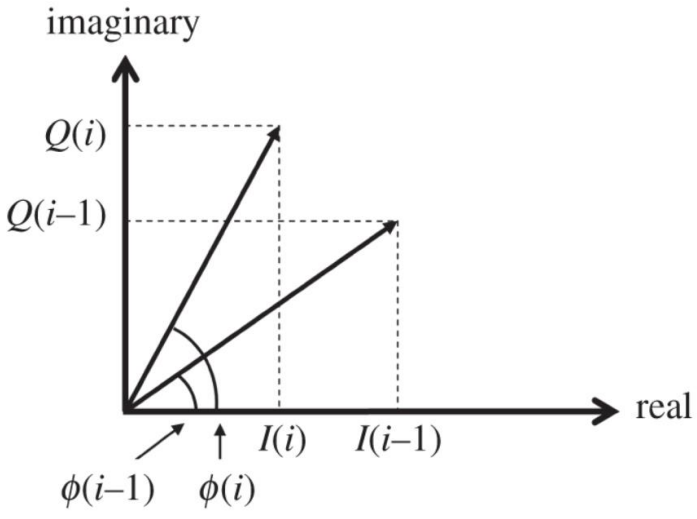

Figure 3.13: Position of a rotating signal vector during two successive samples $i-1$and i, showing the in-phase components $I\ (i-1)$ and $I(i)$ and quadrature components $Q\ (i-1)$ and $Q(i)$.

Major advantages of the autocorrelator are that it gives an unambiguous output for narrowband signals over the range of $\pm\pi$ radians, and that it is well behaved with wideband signals with mean frequencies close to $\pm\pi$ radians because it correctly accounts for partial aliasing in a continuous spectrum. The output of the autocorrelation estimator is also ideally unbiased as the addition of white noise to the signal does not affect the autocorrelation at finite lags; however, the use of clutter rejection filters will colour the system noise leading to a bias in the mean frequency estimate. This bias can be minimized using clutter filters with good roll-off characteristics. A significant advance on the simple autocorrelator as a means of quantifying blood flow velocities was introduced by Loupas *et al.*and differs from the simple method in two distinct ways. Firstly, the estimate of the Doppler frequency is formed by processing samples from a number of axial depths, and, secondly, the axial velocity is calculated from the Doppler equation using explicit estimates of both the mean Doppler and mean RF frequencies at each range gate location. The two-dimensional autocorrelation estimator has considerable advantages over the conventional one-dimensional method, which implicitly assumes that the mean RF frequency is constant and equal to the centre frequency of the transmitted pulse. In practice, the received RF frequency varies considerably owing to both the stochastic nature of the backscattered signal and the effects of frequency-dependent attenuation and scattering, which lead to perturbations in the Doppler frequency, that tend to track the RF fluctuations. If, on the other hand, velocity is calculated from the ratio of the measured Doppler shift frequency to the measured RF frequency, these effects are at least partially compensated for, and a more stable estimate of velocity obtained. Although methods based on measuring the rates of change of phase and particularly autocorrelation methods are now widely used in commercial machines, colour flow mapping can also be implemented using time domain-based techniques such as cross-correlation. These techniques are based on measuring changes in the round-trip time from the transducer to a defined group of scatterers. To implement this, short segments of the echo signals from each pulse are compared with similar segments of previous pulses from approximately the same range, to find the best match and hence to estimate the inter-pulse target displacement t_s. This process is not perfect as no two subsequent scattering signatures are identical because of components of motion perpendicular to the ultrasound beam and because of velocity dispersion within the range cell.

3.3.3 Post Processing, Priority encoding and Display

Once the mean frequency, power and variance of the Doppler signal have been calculated, their values are stored in a colour frame memory before being further processed and combined with PE information to form the final composite image. Doppler signals are stochastic in nature, the estimates of signal parameters vary in a random fashion, and therefore various post-processing techniques such as linear and/or nonlinear, spatial and temporal averaging of the Doppler parameter data are employed to prevent rapid fluctuations and drop-out in the final displayed colour images.For every pixel in the final image (within the region covered by the colour box), there will be both grey-scale PE information and colour Doppler data available. The function of the priority encoder is to determine whether the Doppler data are valid, whether there is any real flow or movement present, in which case these data are given priority, otherwise the PE data are presented.

3.4 Evolution of Ultrasound: Ultrafast Imaging

This section refers to Bercoff et.al. (31)

In the history of ultrasound, many innovations have been developed since its establishment as a medical imaging device in the 1960s. The key innovation that launched the modality in the 1960s, is the real time imaging capability through mechanical scanning. Multichannel systems with electronic control of transducer arrays were developed in the 1970s. In the 1980s, flow analysis tools came to maturity through color flow imaging and quantitative Doppler modes (Pulse Wave Doppler - PWD). In the 1990's significant improvements in image quality were made possible with the introduction of real time compounding techniques and harmonic imaging. In the first decade of the 21st century, technology moved towards extensive miniaturization leading to the introduction of high performances portable devices. The figure 3.14 summarizes the evolution of ultrasound in the last decades.

Today a new technological breakthrough is ongoing. This results from the incredible demand in processing and display performances needed in the videogame industry. In addition to multicore architecture CPU's, new graphical processing units (GPU) allow parallel processing on thousands of channels simultaneously. In 2009, SuperSonic Imagine introduced the first full software-based ultrasound system: instead of increasing integrated hardware processing channels, all the processing is performed by the software unit (CPU and GPUs). The concept of processing channels disappears - the system can compute in parallel as many channels as required by the acquisition.

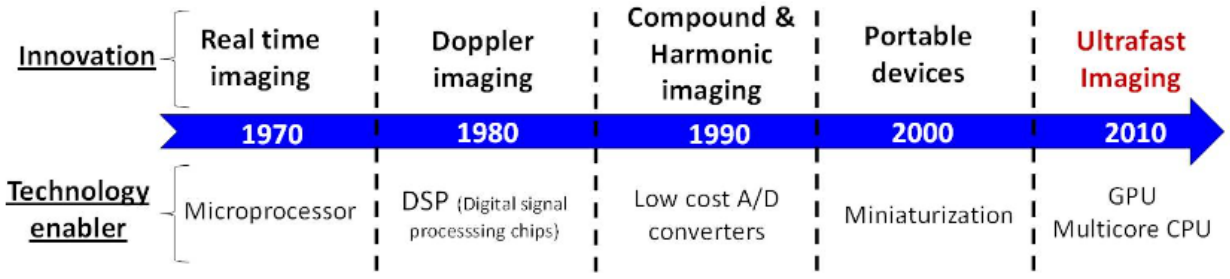

Figure 3.14. A few important innovations in ultrasound imaging and their corresponding technology

3.4.1 From Conventional to Ultrafast imaging: History

Ultrasound imaging is usually performed by sequential insonification of the medium using focused beams. Each focused beam allows the reconstruction of one image line. A typical 2D image is made of a few tens of lines (64 to 512). The frame rate of the imaging mode is set by the time required to transmit a beam, receive, and process the backscattered echoes from the medium and repeat that for all the lines of the image. Ultrasound system architectures were designed to process one image line at a time.

Limitations of the conventional approach appears as soon as higher frame rates are required, typically in echocardiography for the heart motion analysis, as well as in 3D/4D imaging where the number of lines become significant (~ a few thousands). Parallelization schemes have been considered to overcome these limitations. In the academic area this has been reported as soon as the late 70's (Delannoy, 1979; Shattuck, 1984; Von Ramm, 1991). Most current systems have multiline capabilities: for each transmit beam, several lines (typically from 2 to 16) are computed. Multiline processing can be used either to increase the frame rate (for echocardiography for example) either to increase the number of lines computed per image (for 3D imaging). With or without multiline capabilities, current ultrasound systems are built on a serialized architecture and images are reconstructed sequentially from several equivalent transmits.

Ultrafast imaging breaks this paradigm. An ultrafast imaging system can compute in parallel as many lines as requested and is therefore capable of computing a full image from one single transmit whatever the size and the characteristics of the image. In such a system the image frame rate is no longer limited by the number of lines reconstructed but by the time of flight of a single pulse to propagate in the medium and get back to the transducer. Table 3.1 gives typical frame rates for different ultrasound clinical applications using conventional and ultrafast architectures.

Table 3.1: Comparison between conventional and ultrafast imaging in three different application

Application	Typical imaging depth	Conventional architecture	Ultrafast architecture
Abdominal imaging	20 cm	20 Hz	3800Hz
Cardiac Imaging	15 cm	150 Hz	5000Hz
Breast imaging	5 cm	60 Hz	15000 Hz

To achieve ultrafast imaging, the image computation must be performed on a fully parallelized platform, typically a software-based platform. There are two technologically challenging aspects to building a fully software-based platform:

- The data transfer rate from the acquisition module to the processing unit. As raw (non beamformed) Radio Frequency (RF) signals are directly transferred to the PC, the data rate required to perform real time imaging is huge: several GigaBytes/s.
- The processing unit needs to be powerful enough to ensure real time imaging. As an example, conventional gray scale imaging requires 1 to 2 Gigaflops (multiplication + addition) per second.

The ultrafast architecture leverages this processing power by combining it with fast numerical links capable of transferring huge volume of data to these units. This combination allows the shift of the beamforming process from hardware to software, enabling full parallelization of ultrasound image computation.

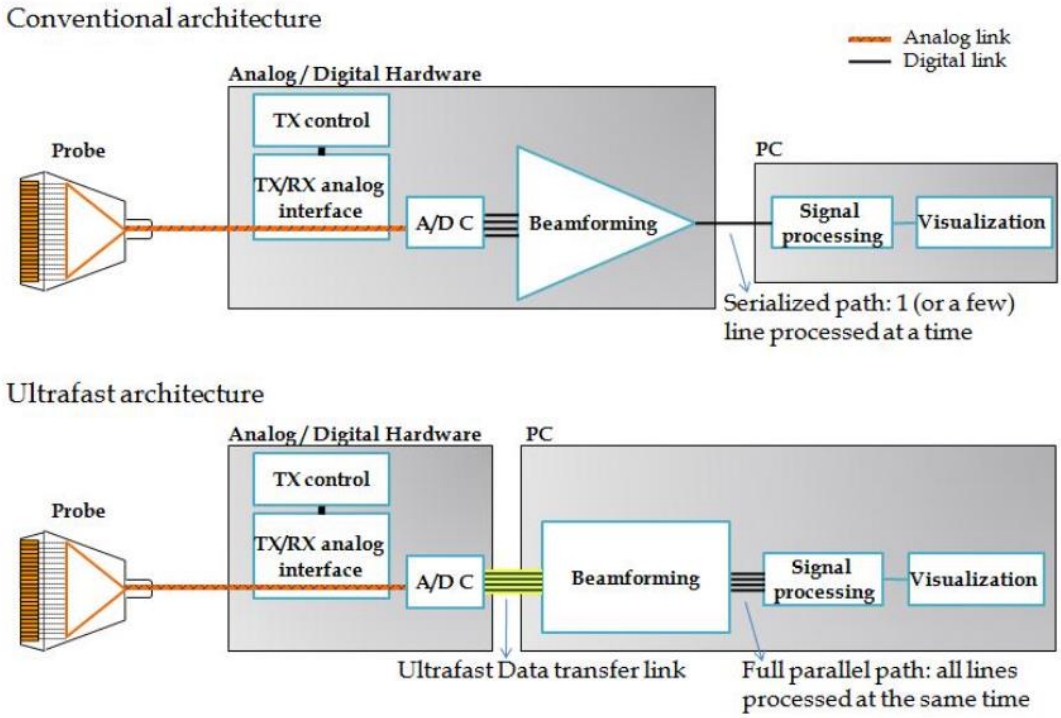

Figure 3.15: The architecture of an ultrafast system compared to a conventional one.

3.4.2 Ultrafast imaging using coherent plane wave compound

There are many ways to leverage an Ultrafast imaging architecture (Lu, 1998; Jensen 2005). SuperSonic Imagine's approach is based on the use of plane wave insonifications. A plane wave is generated by applying flat delays on the transmit elements of the ultrasound probe as illustrated on Fig. 3.16. The generated wave will insonify the whole area of interest.

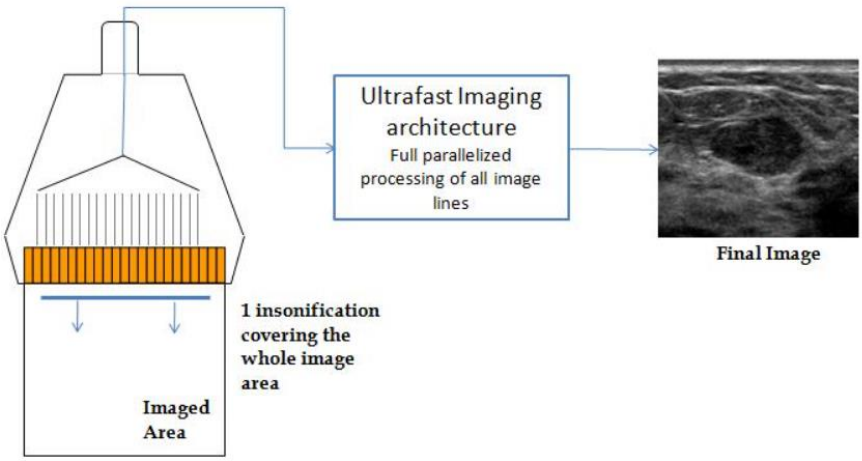

Figure 3.16: A plane wave is sent by a linear transducer and insonifies the whole region of interest. An ultrasound image is computed from this single insonification.

The backscattered echoes are then recorded and processed by the ultrafast scanner to compute an image of the insonified area. Plane wave imaging allows the computation of one full ultrasound image per transmit at the expense of the image quality. As the transmit focalization step is removed, the image contrast and resolution are reduced, as illustrated in the Fig.3.17.

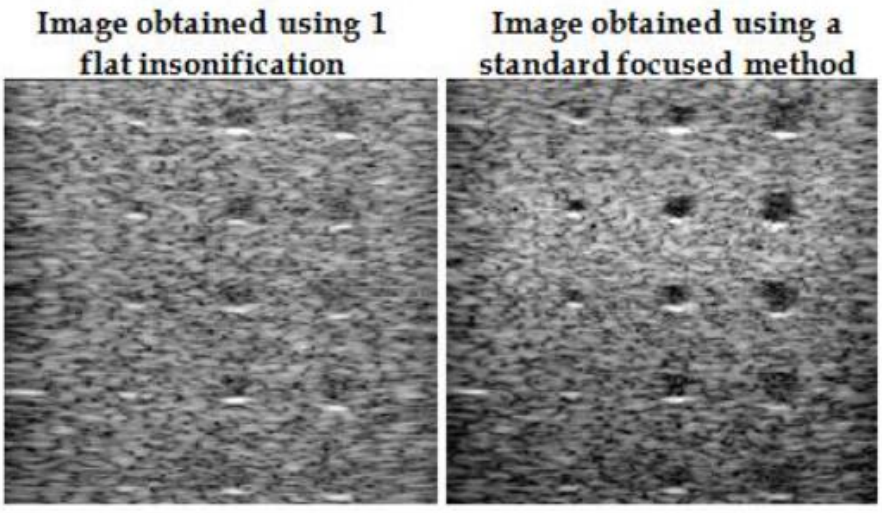

Figure 3.17: Image of a phantom with anechoic inclusion of different sizes with plane wave insonification (left) and standard focused method (right). The images were acquired with a 5 MHz linear probe.

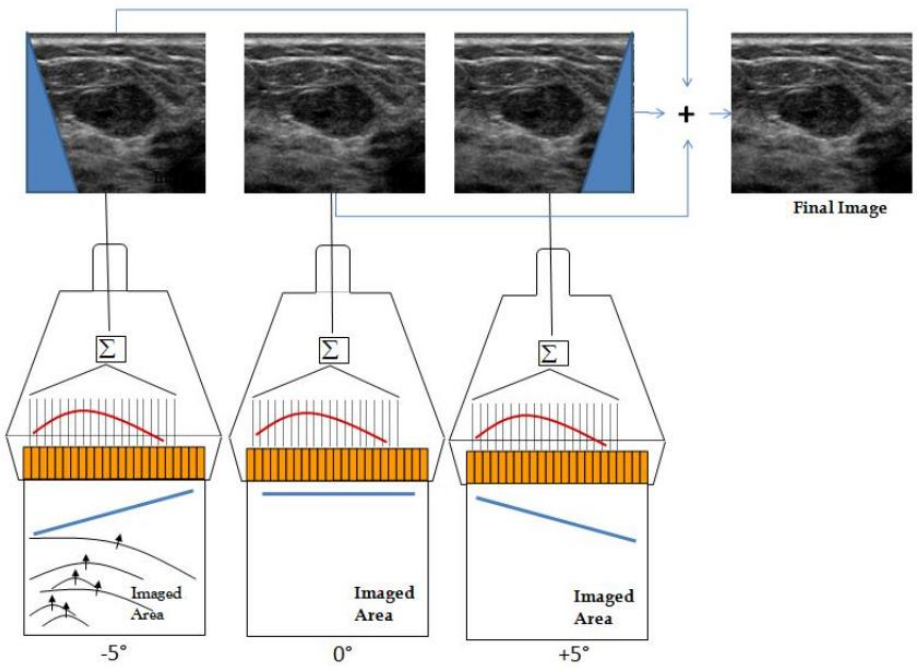

Figure 3.18: Ultrasound image obtained using ultrafast coherent plane wave compound

To overcome this limitation, several tilted plane waves are sent into the medium and coherently summed to compute a full image. Using this method, the transmit focalization step is retrospectively done by this summation (Fig. 3.18). The quality of the final image is therefore dependent on the number of angles used to reconstruct it as illustrated on Fig. 3.19. There is a trade off between the maximum ultrafast frame rate achievable by the mode and the image quality: the higher the number of angles, the better the image quality.

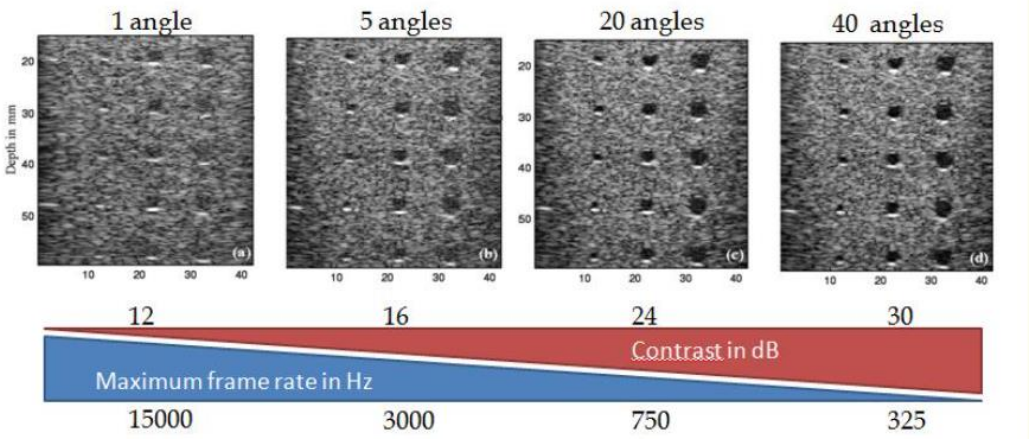

Figure 3.19: Image quality as a function of the number of angles used to compute the final ultrasound image for a 40mm depth image

The ultrafast compounded acquisition sequence presents several advantages:

- Firstly, the retrospective transmit focalization can be done dynamically for each pixel of the image increasing the homogeneity of the final image compared to physical insonification.
- Secondly, the number of firings required to obtain an image of a quality equivalent to a focused mode (in terms of contrast and resolution) is around 5 to 10 times lower (Montaldo, 2009). Therefore, frame rates of ultrasound imaging can be increased by the same factor using coherent plane wave strategies on an ultrafast system. Figure 3.20 shows an example of equivalent quality ultrasound images using the coherent plane wave approach and the focused one. Maximum reachable frame rates increase from 30 Hz to more than 300 Hz.
- Finally, by cleverly trading off the compromises in the image quality, imaging frame rates of a few thousands of Hz can be reached and allow a full new range of applications and innovations.

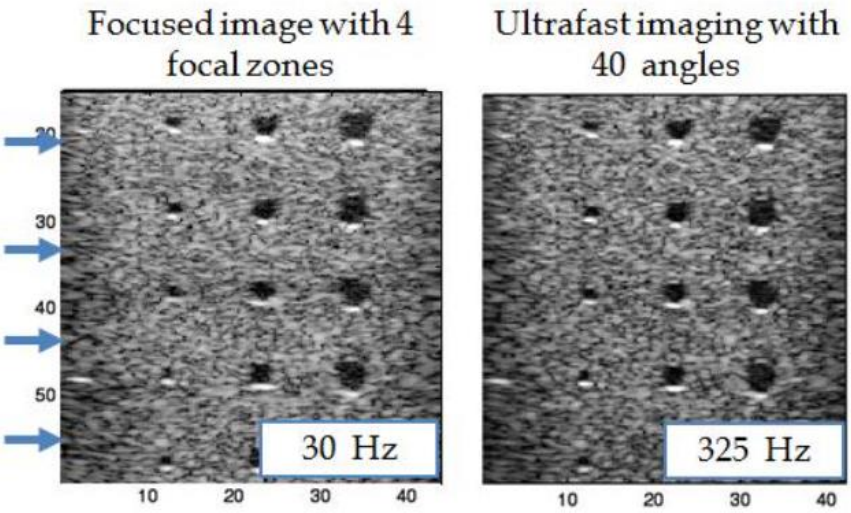

Figure 3.20: Ultrasound images using the focused approach and the coherent plane wave. The maximum frame rate increases from 30 Hz to 300 Hz

3.5 Power Doppler

This section refers to J.M. Rubin. Et al. "Power Doppler US: A potentially useful alternative to mean frequency- based color Doppler US" (32).

An alternative to standard mean-frequency color Doppler is a color Doppler technique that encodes the power in the Doppler signal in color. The primary advantage of using power is that the representation of random noise in the power mode is different from that in a mean frequency mode. This is because the noise always has uniformly low power due to the standard signal to noise requirements of a color Doppler scanner. This is fundamentally different from the random phase noise introduces when calculating the mean frequency shift. Because noise has uniformly low power, when power is encoded in color it raises the sensitivity of the color Doppler unit to image the noise floor, instead of seeing a random distribution of colors that represents any possible flow, only a uniformly colored background is imaged representing low power. Any true flow will have more power in the Doppler signal than does the noise, hence will pop out of the noise background (Fig.3.21).

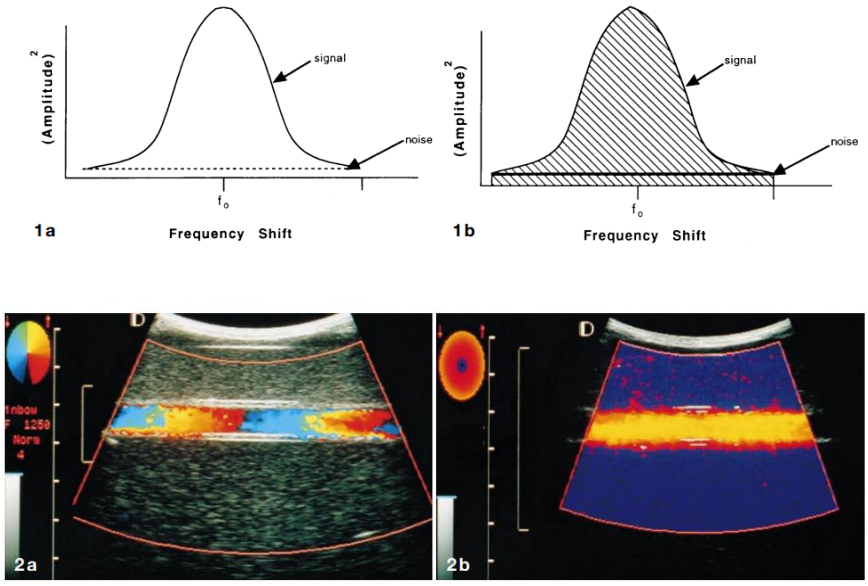

Figure 3.21. 1a Spectral plot for mean frequency flow estimation. The graph is spectral power, as a function of frequency shift. When the signal is weak, it begins to fall into the noise floor which is white in character, contains all frequencies. 1b Same plot except crosshatching represents the integral under the curve. The noise integral is always low, making it possible to separate the signal from the noise when the signal is weak. Flow tube showing aliasing in 2a mean frequency mode and 2b no aliasing in power mode.

A significant advantage of power Doppler imaging is that it does not alias. This is because the total power in the signal is represented by the integral under Doppler power curve also called the power spectrum. The mean frequency can alias when it exceeds PRF/2, but the integral of the power spectrum does not change. Power Doppler imaging is relatively angle independent, certainly compared with mean frequency color Doppler. This is because power is based on the integral of the Doppler power spectrum. The power in the Doppler signal is related to the number of moving scatterers, red blood cells in the absence of contrast agents, producing the recorded Doppler shifts. If the angle of insonification relative to these red blood cells changes, their mean Doppler shift will change, but the power will not change. It can be seen as changing the shape of the frequency distribution, but not the integral. Thus, a power image will change very little with changing angle Fig.3.22.

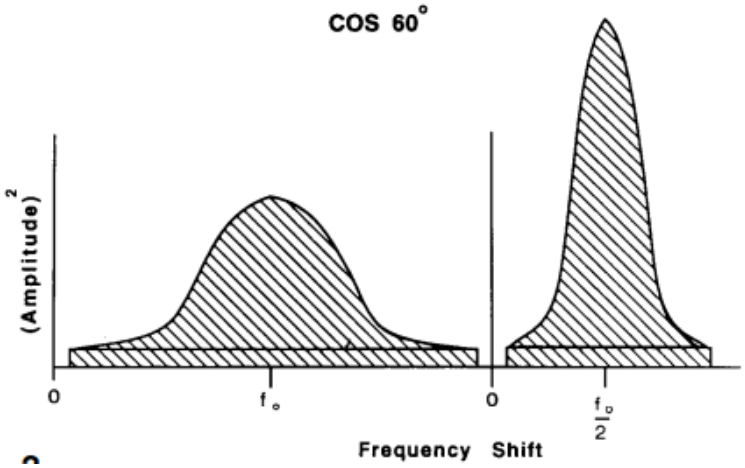

Figure 3.22: The left plot represents the spectral power distribution function at zero degrees, and the right one represents the distribution when sampling at 60 degrees. Each frequency shift in the left-hand distribution is multiplied by half, so the mean value on the left, fo, is exactly twice the mean value on the right, fo/2; however, the areas are unchanged. Hence, the plot on the left is broad and short, whereas the one on the right is tall and thin. Thus, the mean frequencies appear different depending on the angle of insonation, but the power remains essentially unchanged. The only difference is the amount of signal that falls into the wall filter.

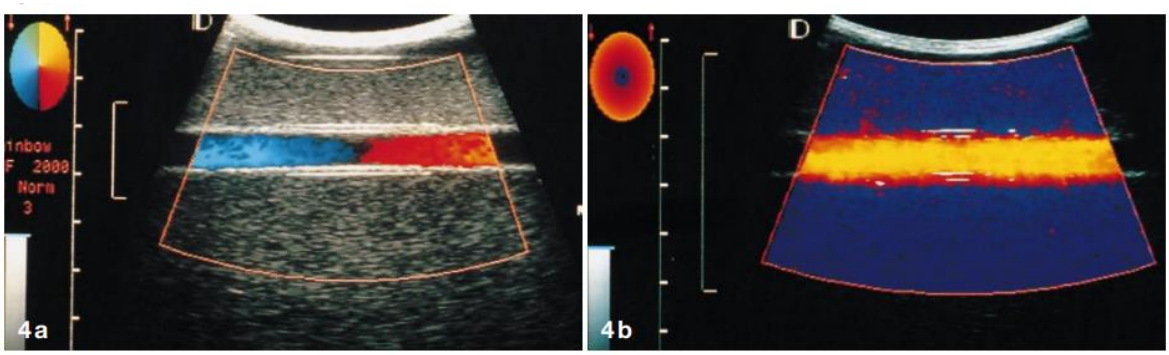

Figure 3.23: 4a Flow tube in mean frequency showing color change as flowing medium moves across the aperture of the scanhead. 4b Same flow tube in power mode showing essentially no change across the tube.

The advantages of power mode include a better boundary detection, improved quantification of vascularity, better 3D depiction of blood vessel anatomy, and advantageous properties of blooming in power mode with contrast agents. The first two advantages are both based on the fact that power mode is a continuous estimator of the amount of blood in a pixel compared with standard mean frequency color Doppler, which is a bistable estimator of pixel blood content. Bistable means that an arbitrary threshold, the color-write echo priority, is defined for color Doppler below which no flow is written and above which a pixel is written as entirely containing flow. Although the functional relationship is complex, the amount of Doppler power in a pixel corresponds to the amount of moving blood that is present. Hence, different amounts of blood in a pixel will appear with different powers. Thus, is obtained a continuous map of vascularity. In addition, it is possible to compensate the Doppler power for depth and transducer affects.

Power mode's natural ability to represent pixel blood content continuously leads directly to improved representations of boundaries compared with mean frequency color Doppler. Power mode depicts continuous smooth representation of boundaries, making boundaries very easy to see (Fig. 3.24). In 3D the lack of aliasing and directional information is an advantage for power mode. In power mode, vessels look continuous and are easy to track visually no matter what the perspective. A disadvantage of power imaging is that it provides no information about speed of flow or direction of flow. Color Doppler is often used only to localize vessels for placement of sample volumes or to determine the presence or absence of flow. In these cases, this limitation of power Doppler presents no problem. The biggest limitation is that the method is extremely motion sensitive. Minimal soft tissue motion can seriously degrade the image. This is since power Doppler is a high-sensitivity technique in which

any motion is detected. Soft tissue motion can be difficult to distinguish from blood flow. Very strong soft tissue scatterers can still give a structured noise that can look like flow-containing objects under certain conditions. This makes it mandatory that additional sophisticated soft tissue motion suppression schemes be used with this technique.

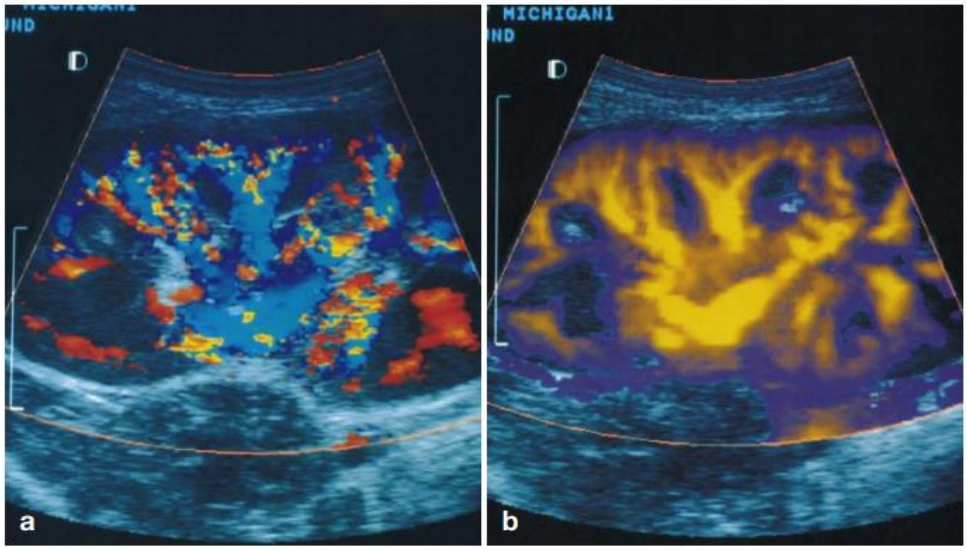

Figure 3.24: Image of renal transplant in power mode and mean frequency. a) Mean frequency image shows less flow in the cortex of the vessel margins. b**)** Power Doppler image of the same kidney at same PRF. The gain is set higher in power mode. There is more flow depicted in the renal cortex, and the vessel are better visualized.

3.6 Ultrafast Doppler Imaging

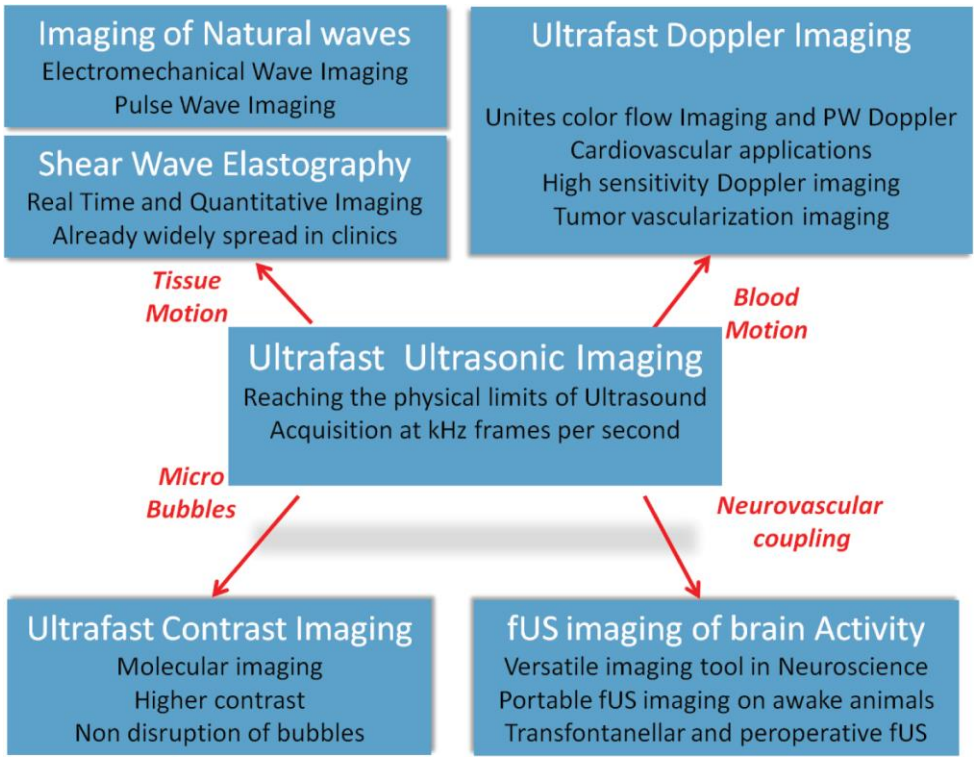

Ultrafast imaging using unfocused transmissions offers a technologically disruptive solution to the problem of imaging and quantification for blood flow characterization.

Bercoff *et al*. has demonstrated that ultrafast Doppler based on plane-wave imaging could disrupt current incompatibilities that exist between imaging and quantification. Indeed, planewave transmissions give access to high-precision characterization of complex vascular and cardiac flows because all pixels of the 2-D ultrasonic image rely simultaneously on a very high frame rate and a large number of temporal samples. One major advantage of ultrafast Doppler for use in routine vascular imaging lies in the fact that all blood flow dynamics can be acquired during a limited number of cardiac cycles (typically one to three), and all PW Doppler pixel data for the whole image can be retrieved from the ultrafast sequence.

The use of ultrafast imaging during Doppler examinations permits the following:

- Adjustable positioning of the PW Doppler window without requiring the probe to remain in the same imaging plane for a prolonged period of time;
- Several independent PW Doppler windows can be added, corresponding to simultaneous acquisition at different locations and allowing comparison ofblood flow at different locations without requiring several successive conventional PW Doppler exams.
- Blood flow dynamics within the same cardiac cycles can be compared in different PW Doppler windows in a synchronous manner.
- 2-D vector flow dynamics can be acquired over entire regions within a single cardiac cycle; and
- Imaging of blood flow and tissue motion in arteries can be performed simultaneously.

These factors contribute to a more refined analysis of complex blood flows. An example of ultrafast Doppler imaging in the human carotid is presented in Fig. 3.25. The ability of ultrasound to yield a very large amount of new information makes it ideal for detecting very subtle blood flow in small vessels. Indeed, the ultrafast acquisition of backscattered echoes within a single cardiac cycle increases the number of temporal samples in each pixel of the blood flow image. This accumulation of data results in the fact that Doppler shows higher sensitivity for slow flow rates. Potential clinical targets of Ultrafast Doppler include neovascularization imaging in tumors without the requirement for contrast agents (for example in breast cancer diagnosis). Osmanski *et al*. demonstrated *in vivo* that small vessels can be detected in cardiac muscle without the need to inject contrast agents. Also, Denarie *et al*. studied the influence of frame rate on coherent plane-wave compounding in rapidly moving organs and proposed a correction method for the degradation of coherent synthetic summation that occurs in these types of organs.

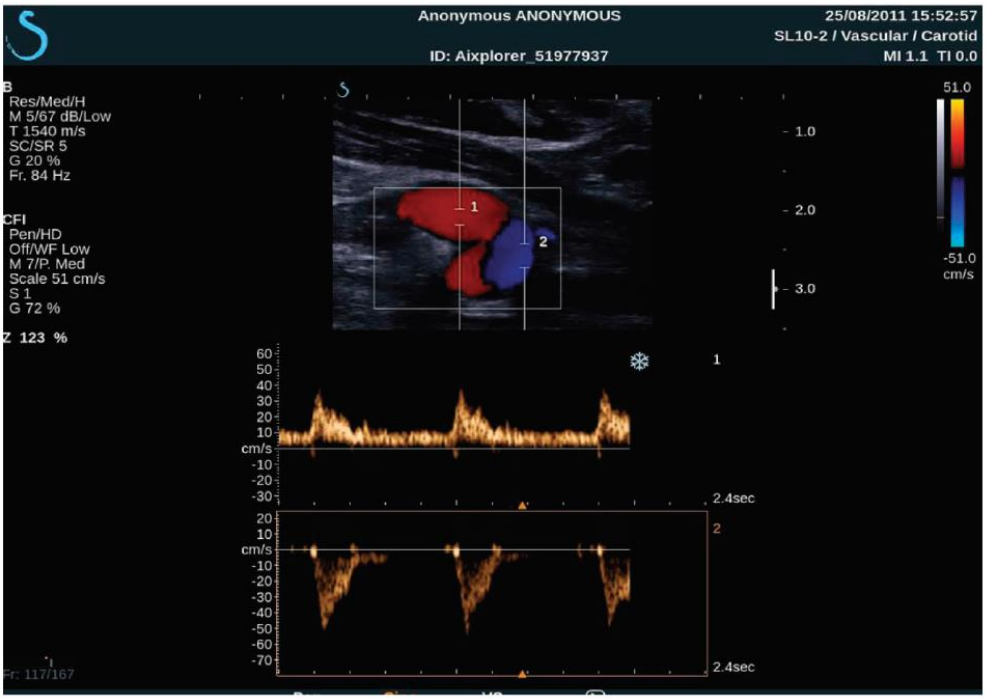

Figure 3.25: Blood flow quantification from ultrafast acquisitions

4. High Definition Microvessel Imaging Technique

This section refers to Demenè et al. (33) and Bayat et.al (21)

4.1 Spatiotemporal singular value decomposition clutter rejection

Extensive work has been done over the decades in order to suppress clutter signals originating from stationary and slowly moving tissue as they introduce major artifacts in ultrasonic blood flow imaging. The reason why clutter filters initially fail is due to the underlying assumption on which they are built. In the early history of Color Flow Imaging (CFI), clutter filtering has always assumed that tissue signal and blood flow signal have completely differing spectral characteristics: tissue motion is supposed very slow or non-existent whereas red blood cells are fast moving scatterers, meaning that demodulated tissue signal and blood signal have non-overlapping spectra centered on the zero frequency and the Doppler frequency respectively.

Several techniques have been developed to adapt to each Doppler imaging situation by compensating background tissue motion: by estimating first tissue velocity and down-mixing the ultrasound temporal signal via a phase correction, the spectrum can be shifted so that the center frequency of the tissue signal match the zero frequency. The signal is then processed using a classical fixed cut-off filter to remove tissue echoes. In all these methods, only the temporal information has been used because the hypothesis used to discriminate tissue signal and blood scatterers signal focused on their different spectral content. But also, the spatial characteristics of tissue signal are different from those of blood scatterers. Tissue is less deformable than a red blood cell arrangement in plasma, and a small movement of tissue can be seen as a spatial shift of a speckle pattern whereas a movement of red blood cells implies a reorganization of the scatterers generating a different speckle pattern.

Tissue signal has a higher spatial coherence than blood signal in ultrasound imaging. The singular value decomposition (SVD) takes benefits of the different features of tissue and blood motion in terms of spatiotemporal coherence and strongly outperforms conventional clutter rejection filters based on high pass temporal filtering. Whereas classical clutter filters operate on the temporal dimension only, SVD clutter filtering provides up to a four-dimensional approach (3D in space and 1D in time).

4.1.1 The Different Components of The Ultrasound Signal

An Ultrafast Doppler acquisition can be represented under the complex valued variable s (x, z, t), where x stands for the lateral dimension (along the transducers array), z stands for depth in the medium in front of the ultrasonic probe, and t stands for time (sampled at a frequency noted Frame Rate). It is assumed that this signal can be described as the summation of three contributions: c the clutter signal, b the blood signal, and n the electronical/thermal noise.

$$s(x, z,t)=c(x,z,t)+b(x,z,t)+n(x,z,t). \quad (4.1)$$

Those three contributions have different spatial and temporal characteristics. The classical approach consists in assuming that blood signal is a high temporal frequency signal, and that tissue signal is a low frequency signal.

4.1.2 Covariance Matrix of Neighboring Pixels

The temporal signal in one pixel exhibits low frequency fluctuations corresponding to tissue movement (in the imaginary part of the signal the three slow oscillations observed are due to tissue moving when the heart beats) and high frequency fluctuations due to actual blood cells motion. In order to compare spatially close temporal signals, a simplified signal is calculated:

$$\tilde{s}_{(x,z,t)} = s(x,z,t)\,\overline{s_{(x,z,t)}}\,*/|\overline{s_{(x,z,t)}|2} \quad (4.2)$$

where $\bar{s}$ is the time average value of s and $*$ stands for complex conjugate. This simplified illustrative representation enables to get rid of any phase shift (via the product with the complex conjugate of the time averaged signal) and of amplitude difference (via the division with the squared

modulus) between two-pixel signals; and consequently, to compare signals only on the basis of their shape. Fig.4.1 shows that in neighboring pixels, simplified signals present very similar low frequency variations (tissue motion), whereas the rapid fluctuations (blood motion) do not present the same pattern from one pixel to another. This aspect is displayed in Fig.4.2, where the nine-pixel signals of the second neighborhood of Fig. 4.1 are separated in blood (HF) and tissue (LF) signal with a temporal filter. Tissue signal is highly correlated and the covariance matrix of the nine signals exhibits a high degree of correlation, whereas the blood signal covariance matrix is almost diagonal, meaning that blood signal is poorly spatially coherent, even at a very local scale.

Contrary to tissue signal, blood signal is not assumed to have high spatial coherence. In addition, tissue signal energy is much higher (10 to 50 dB) than blood signal energy, and a separation method based on covariance estimation certainly finds the highest covariance values for the tissue signal. This discrimination based on covariance estimation can be performed using the singular value decomposition of raw data.

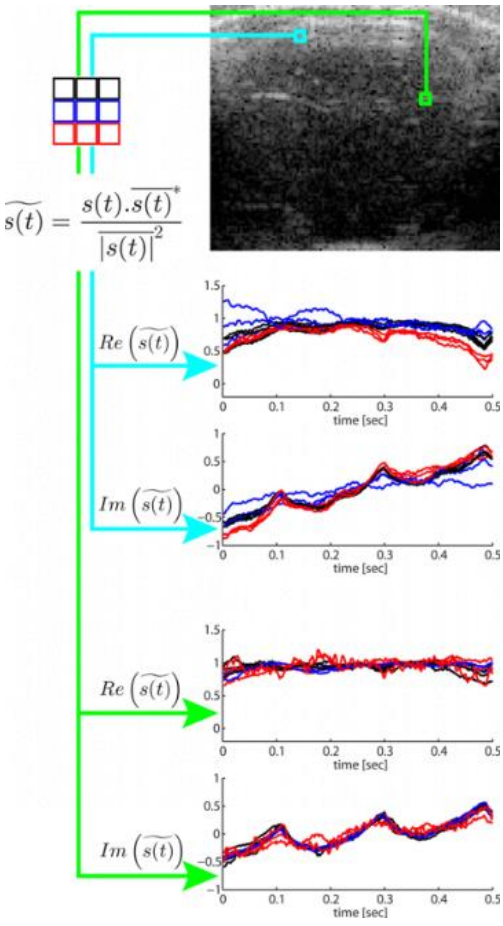

Figure 4.1: Example of an ultrafast acquisition. The top image depicts s(x, z,t=0) of an Ultrafast acquisition acquired during 0.5 s at a Frame Rate of 500Hz, on the brain of a thinned skull rat.To have an insight into the temporal dimension of this Ultrafast acquisition, two neighborhoods of nine pixels have been chosen in the image (green and cyan squares). Inside each pixel, the simplified signal s~(x, z,t) is calculated to get rid of phase difference and amplitude difference from one pixel to another. s~ is then plotted with color respective to the position in the nine-pixel neighborhood (black, blue or red). This illustrates that signal in close pixels is very similar in shape.

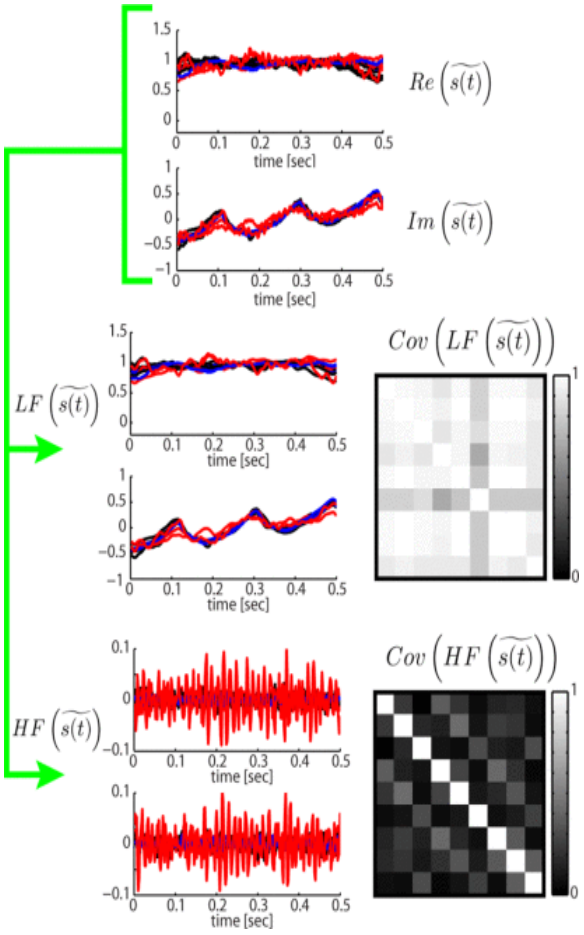

Figure 4.2 **:**The same data than in the green nine pixel neighborhood of Fig. 4.1 are filtered using a 50hz cut off 4th order butterworth filter typically used to discriminate between tissue and blood flow signals, and on the graphs it can be observed that the low frequency (lf) part of the nine pixel temporal signal are really similar in shape and seem highly correlated, whereas the blood signal (hf) seem highly decorrelated. On the right are displayed the 9×9 covariance matrix of the normalized zero-mean complex signals, for the low frequency and high frequency part respectively. HF blood signal is indeed highly decorrelated compared to LF tissue signal.

4.1.3 Singular Value Decomposition of Ultrafast Ultrasonic Data

Considering the spatiotemporal matrix form of s(x,z,t) corresponding to the raw data cineloop acquired during an ultrafast acquisition. s(x,z,t) corresponds to set of (nx×nz×nt) samples where nx, nz and nt are respectively the number of spatial samples along x-direction, the number of spatial samples along z-direction and the number of time samples. The raw data matrix is reshaped under a Casorati matrix form by transforming time series data into a 2D space-time matrix form S with dimensions (nx×nz, nt).

The singular value decomposition (SVD) of the Casorati matrix S consists in finding the three matrices such as:

$$S=U\Delta V^{*} \tag{4.3}$$

Where V is a non-square (nx×nz,nt) diagonal matrix, U and V are orthonormal matrices with respective dimensions (nx×nz,nx×nz) and (nt, nt) and $*$ stands for the conjugate transpose. Columns of U and V matrices correspond respectively to the spatial and temporal singular vectors of S.

The singular value decomposition (SVD) is the decomposition of a matrix S into a weighted, ordered sum of separable matrices Ai, this means that the matrix S can be written as an outer product of two vectors Ai=Ui⊗Vi. Specifically, the matrix S can be decomposed as:

$$s = \sum_i \chi_i A_i = \sum \chi_i U_i \otimes V_i \tag{4.4}$$

Thus, the SVD can be used to find the decomposition of an ultrafast ultrasonic dataset into separable space and time filters. Here Ui and Vi are the ith columns of the corresponding SVD matrices, λi are the ordered singular values, and each Ai is a separable matrix. The number of non-zero λi is the rank of the matrix. Each column Vi corresponds to a temporal signal with length nt and each column Ui corresponds to a spatial signal with length nt. Each vector Ui describes in fact a 2D spatial image Ii with dimensions (nx,nz).

The SVD of S decomposes the field into a sum of separable images Ii (characterized by a vector Ui) that are independently modulated by a temporal signal Vi.

Thus, thanks to the SVD processing, the spatiotemporal cineloop s(x,z,t) corresponding to ultrasonic raw data can be rewritten as:

$$s(x,z,t) = \sum_{i=1}^{rank(s)} \lambda i I_i\,(x,z) V_i(t) \quad (4.5)$$

In this decomposition, tissue displacements is described mainly in the first singular values and singular vectors as their high spatiotemporal coherence insures that a large number of spatial pixels will exhibit the same time profile. On the contrary, blood signal is found in lower singular values as they exhibit much lower spatiotemporal coherence. Thus, filtering the data using the SVD approach consists in calculating:

$$s^f = sv\dot{I}^f v^* = U\Delta^f v^* \quad (4.6)$$

Where Sf is the filtered data set and If is a matrix filter.

4.1.4 Implementation of the SVD Filter

Under the hypothesis of high spatiotemporal coherence for the tissue signal, a new spatiotemporal representation of the Ultrafast acquisition in the basis provided by the singular value decomposition is built. The first step is presented in Fig. 4.3(a) and consists in rearranging the Ultrafast Doppler acquisition into a 2D Casorati matrix S where one dimension is space and the other dimension is time. Singular value decomposition could be performed on this matrix S and directly give the new temporal singular vector basis U and the new spatial singular vector basis V.

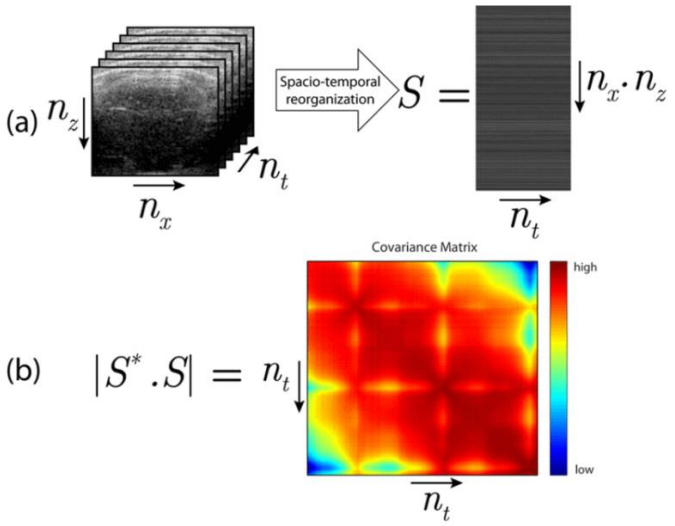

Figure 4.3: (a) The ultrafast doppler acquisition forms a 3d stack of images with 2 spatial dimensions and one temporal dimension. It is reshaped in one spatiotemporal representation (casorati matrix) where all pixels at one time point are arranged in one column. (b) The covariance matrix is presented in magnitude and is of dimension nt×nt.

The Ultrafast Doppler acquisition presents many more spatial points than temporal points (several hundreds or thousands), and it is demanding from a computing point of view to form the nt×nt covariance matrix (Fig. 4.3(b)) and diagonalize it. This gives nt temporal eigenvectors that are the right singular vector Vi of S.

Fig. 4.4(a) shows the spectral content of the eigenvectors sorted by decreasing eigenvalue. The largest eigenvalues are associated with the temporal singular vectors presenting the slowest variation. This is consistent with spatially coherent tissue signal supposed to be quite similar in neighboring pixels in a way that enables to reduce the nx×nz realizations of tissue temporal signal on a much smaller subspace. Therefore, tissue signal is supposed to be concentrated in the first singular vectors whereas blood and noise signals are described by the singular vectors associated with lower singular values. The eigenvalue itself is closely related to the energy associated the corresponding singular vector

and Fig.4.4(b) depicts the relative variation of those singular values: the dashed red line shows that with a threshold of 50 rejected singular values the SVD clutter rejection discriminates the supposedly tissue from a signal 30 dB below, which is really consistent with the expected relative difference between tissue energy and blood energy at that range of US frequencies (15 MHz).

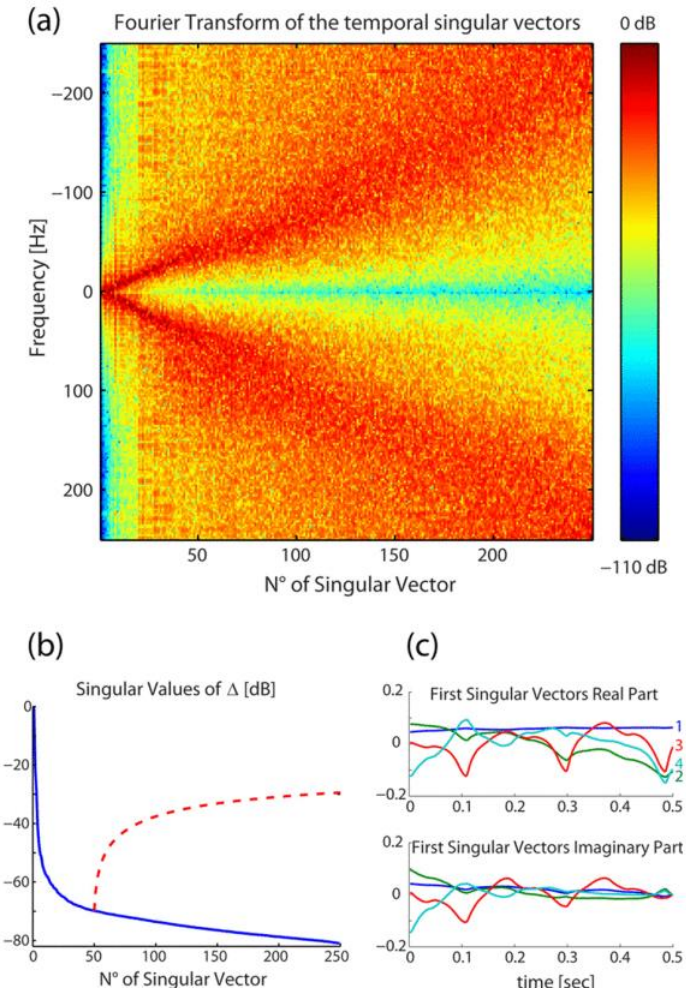

Figure 4.4: (a) Spectral content estimation of all the right singular vectors, sorted with decreasing singular value. Low frequency temporal signal is associated with the highest singular values. As all singular vectors are normalized, energy in all spectra is equal to one. (b) Singular values of the matrix Δ (solid blue) expressed in dB and cumulative sum of those singular values from n∘50 (dashed red). (c) The first four singular vectors of the covariance matrix are plotted versus time.

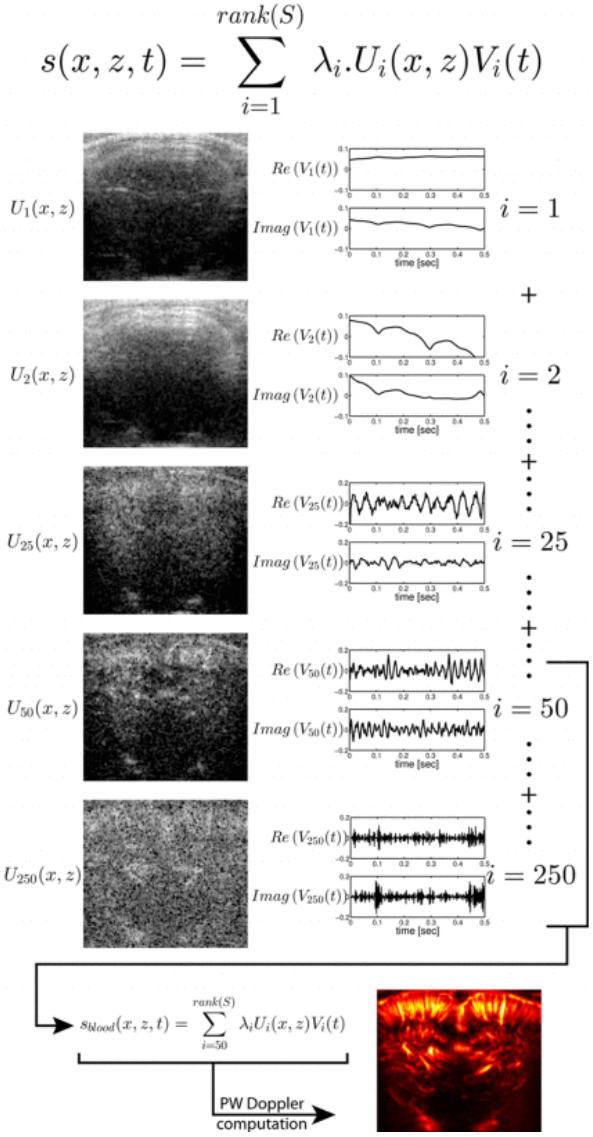

Figure 4.5: The ultrafast acquisition (same data than Fig. 4.4) is decomposed by the singular value decomposition into a set of spatiotemporal couples of vectors. Tissue signal is coherent enough to be quite similar over the entire image, and that it is described by a set of vectors constituting a subspace of the temporal signal space, but much smaller. Indeed, by rejecting the first 49 couples of singular vectors, tissue signal is rejected and a very good PW doppler image of the vascularisation in the rat brain is obtained.

Using this decomposition, s(x, z,t) can be decomposed on both a temporal basis and a spatial basis of singular vectors Fig. 4.5. Based on the assumption that tissue signal is gathered in the first singular vectors, clutter rejection is performed using a threshold n on the number of singular vectors removed from the raw signal:

$$s_{blood(x,z,t)} = s(x,z,t) - \sum_{i=1}^{n} x_i I_i(x,z) Vi(t)) \tag{4.7}$$

This filtered signal is processed using short time Fourier transform for blood flow speed measurement or the energy per pixel can be computed to produce the Power Doppler image.

$$PW(x,z) = \int |s_{blood(x,z,t)|2 \quad dt} \tag{4.8}$$

4.2 Singular Value Thresholding for Ultrasound Clutter Removal

The singular value thresholding clutter removal seeks a low rank approximation of R (Casorati Matrix) which can best represent and remove the tissue contribution. The best rank *K* approximation of the matrix R can be found via SVT as:

$$R\_clutter = argmin\ (rank(z) < K)\ \big||R - Z|\big|F = \sum_{i=1}^{k} \sigma_i U_i V_i^h \tag{4.9}$$

where $R = U\Sigma V^H$ is the singular value decomposition (SVD) of *R*, $U = [u_1, u_2, \ldots, u_S]$ and $V = [v_1, v_2, \ldots, v_S]$ are unitary matrices, $\Sigma = diag(\sigma_1, \sigma_2, \cdots, \sigma_r)$ is a diagonal matrix of singular values, *S* is the rank of *R* and $\|.\|_F$ indicates the Ferobinous norm. Hence the combined blood and noise sub-space can be represented as:

$$R_{blood+noise} = \sum_{i=K+1}^{S} \sigma_i U_i V_i^h \tag{4.10}$$

In ideal situations where all attenuations are compensated by TGC and tissue clutter signal is perfectly removed by SVT, the blood and noise signal at depth z_i of a scanline can be approximated as:

$$R_{blood+noise}(zi, tk) \approx s_b(zi, tk) + G_{atgc}(zi)G_{dtgc}(zi)\ \text{n(zi, tk)}) \tag{4.11}$$

Equation 5.10 represents the estimated blood signal which is also contaminated by depth dependent (due to TGC) additive noise. Using this data, the corresponding power Doppler intensity can be formed as:

$$pw_{blood+noise}(zi) = \frac{1}{k}\sum_{k}^{K} |s_b(zi, tk) + G_{atgc}(zi)G_{dtgc}(zi)\ n(zi, tk)|)2 \tag{4.12}$$

$$\cong \frac{1}{k}\sum_{k}^{K} |s_b(zi, tk)|2 + |G_{atgc}(zi)G_{dtgc}(zi)|2\ PWnoise$$

where the last equation follows from the assumption that blood and noise signals are independent ergodic random processes such that

$$pw_{noise} = \frac{1}{k}\sum_{k=2}^{k}|n(tk)|^2 \tag{4.13}$$

and noise is modelled as independent identically distributed (i.i.d) for all points through the depth. As it can be seen in eq. 5.12, the SVT-filtered power Doppler images of the vessels are expected to be superimposed on a background signal formed by noise. If TGC is employed, the background signals present spatial variability which stems for the depth dependent amplifications of the noise as predicted by 5.12.

4.3 Background Removal Using Top-Hat Filtering

A morphological-based filtering, Top-hat filtering, is used to estimate and remove the background signal from the SVT-derived power Doppler images using nonlinear operations.

A top-hat filtering (THF) is comprised of a background estimation followed by a subtraction operation. For an image, *I*, the white top-hat filtering is defined as:

$$Iw=I-I\circ SE \tag{4.14}$$

where SE is a morphological structuring element and ∘ is an opening operation. The opening of image *I* by a structuring element *b* is defined as:

$$I \circ b = (I \ominus b) \oplus b \tag{4.15}$$

where $\ominus$ and $\oplus$ are the erosion and dilation operations respectively. The gray-scale dilation and erosion are the two basic mathematical morphological operations which at pixel (*x, y*) are defined as:

$$\{[I \ominus b]_{(x,y)} = \min_{(s,t)\in b}\{I(x+s,y+t)\} \text{ Erosion} \tag{4.16}$$

$$\{[I \oplus b]_{(x,y)} = \max_{(s,t)\in b}\{I(x-s,y-t)\} \text{ Dilation} \tag{4.17}$$

$I(x + s, y + t)$ and $I(x - s, y - t)$ are simple translational shifts of the image *I* performed for all pairs (*s, t*) selected from the structuring element *b*. Hence, the white top-hat filtering of image *x* by structuring element SE is:

$$Iw = I - (I \ominus SE) \oplus SE \tag{4.18}$$

4.4 Hessian-Based Vessel Enhancement Filtering

Morphological filtering can enhance the visibility of the vascular structures in presence of the strong background signals. However, the randomness of the background noise creates image features with morphological structures smaller than the size of the structuring elements. Hence, in addition to vessel-like structures these random patterns will be also present at the output of the top-hat filtering. To further promote vascular structures and penalize the residual random background a vessel enhancement filtering is required.

In power Doppler images, the second derivative of intensity near the vessels is expected to be large in the direction perpendicular to the vessel orientation and very small along the vessels. Hence, this characteristic can be employed to devise filters which can significantly promote the vessel-like structures and penalize unstructured random shapes. The Hessian matrix of an image can provide

information about the second derivative. However, in order to capture curvature features independent of the vessel direction, the eigenvalues along the two eigenvectors of the Hessian matrix can be used instead. Additionally, to make the analysis of the curvature less sensitive to scaling, intensity variations and limit noise amplification, direct derivatives can be replaced by the scale space Gaussian derivatives. Using this approach, the intensity signal, *I*, within δr distance from a pixel located at *r* can be written as:

$$(I(r+\delta_r, s) \cong I(r) + \delta r^{\mathrm{T}} \nabla_{\mathrm{S}} + \delta r^{\mathrm{T}} \mathrm{H}_{\mathrm{S}}\, \delta r^{\mathrm{T}} \tag{4.19}$$

where ∇_s and Hs are the Gaussian gradient vector and the Hessian matrix at size scale s respectively. In the scale space theory, true derivatives are replaced by the scaled bandlimited differentiation using a Gaussian kernel as:

$$\frac{\partial}{\partial r} I_{[(r,s)} = \frac{\partial}{\partial r}(I(r) * \Gamma(r,s) = I(r) * \frac{\partial}{\partial r}\Gamma(r,s) \tag{4.20}$$

where $\Gamma(r, s)$ is a Gaussian kernel defined as:

$$\Gamma(r,s) = \frac{1}{2\pi s}{}_2\, e^{-\frac{||r||2}{2s}2} \tag{4.21}$$

Based on this definition of the differentiation, the Hessian matrix at scale *s* in the Cartesian coordinate is calculated.

Eigenvalue decomposition of Hs provides curvature information along two principal directions represented by their corresponding eigenvectors and eigenvalues. Since vessel orientation is not of any interest, the eigenvalues, λ_1 and λ_2 (assuming $|\lambda_2| > |\lambda_1|$) are only considered for further vessel analysis. In the vicinity of any intensity increase both eigenvalues become negative numbers. Noise-like variations, however, do not result in significant eigenvalues. Therefore, the energy of the eigenvalues can be used as a measure for assessment of the structured shapes as opposed to random patterns. The Hessian eigenvalues can be computed for a number of size scales which are defined based on different vessels sizes present in the imaged region. Based on the eigenvalues at each size scale, Frangi *et al.* proposed a vessel enhancement and thresholding function as the following:

$$\Delta s = \begin{cases} 0 & ,\lambda_2 > 0 \\ e^{-\frac{M}{2\beta^2}}\left(1 - e^{-\frac{\Delta^2}{2\alpha^2}}\right) & ,elsewhere \end{cases} \quad (4.22)$$

The output of (4.23) is an intensity image which is maximum at vessels with size *s*. $M = \frac{\lambda_1}{\lambda_2}$ defines the eccentricity of the second order ellipse defined by the eigenvectors and $\Delta = \sqrt{\lambda_1^2 + \lambda_2^2}$ is used to penalize any unstructured patterns such as background noise. Parameter α defines the roll-off rate for soft-thresholding of the unstructured patterns; a large α penalizes the noise-like areas more aggressively but may result in damages to the vascular structures. A small α may allow more noise in the final image limiting the utility of the vessel filter. Parameter β controls the dynamic range of the output intensity such that large values of β decrease the final image intensity at a vessel area and vice versa. An important aspect of using the scale space analysis is the fact that the structures can be analyzed at different size scales simultaneously. In other word, the output of the vessel function, Δ_s, is only sensitive to the shape similarities instead of image intensities. Hence the final power Doppler vessel image, Δ, can be formed by taking the maximum value of δ_s over all estimated size scale values *s*.

$$\Delta = \max_s \Delta s \quad (4.23)$$

4.5 Vessel Segmentation and Skeletonization

The microvasculature image (output of Hessian filter) is converted in to a binary image, the small noise-like objects are removed through an erosion and dilation operation; the small holes are removed and then filled with a dilation and erosion operation; the image skeleton is found and then cleaned; removed the spur pixels; labeled connected components;found the branch points; dilated the branch points; removed the branch points and removed the small objects. After these steps, the output image includes the vessel segments. Those segments are analyzed in the vessel quantification module to estimate the desired quantitative parameters of the vessels. The following preprocessing steps are:

I. *Converting grayscale to binary:* The input image to the morphological operation module, IH(x,z) , is converted to a binary image IB(x,z).

II. *Erosion followed by dilation:* Erosion followed by dilation is used to remove some noise-like small objects in the image after amplitude thresholding.

III. *Removing small holes:* A morphological "hole-filling' step is added to avoid erroneous splitting of the vessels; this step sets a pixel to 1 if five or more pixels in its 3-by-3 neighborhood are 1s; otherwise, it sets the pixel to 0. After this operation, some small holes with larger sizes remain.

IV. *Finding the skeleton image:* To estimate the centerline of vessel structure, the next step in the morphological operations on binary images is removing pixels so that an object without holes shrinks to a line, and an object with holes shrinks to a connected ring halfway between each hole and the outer boundary. Finding the skeleton image is based on a thinning algorithm.

4.6 Vessel Quantification

The quantification parameters include number of vessel segments, vessel density, number of branch points, vessel diameter, and vessel tortuosity. Two different tortuosity metrics are considered: the distance metric (DM) and the sum of the angle metric (SOAM). Each vessel is defined by a "location vector" whose elements represent the pixels within the vessel. The location vector for the vessel j is defined as Pj:=[p1j,….,pNjj] $P_j = [P_{1j},\ldots..,P_{Nj}]$ where $P_{i,j} = [X_{ij}, \ldots\ldots, Z_{ij}]^{\mathrm{T}}$ is the point i in the vessel j , and Nj is the length of vessel j.

I. Distance Metric' (DM)

The DM of the vessel j is the most common parameter used to measure vascular tortuosity in 2-D. The DM of a vessel is defined as the ratio between the actual path length of a meandering curve and the linear distance between endpoints. The DM for vessel j is denoted by τ in the following equation:

$$\tau_j = \sum_{k=2}^{N} |P_{K,J} - P_{K-1,J}\,| / P_{N,J} - P_{1,J}) \qquad (4.24)$$

II. Sum of Angle Metric (SOAM)

The displacement vectors between points $P_{K-1,J} - P_{K,J}$ on vessel j are defined by:

$$d_{K,J} = P_{K,J} - P_{K-1,J} \tag{4.25}$$

where k $\in\{2,\ldots, N_{J-2}\}$, and Nj is the length of the vessel in pixels. The in-plane angle at the point $P_{K,J}$ is given by:

$$I_{kj} = \cos^{-}1\left(\left(\frac{d_{k,j}}{|d_{k,j}|}\right).\left(\frac{d_{k+1,j}}{|d_{k+1,j}|}\right)\right) \tag{4.26}$$

The total angle at point pkj and vessel j is given by:

$$CP_{k,j} = |I_{k,j}| \tag{4.27}$$

The SOAM calculates the total tortuosity of the vessel j and is defined as in.

$$SOAM_j = \sum_{K=2}^{NJ-2} CP_{k,j} \,/\, \sum_{K=2}^{N} |P_{k,j} - P_{k-1,j|} \tag{4.28}$$

III. Estimating Diameter

To obtain the vessel diameter, the Euclidean distance in the inverted image between pixels corresponding to vessel segments and the nearest pixel corresponding to the background of the image has been calculated. For all pixels corresponding to vessels, the distance to the most adjacent non-vessel pixel is dedicated to that pixel. The set of points inside of the vessel region and the background region is denoted by V and B, respectively. For any point of (x,z)∈V , the Euclidian distance between (x,z) and all points (xb,zb)∈B are calculated, and the minimum distance value is obtained as follows:

$$d(x,z) = \min_{[x_b,z_b)} \sqrt{(x-x_b)^2 + (z-z_b)^2} \tag{4.29}$$

The vessel image is then skeletonized using a thinning algorithm so that the distances along the centerlines can be calculated. The i^{th} point at centerline of the vessel j is denoted by (x_{ij},z_{ij}). Vessel diameter is $D(x_{ij},z_{ij})=2d(x_{ij},z_{ij})$. For each vessel segment, the average diameter of the vessel segment over points related to that vessel is reported as vessel segment diameter D_j.

IV. Microvessel Fractal Dimension (mvFD):

Microvessel fractal dimension is a metric used to quantify the structural complexity of a vascular network. The box counting method was employed to calculate mvFD using the binary image through the following six steps also displayed in the Figure 4.6: 1) the binary image was padded with zeros to make its dimensions to a power of 2; 2) the box size (S) was set to the size of the binary image; 3) the number of boxes (NS) needed to cover all vessels (non-zero pixels) in the binary image were counted; 4) S was set to S/2 and step 3 was repeated only if S>sizeofapixel , otherwise, the process continues to step 5; 5) a first-order polynomial fit was applied to the pairs, (log(1S),log(NS)) ; 6) the slope of the fitted line was obtained as mvFD:

$$mvFD = \lim_{S\to 0} \frac{\log Ns}{\log 1/s} \tag{4.30}$$

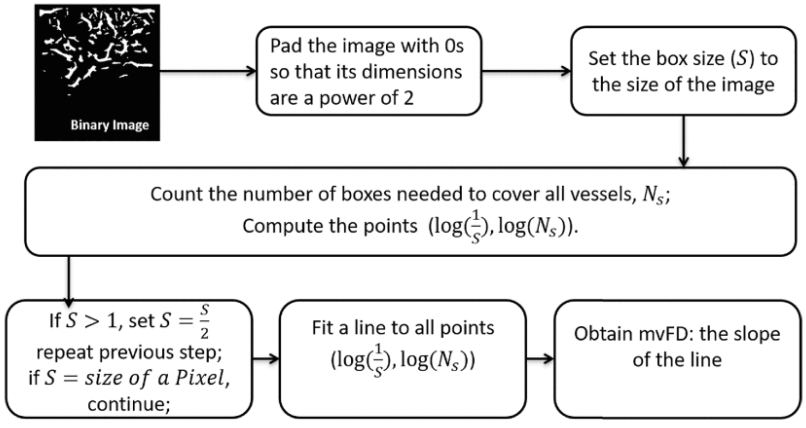

Figure 4.6: Diagram of microvessel fractal dimension calculation.

V. Murray's Deviation (MD):

To quantify vessel morphological parameters, binary and skeleton images were formed. The vessels are sequentially thinned, and the midline of each vessel determined to construct the skeleton of a vessel network. Using skeleton image, the 3-by-3 neighborhood pixels were removed for each branch point to isolate and label each vessel component. This allowed to determine the number of branches. A unique label was assigned to each segment. Diameters (D) of vessels were calculated using the binary image. For each branch point, a 4×4 -pixel neighboring region was defined on the skeleton image. The number of non-zero pixels was obtained as the number of sub-vessels (NSV). According to their labels, the diameters of sub-vessels were found from diameter data and then used to define mother and daughter vessels; the sub-vessel with the largest diameter was designated as a mother vessel and the remaining sub-vessels served as daughter vessel(s). MD was calculated using 4.31. A flowchart of the MD calculation is shown in Fig. 4.7.

$$MD = \frac{D_{mother}^3 - \sum D_{doughter}^3}{D_{mother}^3} \tag{4.31}$$

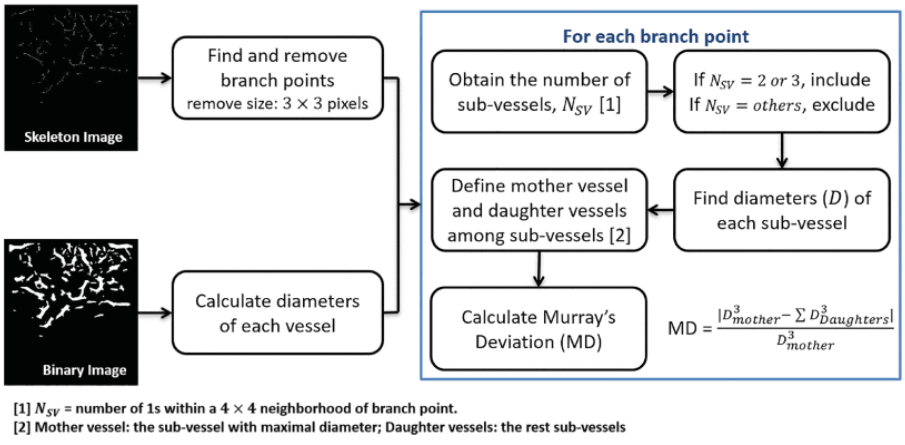

Figure 4.7: Diagram of Murray's deviation calculation

VI. Bifurcation Angle (BA):

At first N_{SV} was defined for each branch, and only the branch with three sub-vessels, one mother vessel and two daughter vessels, was included, as the BA refers to the angle between two daughter vessels. The average vessel length of each data set was calculated after branch point removal. The two daughter vessels were selected the same way as was done for MD. Two straight lines were generated by fitting two daughter vessels, and the angle between them was calculated as BA. Only the near-branch-point part of the daughter vessels was used for fitting, based on their length (LD, unit pixels): if $L_D \leq 3$ pixels, whole daughter vessels were used; if $3 < L_D \leq VL$ pixels, half daughter vessels were used; if $L_D > VL$ pixels, 1/5 daughter vessels were used (Fig. 4.8).

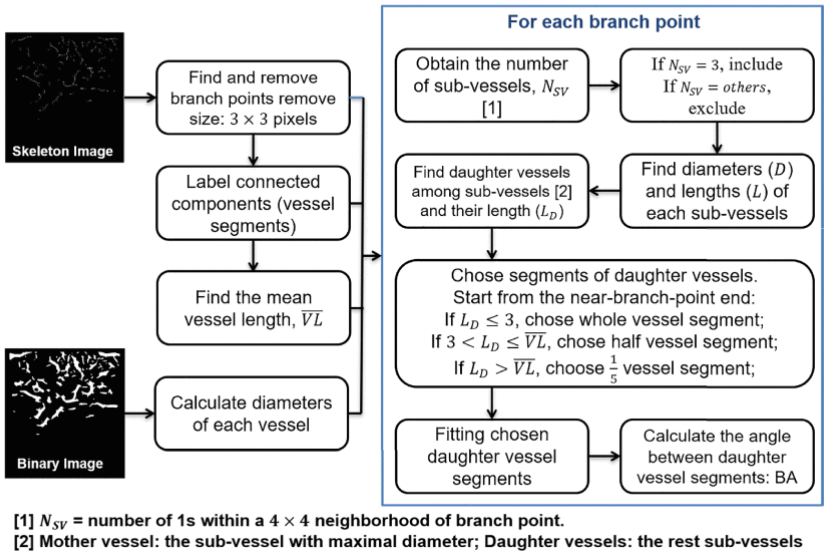

Figure 4.8: Diagram of bifurcation angle calculation

VII. Spatial Vascularity Pattern (SVP):

The spatial vascularity pattern assesses the tumor vascular distribution pattern as being either intratumoral, which is more concentrated inside, or being peritumoral, which is more concentrated peripherally, shown with two possible values (SVP = 1) and (SVP = 0), respectivelyIn the present study, to calculate the SVP, image erosion has been performed to mask the image, then the geometric center of the lesion was defined, and the largest radius was selected on the mask image. Next, after defining the center and peripheral regions of the lesion, the vessel density ratio (VDR) was calculated. A flowchart of the SVP calculation is shown in Fig. 4.9.

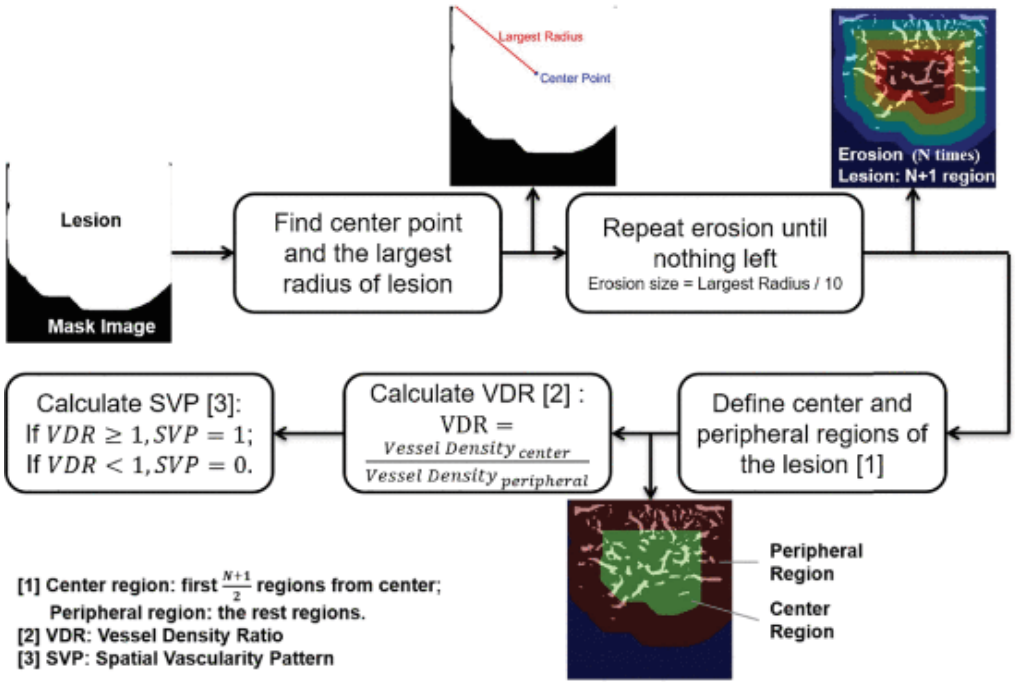

Figure 4.9: Diagram of spatial vascularity pattern calculation

VDR has been defined as the ratio of vessel density of the tumor center to periphery. Therefore, VDR can describe the tumor vessel distributions at the periphery (VDR < 1), or at the center (VDR >1) or both (VDR ≈ 1). VDR was calculated as:

$$VDR = \frac{Vessel\ density\ center}{Vessel\ density\ peripheral} \tag{4.32}$$

Finally, after calculating VDR, we have defined SVP as:

$$\begin{cases} VDR \geq 1, \ SVP = 1 \\ VDR \leq 1, \ SVP = 0 \end{cases} \tag{4.33}$$

A VDR equal to or larger than 1 defines the SVP value as equal to 1, meaning the vascular distributions are more concentrated centrally and a VDR less than 1 defines the SVP value as zero, meaning the vascular distributions are more concentrated peripherally.

5.Matherials and Methods

5.1 Patient Study

This study was performed in compliance with the Health Insurance Portability and Accountability Act (HIPPA) and under the guidelines and regulations of an approved institutional review board (IRB) protocol. A written IRB approved informed consent with permission for publication was obtained from each patient participant prior to the imaging study. Our study population comprises patient participants, 18 and up, with suspicious nodule, who were prospectively enrolled for this study from March 2015 to May 2017. From a total of 92 patients studied, there were 74 female and 18 males, ages from 18 to 86 years and mean age 59.50 ± 0.71.

All study patients underwent ultrasound examination, and the morphological features of thyroid nodules were evaluated for Thyroid Imaging Reporting and Data System (TI-RADS). TI-RADS scores and the histopathological results of FNAB and or surgical excision were included in the analysis. TI-RADS scores above 3 were referred for fine needle aspiration biopsy (FNAB) and or surgical as their clinical care of thyroid nodule as part of their clinical care. Subsequently, our study patients underwent ultrasound examination as their clinical care and the morphological features were measured. All study patients underway FNAB within an hour or a day after the HDMI test. Under ultrasound guidance, our board-certified endocrinologists or radiologists performed FNAB, using standard sterile technique, and a 25-gauge needle to obtain six fine needle aspirates for each node. Immediately after FNAB, slides were prepared and sent for cytology. Pathological diagnosis was made by pathologists with more than 15 to 20 years of experience. The histopathological results of FNAB and surgical excision for all thyroid nodules were included for data analysis as reference gold standard.The diagnosis of all benign nodules, except two, was made by FNAB. The diagnosis of all malignant nodules, as well as the two benign that were indeterminate in their primary FNAB, was confirmed by surgical pathology.

5.2 High-definition Microvasculature Imaging and Quantitative Biomarkers

For all participant HDMI was conducted before FNAB and or Surgery. Ultrasound examination was conducted by two sonographers with more than 30 and 18 years of experience, respectively. However, only one of the two sonographers participated in each participant study. Thyroid nodules were identified using an ultrasound platform equipped with plain wave imaging, Alpinion ECube 12-R ultrasound scanner (Alpinion Medical System Co., Seoul, South Korea), equipped with a L3-12H linear probe operating at 8.5MHz, Figure 5.1.

Then a sequence of high frame rate data (at ~ 600 frames per second) was acquired on the lesion site. This ultrasound system provides a sequence of frames in the form of raw in-phase and quadrature beamformed data for a total duration of 3 s. Each frame of the data was formed using 5-angle coherent plane-wave compounding.

.

Figure 5.1: Alpinion ECube 12-R ultrasound scanner

To reduce the compression effect on altering tissue microvessel, the sonographers were instructed to reduce the preload during ultrasound examination. To diminish motion artifacts, patients were requested to remain stand still and pause their breath for around 3 seconds during data acquisition.

Patient were scanned in the supine position with their neck inclined back and turned to the left or right, depending on the position of the nodule. After finding the nodule in B-mode ultrasound, a sequence of high frame rate data has been processed, detailed in chapter 5 (and article (22)). The acquisitions were acquired in both longitudinal and transversal cross-section of the thyroid gland, two acquisitions in each orientation.

Motion incurred by thyroid due to its proximity to the pulsating carotid artery impacts the visualization of blood fow in small vessels. Singular value based spatiotemporal clutter fltering (SVD-STF) improves the performance of tissue rejection in the presence of motion. However, despite efective clutter fltering, motion in thyroid imaging can impact coherent integration of the Doppler ensemble and degrade the visualization of the underlying vasculature.

Since, out-of-plane motion less occurs in longitudinal cross section, due to distal location of trachea and carotid artery with respect to the thyroid gland, figure 5.2, the longitudinal view was selected as a more reliable cross-section for microvascular blood flow images (34).

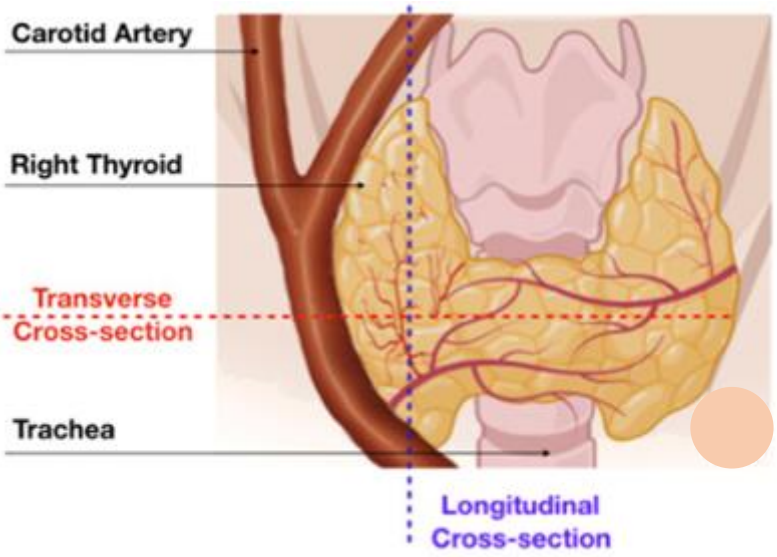

Figure 5.2: Display of the anatomical position of the thyroid gland, the pulsating carotid artery, and the rigid trachea, with respect to the longitudinal and transverse planes

After HDMI acquisitions, image processing, denoising have been done as reported in chapter 5. The nodules were manually segmented using B-mode images obtained from the IQ data reconstruction, and images were prepared for quantification of morphological parameters of tumor microvessels [30]. Subsequently, microvessel morphological parameters including, number of vessel segments (*NV*), vessel density (*VD*), number of branch points (*NB*), vessel diameter (*D*), vessel tortuosity (τ) determined by distance metric (*DM*), bifurcation angle (*BA*), Murray's deviation (*MD*) and spatial vascular pattern (*SVP*) calculated by vessel density ratio (*VDR*), were extracted from the HDMI images. All the methods for HDMI image formation, vessel extraction, steps for vessel segmentation and quantification have been detailed in chapter 5.

5.3 Statistical analysis method

The diagnostic performance of each parameter for differentiation of benign and malignant thyroid nodules was determined using the Wilcoxon rank-sum test, the receiver operating characteristic curve (ROC) and the 95% confidence interval, implemented on MATLAB software. To investigate the specificity, sensitivity, and the area under the curve (AUC) the receiver operating characteristics curve (ROC) analysis has been performed using Machine Learning,Classification Learner, MATLAB toolbox. This was achieved by partitioning the input data set and using a subset (70%) to train the algorithm and the remaining data (30%) for testing. The multivariable analysis using a support vector machine (SVM) classification method trained in the space of HDMI biomarkers alone and both HDMI biomarkers and clinical factors (age, size and TI-RADS) has been used to develop two different models, HDMI model and HDMI-C. To prevent overfitting and evaluate the model's accuracy, a five-fold Cross-Validation procedure was used. A p-value < 0.05 was considered to be significant in discriminating thyroid nodules.

6.Results

6.1 Histopathological Results

In total of 92 patients examined by HDMI, the histopathological results of FNAB confirmed 55 (60%) of thyroid nodules as benign and 2 (2%) nodules were confirmed by surgical pathology and 35 (38%) as malignant confirmed by surgical pathology. From the entire cohort 74 (80%) patients were female and 18 (20%) males, with age range 18 to 86 years (mean age 59.50 ± 0.71 years) and the lesion size in the largest dimension ranged from 6 to 60 mm with a mean of 17.50 ± 6.37. The participant demographic information, lesion characteristics, the distribution of malignant lesion type by the pathology and the TI-RADS score for each are reported in Table 6.1. The most common malignant histologic type was papillary thyroid carcinoma, 28 (80%) nodules.

The point total determines the nodule's TI-RADS level, which ranges from TR1 (low suspicion for malignancy) to TR5 (high suspicion of malignancy). Although it is possible for a nodule to be awarded zero points and hence be characterized as TR1, all nodules merit at least two points because a nodule that has a mixed cystic and solid composition (one point) will also gain at least one more point for the echogenicity of its solid component. The decision to perform FNA should also account for the referring physician's preference and the patient's risk factors for thyroid cancer, anxiety, comorbidities, life expectancy, and other relevant considerations.

Most of the thyroid nodules in this study were classified as TI-RADS scores 4 and 5.

The dataset comprises a larger number of patients, but some were escluded from the study because of the FNA results; suspiscious for malignancy, indeterminate, and non diagnostic nodules weren't included in the analysis.

Table 6.1: Participant demographic characteristics and malignant nodule types

Patients n=92	Benign n=57 (62%)	Malignant n=35 (38%)
Gender		
Female[a]	47	27
Male[a]	10	8
Age (y)	45.5±19.09	41±3.53
Nodule size (mm)	16±8.48	22.5±14.85
TI-RADS scores		
2	2	1
3	8	0
4	27	9
5	16	24
Malignant nodules		35 (38%)
Papillary carcinoma		28
Medullary carcinoma		3
Papillary microcarcinoma		1
Metastatic papillary carcinoma		3
Anaplastic carcinoma		1

6.2 Visualization of Microvessels of Thyroid Nodules

Figure 6.1 demostrates the sequence of processing steps of the microvasculature image formation, morphological operations, and vessel quantifications algorithm, an example of the output image in each processing step are reported below.

These steps are shown by taking in consideration one patient with benign thyroid nodule, TVACU 173.

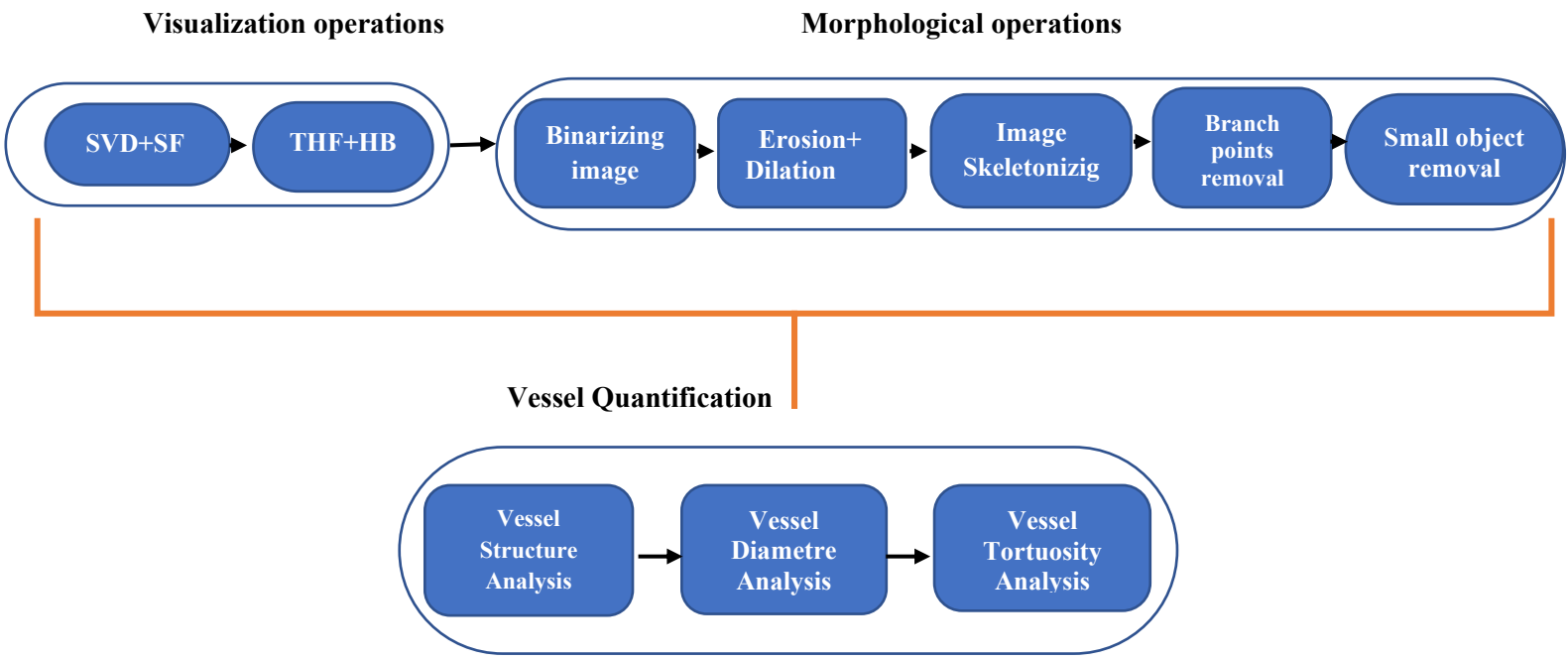

Figure 6.1: Block diagram of the microvasculature analysis system, including visualization and morphological operations and vessel quantification. SVD, singular value decomposition, SF, spectral filtering, THF, top hat filtering, HBF, hessian-based filtering.

Visualization operation

Processing begins with the storage of ultrasound plane-wave data in the quadrature (IQ) format Fig. 6.2(a). The lesions from the thyroid nodules were manually segmented using the B-mode images obtained from the first frame in the imaging sequence and selecting the Region of Interest (ROI) Fig. 6.2(b).

In oreder to reject clutter signals from the Ultrafast Doppler, Singular Value Decomposition (SVD) was employed Fig.6.1(d), then the optimal clutter rank, wich can best reppresent and remove tissue contribution and coincides with a point at which significant singular value decay rate change occours, was determined Fig.6.2 (c).

The Top-Hat filtering was used to remove the backround noise and to enhance the visibility of the microvasculature image in the presence of strong background signal Fig6.2 (e). Due to background noise random pattern are still present in the output of the THF, hence vessel enhancment Hessian enhancment filter is used to penalize background noise and further enhance vessel structure Fig.6.2(f).

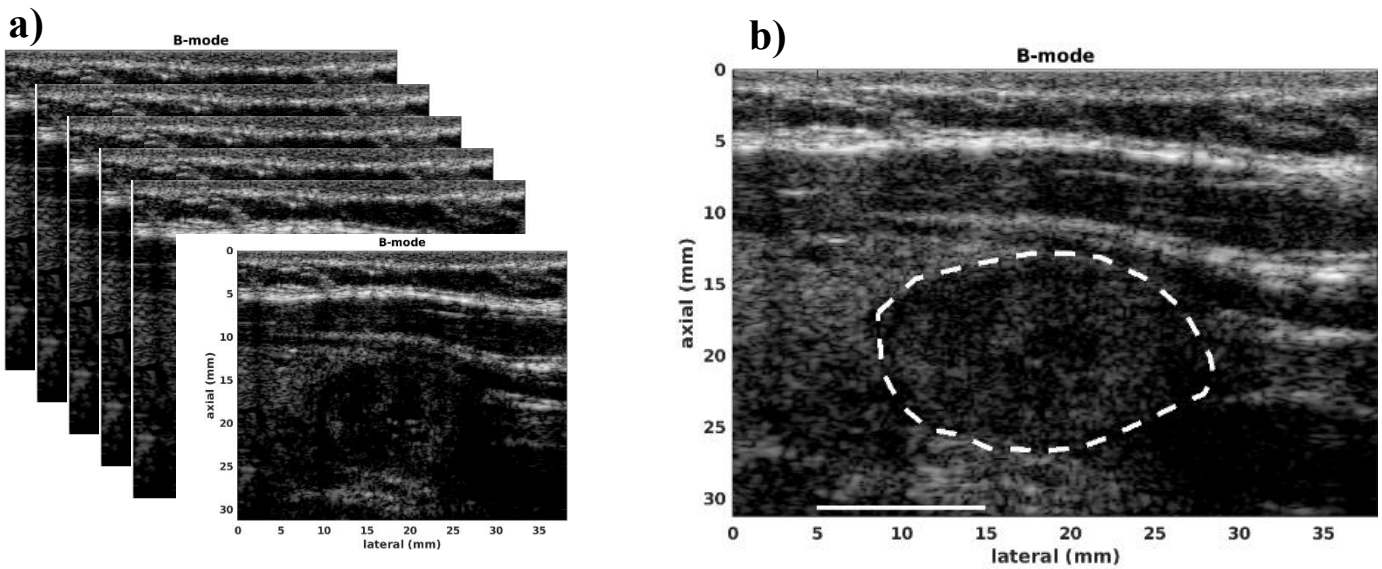

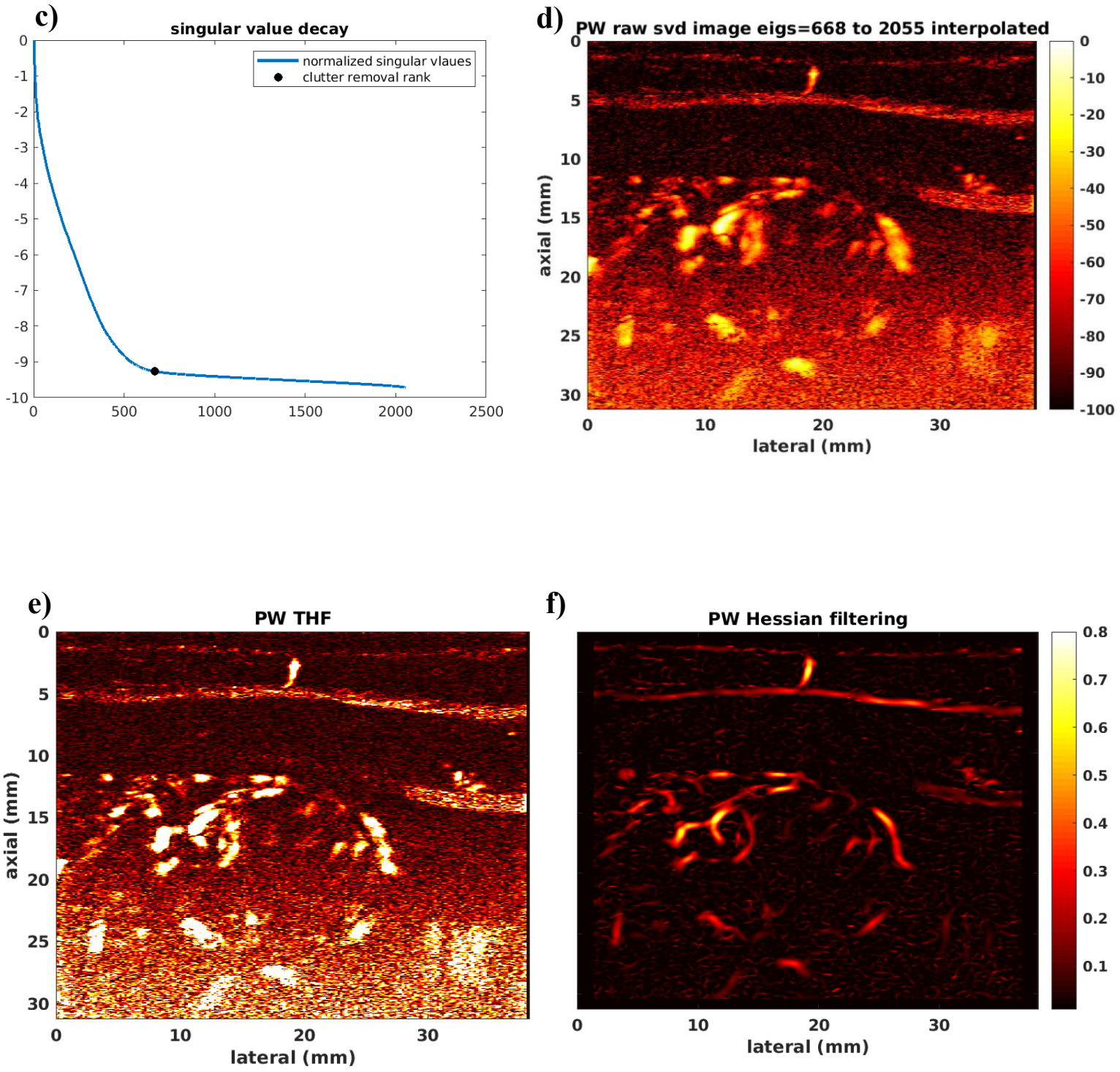

Figure 6.2: Output image of each of the Visulization operation procesing steps: (a) IQ data format, (b) ROI segmentation, (c) Clutter removal rank, (d) SVD, (e) Top hat filtering, and (d) Hessian-based filtering

Morphological operations

The microvasculature image (output of Hessian filter) is converted to a binary image, then the image skeleton and branch points has been found, Fig.6.3. After these steps, the output image includes the vessel segments. Those segments are analyzed in the vessel quantification module to estimate the desired quantitative parameters of the vessels.

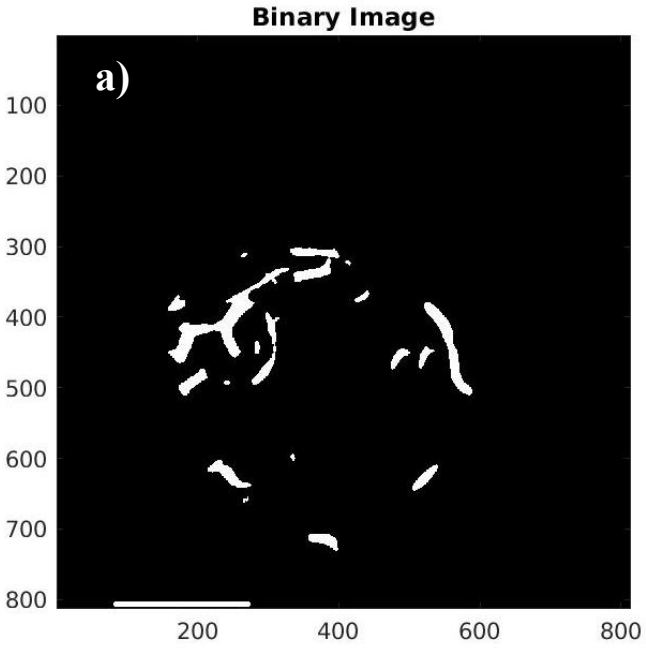

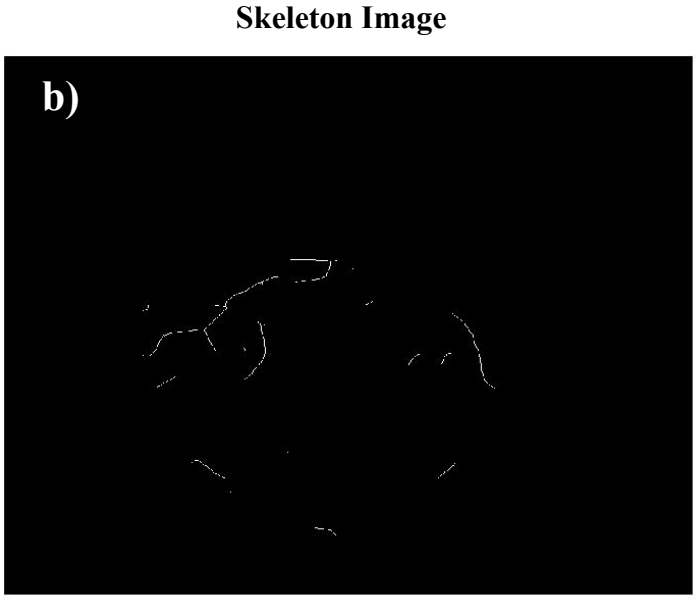

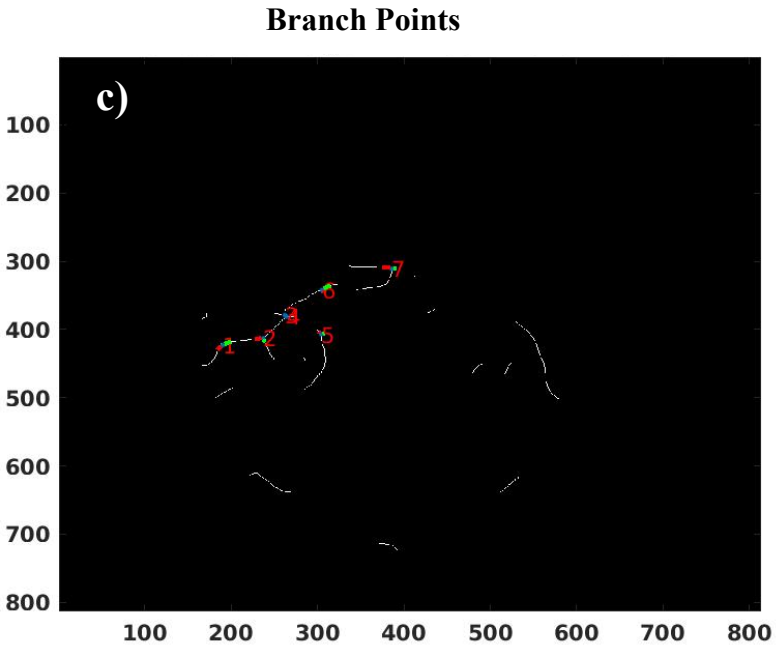

Figure 6.3. (a) Binary image, (b) Skeleton image and (c) Bifurcatio Angle

Vessel quantification

The processing steps of the vessel quantification comprise; vessel structure analysis (number of branch points, number of vessel segments); vessel diametre analysis; vessel tortuosity analysis.
Based on these results, the quantitative parameters of vessels (diametre, number of vessel segments, number of branch points, DM, SOAM, Bifurcation angle, Murray's Deviation and Spatial vascular pattern (SVP)) has been estimated. Figure 6.4 displys the diametre image and SVP respectivey.
As can be seen in Fig.6.4 (b) VDR less than 1 defines the SVP value as zero, meaning the vascular distributions are more concentrated peripherally.

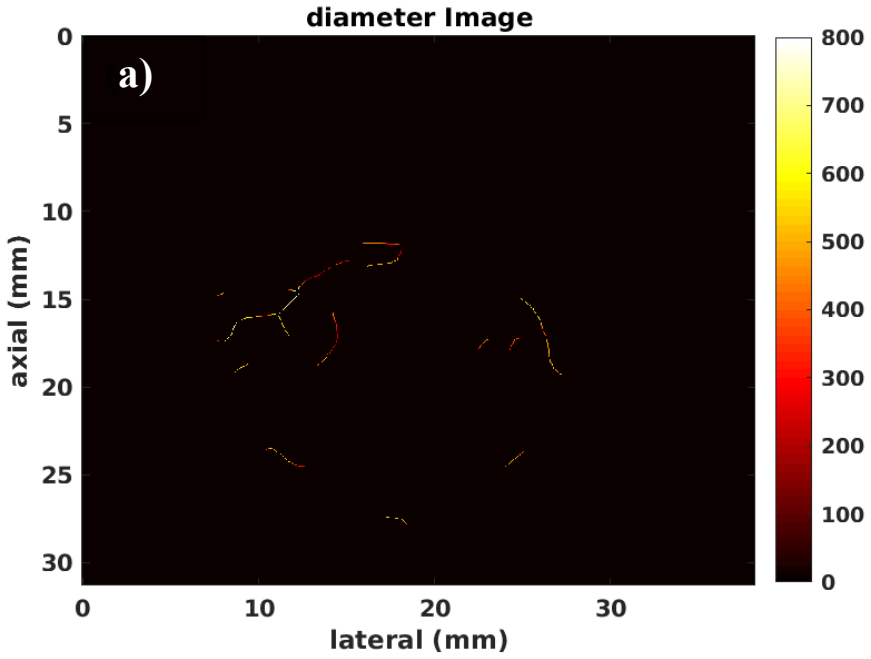

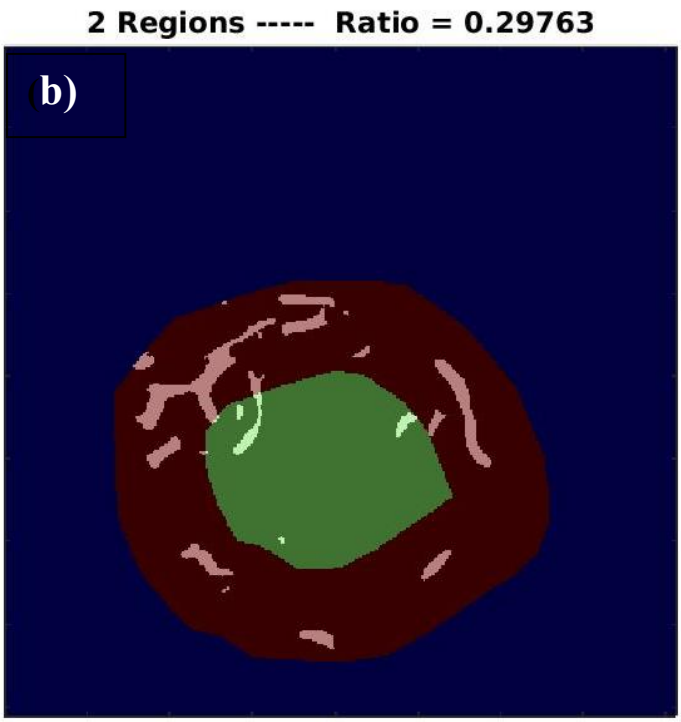

Figure 6.4: (a) Binary image, (b) Spatial vscular Pattern

6.3 Quantification of Microvessel Biomarkers

Representative images of benign and malignant thyroid nodules in two groups of patients, based on nodule size and spatial vascularity pattern along with quantified biomarkers are displayed in Figures 6.5 and 6.6. Conventional B-mode ultrasound and HMDI images of larger and smaller nodules, with a diameter in largest dimension, 24 mm in benign nodule, Figure 6.5 (a, b) and 23 mm in malignant nodule, Figure 6.5 (e, f), respectively. In Figure 6.6, B-mode ultrasound, and HDMI images of smaller nodules with a diameter in largest dimension, 12 mm in benign nodule, Figure 6.6 (a, b) and 11 mm in malignant nodule, Figure 6.6 (e, f). The SVP diagram displays the vascular distribution pattern as perinodular in Figure 6.5(d) and intra nodular in nodules displayed in Figure 6.5(h) and Figure 6.6(d, h) nodules. The visual inspection shows microvessels with high density along with irregularity in malignant nodules while microvessels in benign are much less and regular. HDMI biomarkers, shown on the right side of Figure 6.5 and 6.6 (top) for benign nodules and (bottom) for malignant, reports differentiating values between benign and malignant.

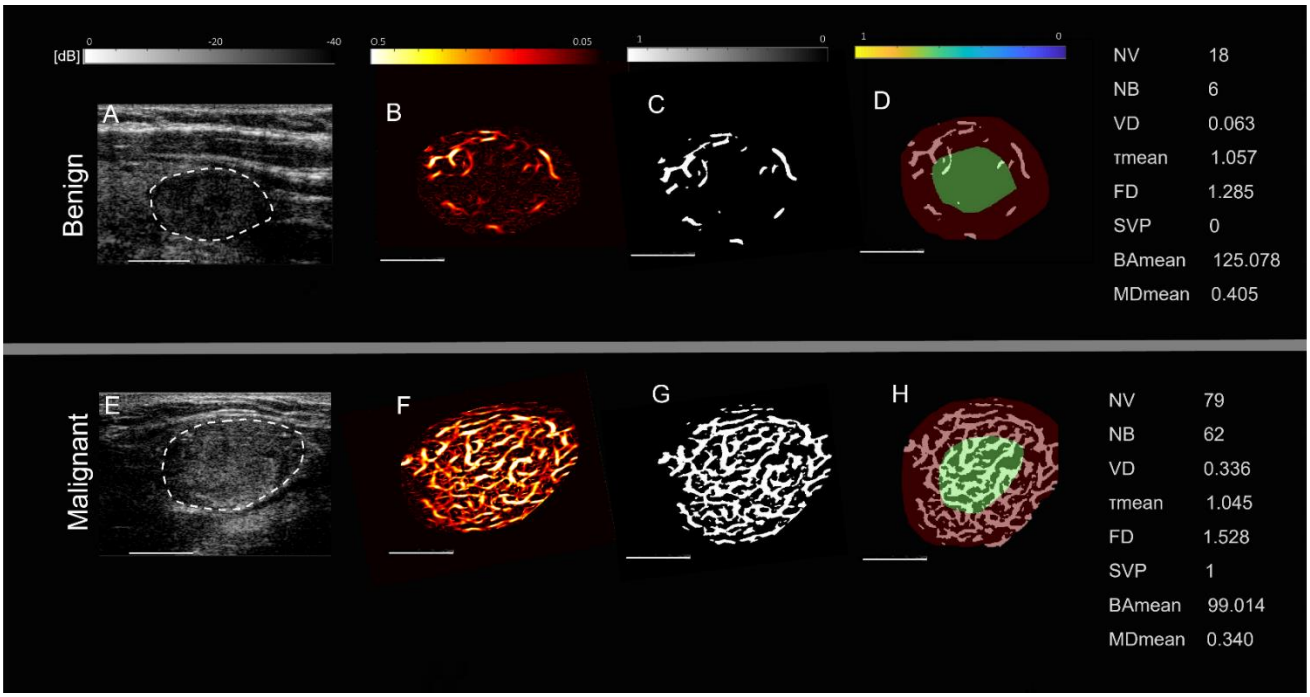

Figure 6.5: Representative images of large thyroid nodule>20mm, benign (top row) and malignant (bottom row). **(A)** and **(E) are** B-mode ultrasound images, **(B)** and **(F are** HDMI images showing tumor microvessels, **(C)** and **(G)** are binary images of microvessel, **(D)** and **(H)** Spatial Vessel Pattern (SVP) diagrams (green circle represent the central region and the red one the peripheral region of the nodule). The correspondent quantitative biomarkers are displayed on the right side of each row. White line

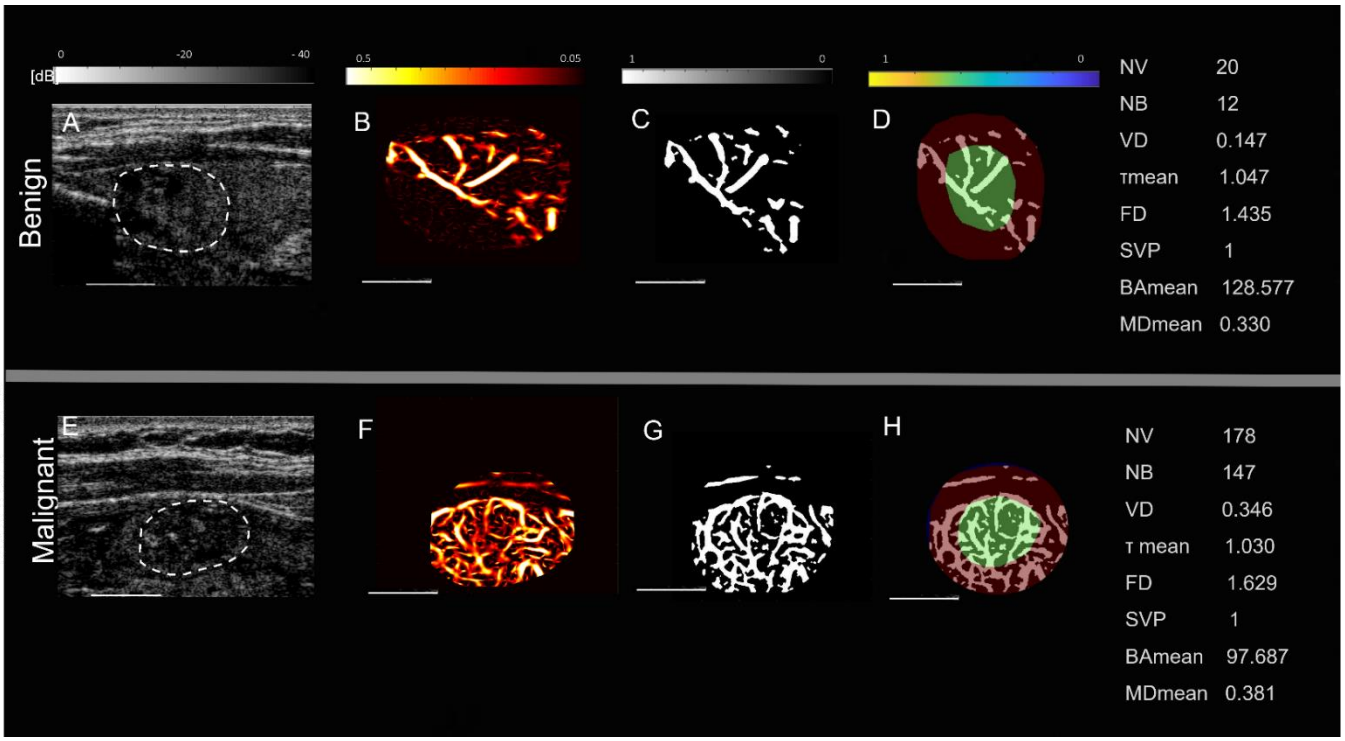

Figure 6.6: Representative images of small thyroid nodule<20mm, benign (top row) and malignant (bottom row). **(A)** and **(E) are** B-mode ultrasound images, **(B)** and **(F)** HDMI images, showing tumor microvessels, **(C)** and **(g)** are binary images of microvessel, **(D)** and **(H)** Spatial Vessel Pattern (SVP) diagrams, (green circle represent the central region and the red one the peripheral region of the nodule). The correspondent quantitative biomarkers are displayed right side of each row. White line denotes a scale of 1cm.

6.4 Statistical Results of HDMI Biomarkers

All malignant thyroid nodules had higher values of *(NV)*, *(NB)*, *(VD), (mvFD)* and *(MD)* when compared to benign nodules, demonstrating a p-value of (**4.9E-05, 9.8E-06, 6.1E-04, 5.5E-05, 5.5E-03**) respectively. The value of (BA_{mean}) was also a discriminative parameter, showing a decreases of bifurcation angle in malignant nodules when compared to the benign one with a p-value (**2.9E-03**).
For each nodule, the spatial vascularity pattern (SVP), which evaluates whether the vascular patterns are more concentrated peripherally or centrally the lesion, was reported as a binary value of 0 if the tumor was perinodular or 1 if it was intranodular. The results of the SVP in this study showed that an SVP equal to 0 is associated with a perinodular vascularization, as can be seen in Figure 6.4(d) conversely, SVP equal to 1 is associated with a higher intra-nodular vascularization concentration, as can be seen in Fig6.4. (h) and Fig6.5. (d,h).
The performance of HDMI biomarker is shown in Figure 6.7 (box plots, a-f), which shows a statistical significance difference in separating benign from malignant thyroid nodules. The performance of HDMI biomarkers is also shown in table 6.2, a $p< 0.05$ has been considered to have a statistical significance.

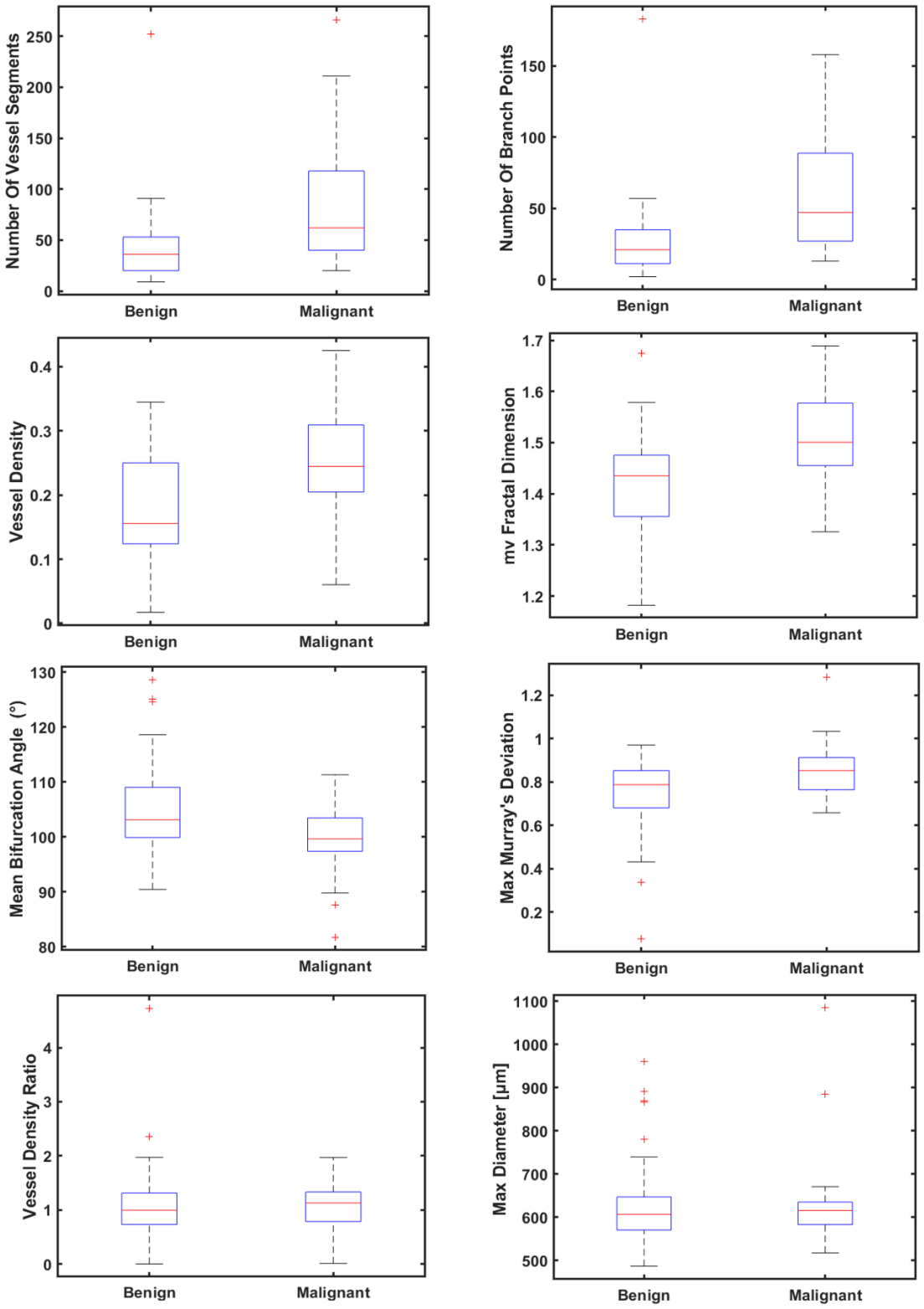

Figure 6.7**:** Box plots for differentiation of benign and malignant thyroid nodules. **a: vessel Density (VD), b: number of branch points (NB), c: number of vessel segments (NV), d: microvessel fractal dimension (mvFD), e: mean bifurcation angle (BA), f: maximum Murray's Deviation (DM_{max},), g:** maximum **diameter (D), h:** vessel density ratio (VDR). Benign (n=57) Malignant (n=35)

Table 6.2: Summary of the significant parameters, reported as mean ± standard deviation and p-value, in differentiating Benign an

HDMI Biomarkers	Benign (n=57)	Malignant (n=35)	P-value
Number of Branch Points	29.00 ± 8.49	42.50 ± 41.72	**9.8E-06**
Number of Vessel Segments	49.00 ± 1.41	65.50 ± 64.35	**4.9E-05**
Vessel Density	0.16 ± 0.12	0.14 ± 0.05	**6.1E-04**
Max Diameter [μm]	624.59 ± 48.48	624.04 ± 9.65	9.3E-01
Vessel Density Ratio	0.96±0.23	1.09±0.49	2.9E-01
Max Tortuosity	1.36±0.004	1.42±0.14	4.4E-01
Mean Tortuosity	1.05±0.01	1.06±0.01	7.05E-01
mv Fractal Dimension	1.43±0.01	1.46±0.14	**5.5E-05**
Bifurcation Angle Mean	108.31±96.00	94.41±6.55	**2.9E-03**
Bifurcation Angle Max	169.12±2.66	149.11±29.37	8.8E-02
Murray's Deviation Mean	0.36±0.02	0.38±0.03	2.8E-01
Murray's Deviation Max	0.81±0.12	0.84±0.13	**5.5E-03**

6.5 Differentiating Malignant nodules from Benign with HDMI Biomarkers, and Combined with Clinical Factors

Two models were developed, at first using biomarkers extracted from the HDMI only and the second model made by using the combination of HDMI markers and the clinical factors. The corresponding ROC curves are shown in Figure 6.8. HDMI biomarkers, NV, NB, VD, SVP, VDR, Tortuosity(τ) , BA, BA, MD, and FD were included in the HDMI model. From the first model the AUC was 0.83 (95% CI: 0.75-0.91), with a sensitivity of 78% and a specificity of 80%. The AUC was further increased when clinical factors, including age, d, and TI-RADS was added to the HDMI model. The corresponding AUC estimate was 0.88 (95% CI: 0.81-0.94), with a sensitivity of 88 % and a specificity of 73%.

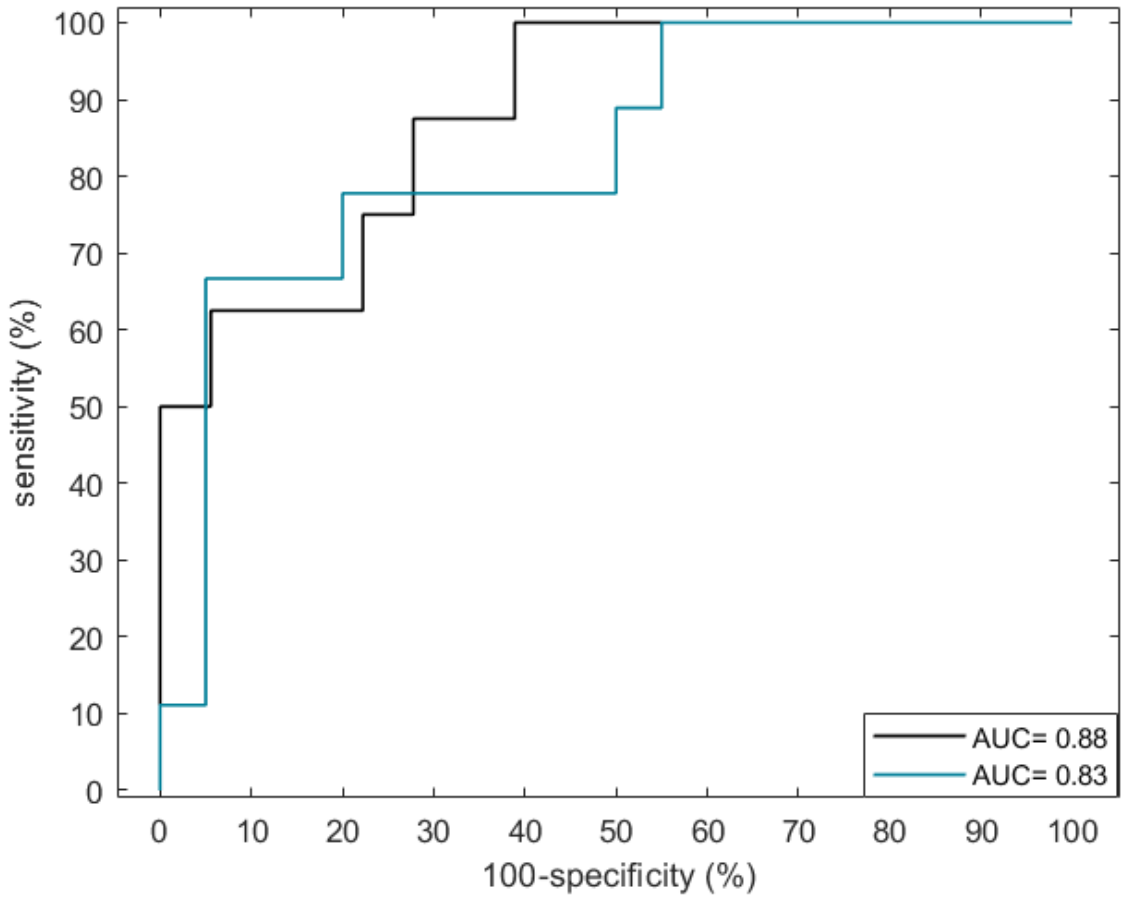

Figure 6.8: ROC curves generated using the HDMI biomarkers (blue) and HDMI biomarkers combined with clinical data (black)

7. Discussion

The present study, evaluated a set of microvessel morphological parameters, extracted from the US-based quantitative high-definition microvessel imaging technique (HDMI), as quantitative tumor biomarkers for differentiation of malignant and benign thyroid nodules. No contrast agent was applied to extract submillimeter microvessels. This study findings shows that six HDMI biomarkers, including vessel density, number of vessel segments, branch points, bifurcation angle (mean), and Murray deviation (max) provided meaningful separation between malignant and benign nodules. With multivariable analysis, using support vector machine classification method trained in the space of HDMI features, the current study shows that distinguishing performance of combined HDMI biomarkers are significantly better than any individual biomarker alone. The addition of clinical information such as age, nodule size, and TI-RADS scores, to the multivariable analysis increases the sensitivity, accuracy, and AUC. Other studies also without the help of contrast agents, reported the value of microvessel imaging for thyroid nodule differentiation, either using AngioPLUS Microvascular Imaging (35) , or superb microvessel imaging (SMI)(20), LuR 2017,Chen L 2019], however, the evaluation is mostly based on visual inspection and the quantification is limited to vessel index and pixel counting. Furthermore, studies combined SMI and CEUS to achieve better results in differentiating benign from malignant nodules, the limited quantification along with the inconvenience of injecting contrast agents exists(7). In support of these observation, Caresio et.al. confirmed the correlation between the morphology and distribution of blood vessels and the malignancy, when reconstructed vascular architecture from 3-D PDUS and CEUS images of thyroid nodules(36). This study shows that the diagnostic performance of HDMI biomarkers combined with TI-RADS for distinguishing benign and malignant thyroid nodules is better than HDMI biomarkers alone. The same observation has been reported, using SMI without addition of (20) and with TI-RADS scores (19) and for distinguishing benign and malignant thyroid nodules, demonstrating that TI-RADS improves the diagnostic accuracy. The present study demonstrates that benign nodules had a statistically significant lower number of vessel segments and branch points compared to the malignant thyroid nodules.

It is known that the rapid growth of the neoplasm is associated with a greater level of vessel sprouting, marker of malignancy, resulting in increased *NV* and *NB* in malignant tumors(37). This findings are also supported by our observation in breast cancer detection (22) (25)and studies by others (36),(38). Vessel density showed statistically significant differences between benign and malignant nodules.

Similar findings have been reported by other studies on thyroid nodule differentiation and (36) and in renal cell carcinoma (39) .

This study also demonstrates a higher values of Murray's deviation in malignant thyroid nodules, with MD_{max} showing a statistically significant difference of between the two groups. The diagnostic value of MD was demonstrated for different diseases (40), indicating that the vascular network of diseased and malignant tissue may show a deviation from Murray's law (41),(42) ,(43).Moreover, has been found a decrease in mean and standard deviation of the Bifurcation Angle in malignant thyroid nodules compared with the benign one. Similar findings have been reported in previous studies on invasive colon carcinomas (44) and breast cancer detection (24,25), showing smaller angles in vessel network of malignant tissues and with fewer branches in benign, the bifurcation angle among them is wider. Consistent with previous research on oral cancer carcinoma(45), renal cell carcinoma(46), glioblastoma (47), breast lesions(36), has been found that malignant nodules have significantly higher values of mvFD than benign and the discriminative power among the two groups was statistically significant ($p<0.000001$), suggesting that the hyper vascularity in malignant nodules is associated with complexity, irregularly branched, and distorted microvessel networks. The current study also investigated spatial vascular pattern with a peripherally distribution vasculature, SVP equal to 0, observed in benign but a higher intra nodular vessel concentration, SVP equal to 1 in malignant nodules.

One limitation of this study is that all quantitative biomarkers were evaluated using 2-dimensional (2D) HDMI, hence some significant 3-dimensional (3D) morphological features and connectivity of nodule microvessels may be overlooked by the 2D technique. Another limitation is the sample size which was relatively small. In addition, there is strong potential for data degradation due to motion caused by the thyroid's proximity to the pulsing carotid artery affects the visualization of microvessels (34).

8.Conclusion

In the present thesis, an upgraded High Definition Microvessel Imaging Technique for thyroid nodule identification and quantification was used.

Quantification of microvessel morphological features play an important role in disease diagnosis and tumor classification. All malignant thyroid nodules had higher values of *(NV)*, *(NB)*, *(VD), (mvFD)* and *(MD)* when compared to benign nodules, demonstrating a p-value of (**4.9E-05, 9.8E-06, 6.1E-04, 5.5E-05, 5.5E-03**) respectively. The value of (BA_{mean}) was also a discriminative parameter, showing a decreases of bifurcation angle in malignant nodules when compared to the benign one with a p-value (**2.9E-03**).

Two models has been realizeed, from the first model (HDMI) the AUC was 0.83 (95% CI: 0.75-0.91), with a sensitivity of 78% and a specificity of 80%. The AUC was further increased when clinical factors, including age, dimension, and TI-RADS was added to the HDMI model (HDMI-C). The corresponding AUC estimate was 0.88 (95% CI: 0.81-0.94), with a sensitivity of 88 % and a specificity of 73%.

In conclusion singular value spatiotemporal clutter filtering combined with Top-Hat filtering and Hessian filtering enhances the efficacy of tissue rejection in the presence of motion; although, combining this approach with motion correction might improve the performance of the extracted features in distinguishing benign from cancerous thyroid nodules.

Moreover, this analysis suggests that TI-RADS combined with HDMI biomarkers may have a good performance in distinguishing benign and malignant thyroid nodules, but in order to increase the diagnostic accuracy further detailed studies are required to confirm the present findings. Future work could include the evaluation of the performance of HDMI biomarkers equipped with motion correction on a larger and more heterogeneous patient population. Moreover, 3D microvasculature imaging would be helpful to overcome the limitations of 2D HDMI.

REFERENCES

1. Seib CD, Sosa JA. Evolving Understanding of the Epidemiology of Thyroid Cancer. Vol. 48, Endocrinology and Metabolism Clinics of North America. 2019.
2. Prete A, Borges de Souza P, Censi S, Muzza M, Nucci N, Sponziello M. Update on Fundamental Mechanisms of Thyroid Cancer. Vol. 11, Frontiers in Endocrinology. 2020.
3. Haugen BR, Alexander EK, Bible KC, Doherty GM, Mandel SJ, Nikiforov YE, et al. 2015 American Thyroid Association Management Guidelines for Adult Patients with Thyroid Nodules and Differentiated Thyroid Cancer: The American Thyroid Association Guidelines Task Force on Thyroid Nodules and Differentiated Thyroid Cancer. Thyroid. 2016 Jan 1;26(1):1–133.
4. Wiest PW, Hartshorne MF, Inskip PD, Crooks LA, Sylvia Vela B, Telepak RJ, et al. Thyroid palpation versus high-resolution thyroid ultrasonography in the detection of nodules. Journal of Ultrasound in Medicine. 1998;17(8).
5. Bessey LJ, Lai NBK, Coorough NE, Chen H, Sippel RS. The incidence of thyroid cancer by f ine needle aspiration varies by age and gender. Journal of Surgical Research. 2013;184(2).
6. Valderrabano P, McIver B. Evaluation and Management of Indeterminate Thyroid Nodules: The Revolution of Risk Stratification Beyond Cytological Diagnosis. Vol. 24, Cancer Control. 2017.
7. Zhao CK, Xu HX. Ultrasound elastography of the thyroid: Principles and current status. Ultrasonography. 2019;38(2).
8. Grani G, Lamartina L, Cantisani V, Maranghi M, Lucia P, Durante C. Interobserver agreement of various thyroid imaging reporting and data systems. Endocr Connect. 2018;7(1).
9. Cantisani V, Maceroni P, D'Andrea V, Patrizi G, di Segni M, de Vito C, et al. Strain ratio ultrasound elastography increases the accuracy of colour-Doppler ultrasound in the evaluation of Thy-3 nodules. A bi-centre university experience. Eur Radiol. 2016;26(5).
10. Kumar V, Webb J, Gregory A, Meixner DD, Knudsen JM, Callstrom M, et al. Automated Segmentation of Thyroid Nodule, Gland, and Cystic Components from Ultrasound Images Using Deep Learning. IEEE Access. 2020;8.
11. Gregory A, Bayat M, Kumar V, Denis M, Kim BH, Webb J, et al. Differentiation of Benign and Malignant Thyroid Nodules by Using Comb-push Ultrasound Shear Elastography: A Preliminary Two-plane View Study. Acad Radiol. 2018;25(11).

12. Park AY, Son EJ, Han K, Youk JH, Kim JA, Park CS. Shear wave elastography of thyroid nodules for the prediction of malignancy in a large scale study. Eur J Radiol. 2015;84(3).
13. Reginelli A, Urraro F, di Grezia G, Napolitano G, Maggialetti N, Cappabianca S, et al. Conventional ultrasound integrated with elastosonography and B-flow imaging in the diagnosis of thyroid nodular lesions. International Journal of Surgery. 2014;12(S1).
14. Ramsden JD. Angiogenesis in the thyroid gland. Vol. 166, Journal of Endocrinology. 2000.
15. Rajabi S, Dehghan MH, Dastmalchi R, Mashayekhi FJ, Salami S, Hedayati M. The roles and role-players in thyroid cancer angiogenesis. Endocr J. 2019;66(4).
16. Ebeed AE, Romeih MAE hamied, Refat MM, Salah NM. Role of ultrasound, color doppler, elastography and micropure imaging in differentiation between benign and malignant thyroid nodules. Egyptian Journal of Radiology and Nuclear Medicine. 2017;48(3).
17. Chammas MC, Gerhard R, de Oliveira IRS, Widman A, de Barros N, Durazzo M, et al. Thyroid nodules: Evaluation with power Doppler and duplex Doppler ultrasound. Otolaryngology - Head and Neck Surgery. 2005;132(6).
18. Newsome IG, Dayton PA. Visualization of Microvascular Angiogenesis Using Dual-Frequency Contrast-Enhanced Acoustic Angiography: A Review. Vol. 46, Ultrasound in Medicine and Biology. Elsevier Inc.; 2020. p. 2625–35.
19. Zhu C, Zhong L, Lin M, Tian C, Wang C. The value of TI-RADS combined with superb micro-vascular imagine in distinguishing benign and malignant thyroid nodules: A meta-analysis. PLoS One. 2022;17(1 January).
20. Hong MJ, Ahn HS, Ha SM, Park HJ, Oh J, Lalwani. N. Quantitative analysis of vascularity for thyroid nodules on ultrasound using superb microvascular imaging: Can nodular vascularity differentiate between malignant and benign thyroid nodules? Medicine (United States). 2022;101(5).
21. Bayat M, Fatemi M, Alizad A. Background Removal and Vessel Filtering of Noncontrast Ultrasound Images of Microvasculature. IEEE Trans Biomed Eng. 2019 Mar 1;66(3):831–42.
22. Ternifi R, Wang Y, Gu J, Polley EC, Carter JM, Pruthi S, et al. Ultrasound high-definition microvasculature imaging with novel quantitative biomarkers improves breast cancer detection accuracy. Eur Radiol. 2022;
23. Ghavami S, Bayat M, Fatemi M, Alizad A. Quantification of morphological features in non-contrast-enhanced ultrasound microvasculature imaging. IEEE Access. 2020;8:18925–37.
24. Ternifi R, Wang Y, Polley EC, Fazzio RT, Fatemi M, Alizad A. Quantitative Biomarkers for Cancer Detection Using Contrast-Free Ultrasound High-Definition Microvessel Imaging:

Fractal Dimension, Murray's Deviation, Bifurcation Angle Spatial Vascularity Pattern. IEEE Trans Med Imaging. 2021 Dec 1;40(12):3891–900.

25. Gu J, Ternifi R, Larson NB, Carter JM, Boughey JC, Stan DL, et al. Hybrid high-definition microvessel imaging/shear wave elastography improves breast lesion characterization. Breast Cancer Research. 2022;24(1).
26. physiopedia. Thyroid Gland.
27. Bauer DC, Mcphee SJ. 20: Thyroid Disease. 1998.
28. Bonjoc KJ, Young H, Warner S, Gernon T, Maghami E, Chaudhry A. Thyroid cancer diagnosis in the era of precision imaging. Vol. 12, Journal of Thoracic Disease. 2020.
29. Szabo TL. Diagnostic Ultrasound Imaging: Inside Out. Diagnostic Ultrasound Imaging: Inside Out. 2004.
30. Bjærum S, Torp H, Kristoffersen K. Clutter filter design for ultrasound color flow imaging. IEEE Trans Ultrason Ferroelectr Freq Control. 2002;49(2).
31. Souquet J, Bercoff J. Ultrafast Ultrasound Imaging. Ultrasound Med Biol. 2011;37(8).
32. Rubin JM, Bude RO, Carson PL, Bree RL, Adler RS. Power Doppler US: A potentially useful alternative to mean frequency- based color Doppler US. Radiology. 1994;190(3).
33. Demené C, Deffieux T, Pernot M, Osmanski BF, Biran V, Gennisson JL, et al. Spatiotemporal Clutter Filtering of Ultrafast Ultrasound Data Highly Increases Doppler and fUltrasound Sensitivity. IEEE Trans Med Imaging. 2015 Nov 1;34(11):2271–85.
34. Nayak R, Nawar N, Webb J, Fatemi M, Alizad A. Impact of imaging cross-section on visualization of thyroid microvessels using ultrasound: Pilot study. Sci Rep. 2020;10(1).
35. Chambara N, Liu SYW, Lo X, Ying M. Diagnostic Value of AngioPLUS Microvascular Imaging in Thyroid Nodule Diagnosis Using Quantitative and Qualitative Vascularity Grading. Biomedicines. 2022 Jul 1;10(7).
36. Caresio C, Caballo M, Deandrea M, Garberoglio R, Mormile A, Rossetto R, et al. Quantitative analysis of thyroid tumors vascularity: A comparison between 3-D contrast-enhanced ultrasound and 3-D Power Doppler on benign and malignant thyroid nodules. Med Phys. 2018;45(7).
37. Chappell JC, Wiley DM, Bautch VL. How blood vessel networks are made and measured. Cells Tissues Organs. 2011;195(1–2).
38. Lindsey B, Rojas J, Martin K, Shelton S, Dayton P. Acoustic characterization of contrast-to-tissue ratio and axial resolution for dual-frequency contrast-specific acoustic angiography imaging. IEEE Trans Ultrason Ferroelectr Freq Control. 2014;61(10).

39. Rojas JD, Papadopoulou V, Czernuszewicz TJ, Rajamahendiran RM, Chytil A, Chiang YC, et al. Ultrasound Measurement of Vascular Density to Evaluate Response to Anti-Angiogenic Therapy in Renal Cell Carcinoma. IEEE Trans Biomed Eng. 2019;66(3).
40. Sun M, Lv W, Zhao X, Qin L, Zhao Y, Xin X, et al. Vascular branching geometry relating to portal hypertension: A study of liver microvasculature in cirrhotic rats by X-ray phasecontrast computed tomography. Quant Imaging Med Surg. 2020;10(1).
41. Schoenenberger AW, Urbanek N, Toggweiler S, Seelos R, Jamshidi P, Resink TJ, et al. Deviation from Murray's law is associated with a higher degree of calcification in coronary bifurcations. Atherosclerosis. 2012;221(1).
42. Murray CD. The physiological principle of minimum work applied to the angle of branching of arteries. Journal of General Physiology. 1926;9(6).
43. McAllister A, Abramoff M, Xu X. Deviation from the optimal branching relationship of retinal vessels in diabetes mellitus. Invest Ophthalmol Vis Sci. 2013;54(15).
44. Konerding MA, Fait E, Gaumann A. 3D microvascular architecture of pre-cancerous lesions and invasive carcinomas of the colon. Br J Cancer. 2001;84(10).
45. Goutzanis LP, Papadogeorgakis N, Pavlopoulos PM, Petsinis V, Plochoras I, Eleftheriadis E, et al. Vascular fractal dimension and total vascular area in the study of oral cancer. Head Neck. 2009;31(3).
46. Sabo E, Boltenko A, Sova Y, Kleinhaus S, Resnick MB, Stein A. Microscopic analysis and significance of vascular architectural complexity in renal cell carcinoma. Clinical Cancer Research. 2001;7(3).
47. Chen C, He Z cheng, Shi Y, Zhou W, Zhang X, Xiao H liang, et al. Microvascular fractal dimension predicts prognosis and response to chemotherapy in glioblastoma: an automatic image analysis study. Laboratory Investigation. 2018;98(7).